# Annual Report 2021

Center for Nuclear Study,
Graduate School of Science, the University of Tokyo

Editor
  Hiroki Nagahama

**Center for Nuclear Study**

# Annual Report 2021

Center for Nuclear Study,
Graduate School of Science, the University of Tokyo

# Preface

This is the annual report of the Center for Nuclear Study (CNS), Graduate School of Science, the University of Tokyo, for the fiscal year 2021 (April 2021 through March 2022). During this period, a lot of research activities in various fields of nuclear physics have been carried out and a wide variety of fruitful results have been obtained at CNS. This report summarizes such research activities. I hereby mention some highlights of the report.

The Center for Nuclear Study (CNS) aims to elucidate the nature of nuclear system by producing the characteristic states where the Isospin, Spin and Quark degrees of freedom play central roles. These researches in CNS lead to the understanding of the matter based on common natures of many-body systems in various phases. We also aim at elucidating the explosion phenomena and the evolution of the universe by the direct measurements simulating nuclear reactions in the universe. In order to advance the nuclear science with heavy-ion reactions, we develop AVF upgrade, CRIB and SHARAQ facilities in the large-scale accelerators laboratories RIBF. The OEDO facility has been developed as an upgrade of the SHARAQ, where a RF deflector system has been introduced to obtain a good quality of low-energy beam. A new project for fundamental symmetry using heavy RIs has been starting to install new experimental devices in the RIBF. We promote collaboration programs at RIBF as well as RHIC-PHENIX and ALICE-LHC with scientists in the world, and host international meetings and conferences. We also provide educational opportunities to young scientists in the heavy-ion science through the graduate course as a member of the department of physics in the University of Tokyo and through hosting the international summer school.

The NUSPEQ (NUclear SPectroscopy for Extreme Quantum system) and Low Energy Nuclear Reaction group study exotic structures in high-isospin and/or high-spin states in nuclei. The groups play a major role in the OEDO/SHARAQ project described below. In 2021, analysis of a new measurement of the $^4\text{He}(^8\text{He}, {}^8\text{Be})4n$ reaction for better statistics and better accuracy has been proceeding. A recoil particle detector for missing mass spectroscopy, named TiNA, at OEDO had been upgraded under the collaboration with RIKEN and RCNP. The original TiNA consisted of 6 sector telescopes and 12 CsI (Tl) crystals. Four TTT-type (1024 channels) doubly-sided silicon detectors and twenty-two CsI(Tl) were added to make a TiNA2 array. The production cross sections of $^{178m2}\text{Hf}$ were evaluated for the mass production in the future with a new and simple chemical separation method. The inelastic decays from the isobaric analog resonances of $^{97}\text{Zr}$ were studied for the single particle wave functions coupled to the second $0^+$ state in $^{96}\text{Zr}$. The nature of the different shape of the second $0^+$ state from the ground state was revealed. The systematic studies of neutron-rich Zr isotopes are planned. The CNS GRAPE (Gamma-Ray detector Array with Position and Energy sensitivity) is also a major apparatus for high-resolution in-beam gamma-ray spectroscopy. The digital signal processing devices for the GRAPE are under development.

The main activity of the nuclear astrophysics group is to study astrophysical reactions and special nuclear structure, such as clusters, using the low-energy RI beam separator CRIB. In 2021, two major experimental projects at CRIB were completed and final publications were made; One was on the study of the $^7\text{Be}$ destruction process in the Big-bang nucleosynthesis, to solve the cosmological $^7\text{Li}$ abundance problem. The other is on the precise determination of the $^{22}\text{Mg}(\alpha, p)$ astrophysical reaction, relevant in X-ray bursts. In January 2022, we performed the first physics experiment at CRIB after the pandemic, which was to simultaneously study the $^{26}\text{Si}(\alpha,\alpha)$ scattering and the $(\alpha, p)$ reaction, relevant to the astrophysics.

Main goal of the quark physics group is to understand the properties of hot and dense nuclear matter created by colliding heavy nuclei at relativistic energies. The group has been involved in the ALICE experiment at Large Hadron Collider (LHC) at CERN. The group has led the global commissioning of the ALICE upgrades in 2021. The group has involved in the data analyses, which include the measurement of low-mass lepton pairs in Pb-Pb collisions, the measurement of long range

two particle correlations in p-Pb collisions, searches for thermal photons in high multiplicity pp and p-Pb collisions. The group has involved in the ALICE-TPC upgrade using a Gas Electron Multiplier (GEM), where the group is very active in the development and benchmarking of the online space-charge distortion corrections using machine learning techniques running on the Graphical Processing Unit (GPU).

The Exotic Nuclear Reaction group studies various exotic reactions induced by heavy-ion beams. We conducted a search of double Gamow-Teller resonance by a double charge exchange reaction ($^{12}$C, $^{12}$Be) at BigRIPS.

The OEDO/SHARAQ group pursues experimental studies of RI beams by using the high-resolution beamline and the SHARAQ spectrometer, and the OEDO for the decelerated RI beams.. SHARAQ11 experiment with a tritium-doped titanium target, which has been developed by Tohoku Univ. , was successfully conducted. For SHARAQ13, a mass measurement by the TOF-Brho technique for very proton-rich nuclei, an active stopper detector has been developed. The optics study of OEDO is under way to improve the transmission of the ion beams. For the high intensity RIBs, the delay-line PPACs have been replaced with the strip-readout PPACs. The experimental study of $0^-$ strength in nuclei using the parity-transfer charge exchange ($^{16}$O, $^{16}$F) will be reported soon. As for The OEDO beamline, the results of the first and second experiments for LLFPs will be finalised and reported soon. The profile of X ray from the RFD had been measured comprehensively, which finalised the design of the lead shield to enable us to conduct the in-beam gamma experiment at OEDO.

Three gaseous active target TPCs called CAT-S, CAT-M and GEM-MSTPC are developed and used for the missing mass spectroscopies. The CAT's are employed for the study of equation of state of nuclear matter. The measurement of giant monopole resonance in $^{132}$Sn at RIBF with CAT-S and the data analysis is ongoing. The CAT-M was employed for the systematic measurement of the deuteron inelastic scattering of the Xe and Kr isotopes. Newly developed permanent dipole magnet system was installed to reduce the background due to the delta rays. The GEM-MSTPC is employed for the nuclear astrophysics study. The data analysis of ($\alpha, p$) reaction on $^{18}$Ne and $^{22}$Mg and the $\beta$-decay of $^{16}$Ne followed by $\alpha$ emission are ongoing.

One of the major tasks of the accelerator group is the development of ion sources and the optimization of the beam transport system to CRIB, E7B, and C12 in the E7 experiment room. In 2021, the operating time of HyperECR ion source was 1773 hours. The beam production methods for metallic ions such as Li, Mg, and Fe have matured. High brightness metallic ion beams to match the requirement for the experiments can now be achieved stably and sustainably. Together with undergoing studies on ECR plasma, further improvements in beam qualities are expected. For the development of the 4-dimensional emittance monitor for the extracted beam from AVF cyclotron, the design of an optical system with a digital camera equipped with a tele lens was completed. Then, it is expected that the monitor can be kept away from the beamline which was the radiation source caused by the ion beam.

The development of an optical lattice interferometer to search for a permanent electric dipole moment (EDM) with Francium (Fr) atoms is now in progress at RIKEN. The lattice-like potential with a standing wave of laser light, the so-called optical lattice, can realize a long interaction time of the trapped Fr atoms with external fields, which allows to measure the EDM with high precision. The experimental apparatus to produce the cold Fr atoms trapped in the magneto-optical trap (MOT) is ready at present. We have confirmed that the newly developed surface ionizer can produce approximately $10^6$ Fr$^+$/s as a secondary beam via nuclear fusion reaction. We are now optimizing the experimental parameters to realize the high intensity cold Fr sources with $10^6$ atoms to measure the EDM.

The nuclear theory group participates in a project, "Program for Promoting Researches on the Supercomputer Fugaku", and has been promoting computational nuclear physics utilizing the Fugaku supercomputer. In FY2021, we performed large-scale shell-model calculations employing the Monte Carlo shell model and quasi-particle vacua shell model to investigate various exotic structures of

unstable nuclei. By using the no-core Monte Carlo shell model, we successfully describe the Hoyle state of $^{12}$C from the first principle without assuming any cluster structure. In the medium-heavy mass region, we successfully described the shape phase transition of Nd and Sm isotopes based on shell-model calculations and evaluated the nuclear matrix element of the neutrinoless double-beta decay of $^{150}$Nd. The nuclear Schiff moment of $^{129}$Xe was also investigated based on the shell model and we found an approximately linear correlation between the Schiff moment and the magnetic moment. In parallel, we promoted many research collaborations with experimental groups for investigating the structure of various nuclei such as $^{40}$Ca, $^{32}$Mg, $^{47,49}$Cl, and $^{55}$Cr.

The 20th CNS International Summer School named A3F-CNSSS21 was organized in August 2021. The school was jointly hosted by CNS and the A3-Foresight program, and supported by RIKEN Nishina Center and ANPhA. Because of the pandemic of COVID-19, the school was held with online. In addition to the participants from China, Korea and Vietnam, many participants from other countries such as Malaysia and India attended. Many invited lecturers including one foreign distinguished physicist gave classes.

Finally, I thank Ms. Shimane and other administrative staff members for their heartful contributions throughout the year.

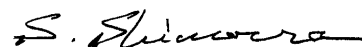<div style="text-align: right">

Susumu Shimoura
Director of CNS

</div>

# Table of Contents

## 1a. Experimental Nuclear Physics: Low and Intermediate Energies

## 1b. Experimental Nuclear Physics: PHENIX Experiment at BNL-RHIC and ALICE Experiment at CERN-LHC

## 2. Accelerator and Instrumentation

## 3. Theoretical Nuclear Physics

## 4. Other Activities

## Appendices

# Experimental Nuclear Physics:
# Low and Intermediate Energies

# Angular distribution of the transfer reaction of $^{79}$Se($d$, $p$) in inverse kinematics

N. Imai, M. Dozono, S. Michimasa, S. Ota, T. Sumikama[a], D. Suzuki[a], O. Beliuskina, S. Hayakawa,
C. Iwamoto, K. Kawata, N. Kitamura, S. Masuoka, P. Schrock, H. Shimizu, S. Shimoura,
K. Wimmer[1b], K. Yako, H. Yamaguchi, L. Yang, N. Chiga[a], D. Nagae[a], S. Omika[a], H. Otsu[a],
H. Sakurai[a], K. Yamada[a], S. Takeuchi[c], H. Miki[c], H. Yamada[c], S. Kawase[d], K. Nakano[d],
Y. Watanabe[d], K. Iribe[e], T. Teranishi[e], N. Aoi[f], E. Ideguchi[f], H.J. Ong[f], R. Yanagihara[f]

*Center for Nuclear Study, Graduate School of Science, University of Tokyo*
[a]*RIKEN Nishina Center*
[b]*Department of Physics, Univ. of Tokyo*
[c]*Tokyo Insititute of Technology*
[d]*Department of Advanced Energy Science and Engineering, Kyushu Univ.*
[e]*Department of Physics, Kyushu Univ.*
[f]*RCNP, Osaka Univ.*

The neutron capture reaction cross-sections are important for understanding the origin of the elements in the universe as well as the nuclear engineering. In some cases, the target nuclei are short-lived so that the measurement of the cross section is not feasible. $^{79}$Se is one of such nuclei. The nucleus is located on the path of s-process nucleosynthesis. Because the first excited state has a $\beta$ decay branch, the ratio of the daughter nucleus $^{79}$Br to $^{80}$Se can determine the temperature when the s-process took place [1]. However, although the main path of the s-process is the neutron capture to proceed to $^{80}$Se, because $^{79}$Se is radioactive the neutron capture cross section on $^{79}$Se has not been measured directly.

The nucleus is also known as the one of the long-lived fission products (LLFPs) of the nuclear wastes. It is supposed to be stored for millions of years in the deep geological repository, which has not been determined yet in Japan [2]. The transmutation of such LLFPs would be a possible way to avoid the inheriting of the nuclear waste to the future. To design the facility for the transmutation, cross sections of any neutron induced reactions must be evaluated precisely.

In the past, the neutron capture cross section was evaluated by measuring the photon strength function [3]. The neutron capture was deduced from the strength function assuming the level density, which are strongly model-dependent. As a result the evaluated cross section has a large uncertainty of a factor 7.

To evaluate the cross section of $^{79}$Se($n, \gamma$) independently, a surrogate ratio technique [4] was employed. In general, the compound neutron capture reaction is considered to be composed of two factors: the formation cross section of the compound states and the $\gamma$ decay probability from the unbound states. The energy-dependent formation cross section can be obtained by using the global optical potential. On the other hand, the $\gamma$ emission probability strongly depends on the nuclear structure of the nucleus. Once the $\gamma$ emission probability is obtained experimentally, the neutron capture cross sections can be determined. In the surrogate method, the same unbound states as those populated

by the compound reaction are assumed to be excited by an alternative nuclear reaction such as ($d, p$) reaction. In the case of ($d, p$) reaction, the excitation energy can be determined by measuring the recoiled protons. Therefore, when $\gamma$ emission channel at each excitation energy is identified, the neutron capture cross section can be determined.

For the surrogate ratio method, the $\gamma$ emission probability is often determined by measuring deexcitation $\gamma$ rays which requires the decay scheme from the unbound state. On the other hand, in our new method, the probability was determined by measuring reaction residues in coincidence with the recoiled proton, instead of measuring $\gamma$ ray. Our new technique is free from the small efficiency of detecting $\gamma$ rays and statistical model to estimate the de-excitation from the unbound state. The transfer reaction in the inverse kinematics made feasible the measurement.

The gamma emission probability, $P_\gamma$, is considered to depend on the spin and parity of the state as well as the excitation energy, $E_x$. Though the distributions of the spin and parity of the unbound states populated by the CN reactions may be different from those by the transfer reactions, the $P_\gamma$ of the populated state can be considered to be identical. The $P_\gamma$ can be obtained from the transfer reaction by taking into account the spin parity distributions of the reactions. In fact, in the absolute surrogate reaction techniques, the spin-dependent $P_\gamma$ was deduced by measuring the multi-polarities of $\gamma$ rays of subsequent decays with the statistical model [5].

When the kinetic energy dissipated in deuteron-induced reaction increases, the dominant reaction process gradually changes from the pre-equilibrium to the compound reaction [6]. In the pre-equilibrium reaction, some internal collisions are involved in the nucleus. Because the angular momenta of particles and holes excited in the reaction are coupled with the initial spin and transferred angular momentum, the spin-parity distribution can be close to the statistical distribution by the compound process, which is adopted in the TALYS-1.9 [7]. On the other hand, to explain the reaction mechanism to populate the unbound states by the transfer reactions, there are also theoretical works in the framework of the direct reactions [8, 9] which concluded

---
[1]Present Address:GSI, Darmstdt, Germany
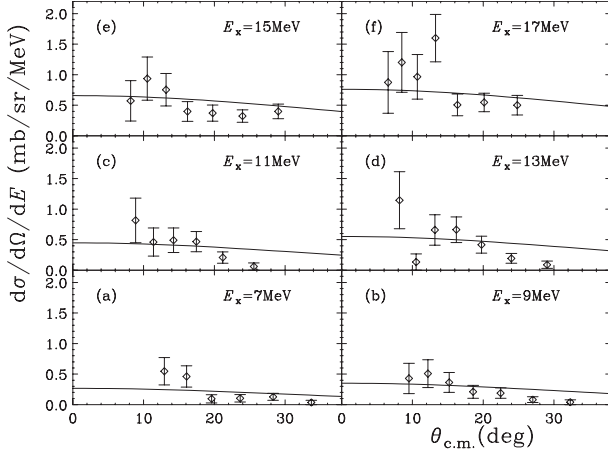
Figure 1. Double differential cross-sections of $^{79}$Se$(d,p)$ reaction at (a) $E_x = 7$, (b) 9, (c) 11 (d) 13, (e) 15, and (f) 17 MeV, respectively. The solid lines are the theoretical calculation assuming the pre-equilibrium with TALYS-1.9.

that the larger angular momenta were transferred to the state than the case of the neutron-capture reaction and that the transfered angular momentum depends on the nuclear structure.

Angular distributions of the transfer reaction help us to understand the reaction mechanism to populate the unbound state. The experimental angular distribution of $^{79}$Se$(d, p)$ reactions for the excited states from $E_x = 7$ to 17 MeV by 2 MeV step in the excitation energies of $^{80}$Se are presented in Fig 1. The smooth forward-peak structures were observed, suggesting that the pre-equilibrium process is dominated in the reaction above 7 MeV. The cross-sections are compared with the calculations using the phenomenological Kalbach model [10] as presented by the solid lines in Fig. 1. The curves are found to be in good agreement with the experiment, supporting the assumption of the pre-equilibrium reaction. In fact, in the calculation of TALYS-1.9 where the pre-equilibrium cross-section is estimated to be larger than the direct- and compound reaction cross-sections. It is worthy of mentioning that the calculated curves in Fig. 1 were not fitted to the experimental data.

The spin dsitribution shown in the previous report was calculated with the TALYS-1.9, where the spin distribution of the pre-equilibrium reaction is assumed to be the same as the compound reaction. Using the spin-dependent $\gamma$ emission proabilities obtained by the statistical modeel and the spin-distribution by TALYS-1.9, the experimental $P_\gamma$ was reproduced well, which enables us to determine the $(n, \gamma)$ cross sections. The final neutron capture cross section was deduced by using the $\gamma$ emission probabilities. The manuscript summarizing the result is under review.

### Acknowledgment

## References

[1] F. Kappler, H. Beer, and K. Wisshak, Rep. of Prog. in Phys. 52, 945 (1989).

[2] https://www.numo.or.jp/en/ .

[3] A. Makinaga et al., Phys. Rev. C **94**, 044304 (2016).

[4] J. E. Escher et al., Rev. of Mod. Phys. 84, 353 (2012).

[5] A. Ratkiewicz, et al., Phys. Rev. Lett. **122**, 052502 (2019).

[6] G. Mantzouranis, H.A. WeidenMüller, and D. Agassi, Z. Physik A 276, 145-154 (1976).

[7] A.J. Koning, S. Hilaire and M.C. Duijvestijn, *TALYS-1.0*, in Proceedings of the international Conference on Nuclear Data Science Technology 2007, EDP Science Nice, France (2008), p.211-214.

[8] G. Potel, F.M. Nunes, and I.J. Thompson, Phys. Rev. C **92**, 034611 (2015).

[9] Jin. Lei, and Antonio M. Moro, Phys. Rev. C **97**, 011601(R) (2018).

[10] C. Kalbach, Phys. Rev. C **37**, 2350 (1988).

# Single particle state coupled to the second $0^+$ state in $^{97}$Zr

R. Tsunoda, N. Imai, M. Dozono, S. Michimasa, N. Kitamura, B. Mauss[a], N. Shimizu, D. Suzuki[a], T. Teranishi[b], and K. Yanase

*Center for Nuclear Study, Graduate School of Science, University of Tokyo*
[a]*RIKEN Nishina Center*
[b]*Department of Physics, Kyushu Univ.*

Shape coexistence is a fascinating phenomenon in the atomic nucleus. It occurs when eigenstates with the same spin parity but different shapes degenerate in low excitation energies. In a naive picture, the phenomenon is explained as the 2$p$-2$h$ excitation either at the proton shell closure or at the neutron shell closure [1]. For example, in the zirconium isotope, which has the harmonics oscillator magic number of 40 for the proton number, a shape coexistence was suggested. Indeed, the low-lying second $0_2^+$ states have been measured in even-even Zr isotopes. The shape coexistence is also associated with the study of the diabadicity of the dynamics of the nuclear motion [2]. The strength of the pairing determines the degrees of the diabadicity.

In a recent theoretical work it is suggested that the shape coexistence is associated with the quantum phase transition in the quadruple deformation around $^{98}$Zr [3], where the onset of the large quadrupole deformation took place. In the framework of a shell model, even-even Zr isotopes are predicted to have shape coexistence. From the lightest stable Zr isotope of $^{90}$Zr to $^{98}$Zr, the ground states are spherical while the low-lying second $0^+$ ($0_2^+$) state is changing from the spherical shape to deformed shape. At $^{100}$Zr the deformations of the ground state and the $0_2^+$ state are considered to be inverted.

The traditional way to study the shape coexistence of the nuclei is to measure the band structures of the ground and the $0_2^+$ state. We here applied another independent measurement using the inelastic decay channel from the isobaric analog resonance (IAR). The IAR via proton elastic scattering provides the information on the single particle properties like one neutron transfer reaction. The inelastic channel yields the overlap between the excited final state of the target nucleus and the parent single particle state. Namely the inelastic channel would provide the single particle structure coupled to the excited state which cannot be obtained by ($d$, $p$) unless the excited state can be prepared as a target. In the past, there are several experimental studies on the inelastic decay to $0_2^+$ state. For example, in the case of the IARs of $^{91,93,95}$Zr, the first resonances coupled to the $0_2^+$ were found to be the same $J^\pi$ of those of ground states of $^{91,93,95}$Zr, respectively, suggesting that the core of the $0_2^+$ states of $^{90,92,94}$Zr are as spherical as the ground state of $^{90-94}$Zr. On the other hand, the shell model calculation predicts that the $0_2^+$ states in $^{90,92}$Zr are spherical, which is consistent with the past experimental results. The $0_2^+$ state of $^{94}$Zr is calculated to be deformed, which disagrees with the experimental result. The $0_2^+$ state in $^{96}$Zr, which is placed closely to the point of the quantum phase transition, was not been studied before although the elastic channel was reported [4]. In the
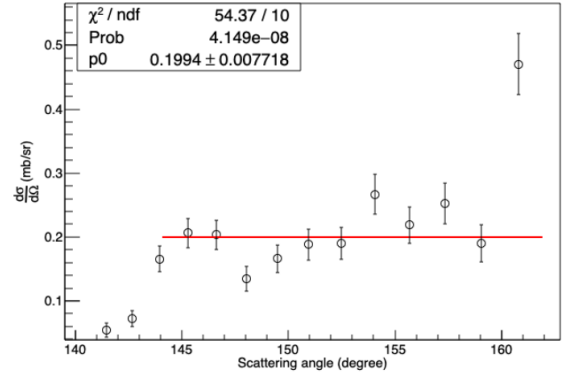


Figure 1. The angular distribution of the inelastic channel of $^{96}$Zr($p,p'$)$^{96}$Zr($0_2^+$) at $E_{c.m.} = 7.2$ MeV. The red line indicates the fitting result assuming $J = 1/2$.

case of $^{96}$Zr, the $0_2^+$ is predicted to be deformed like $^{94}$Zr.

To study the properties of the $0_2^+$ state in $^{96}$Zr, the experiment was carried out at the tanem accelerator facility of Kyushu University. The proton beam was directed onto a 0.5 mg/cm$^2$ thick $^{96}$Zr target. The beam intensity was monitored by the Faraday cup which was placed 30 cm downstream of the target. Two silicon detector telescopes were placed upstream of the target by 15 cm. Each telescope is composed of a $5 \times 5$ cm$^2$ pad type SSD and two sector-shape of 60 degrees singly stripped detector named YY1 with the outer diameter of 13 cm and the inner diameter of 5 cm. They were placed in perpendicular to the beam axis. YY1 has sixteen electrodes concentrically which allowed us to determine the scattering angle of the scattered protons from 140 to 160 degrees in the laboratory frame with about 1.2 degree step. The inelastic channels were identified by measuring the energies of the scattered protons. The proton beam energy was scanned from 5 to 9 MeV to search for the inelastic decay channel to the $0_2^+$ state. The isotope ratio of $^{96}$Zr was measured by the inductively coupled plasma mass spectroscopy. The ratio of $^{90,91,92,94,96}$ Zr isotopes were determined to be 6.3, 1.6, 2.3, 4.1, an 86%, respectively.

The excitation functions of the elastaic and inelastic scattering of $^{96}$Zr were already presented in Ref. [5]. We analayzed the angular distribution of the inelastic scattering to assign the spin-parity of the resonance strongly coupled to the $0_2^+$ state. The experimental angular distribution at $E_{c.m.} = 7.2$ MeV, where the largest resonance coupled to the $0_2^+$ state was observed, is shown in Fig. 1.

The angular distibution from a given spin $J$ is described

Table 1. Theoretical parameters for the angular distribution from a given state of $J$ expressed with Eq. 1.

| $J$ | $B_2$ | $B_4$ | $B_6$ |
|-----|-------|-------|-------|
| 1/2 | 0 | 0 | 0 |
| 3/2 | 1.0 | 0 | 0 |
| 5/2 | 1.142 | 0.857 | 0 |
| 7/2 | 1.190 | 1.051 | 0.758 |

as

$$W(\theta) = 1 + \sum_{L=0}^{2J-1} B_L P_L(\theta), \qquad (1)$$

where $P_L$ is the Legendre polynominal. The theoretical coefficients $B_L$ are summarized in Table 1.

If the meanfield is spherical like the ground state of $^{96}$Zr, the $J^\pi$ of the lowest resonance would be $J^\pi = 1/2^+$ which is the same $J^\pi$ as the ground state of $^{97}$Zr. Indeed, in the cases of the $^{90,92,94}$Zr$(p, p')$ reactions, the lowest resonances which decay to the $0_2^+$ states were observed to have the same $J^\pi$ of the ground state of $^{91,93,95}$Zr, respectively. Since the ground state $J^\pi$ is $1/2^+$, we fitted Eq. 1 with $J = 1/2$ to the experimental angular distribution, clearly ruling out the assignment. The $W(\theta)$ with $J = 5/2$ successfully reproduces the experimental angular distribution.

The $J^\pi$ value obtained is compared to the theoretical single particle enegies calculated by the quadrupole-constrained Hartree-Fock calculation. To make the 57th neutron orbit $5/2^+$, the prolate deformation of $Q = +130$ fm is needed.

As mentioned in Ref. [5], the resonance shape of the elastic scattering at 7.12 MeV suggested that the angular momentum of the first resonance coupled to the $0_2^+$ state was determined as $l = 2$. At the strongest resonance of $0_2^+$ channel at 7.22 MeV the resonance of the elastic channel was rather weak. In addition, the corresponding parent state was not measured in $^{97}$Zr. The different ordering of $l$s for resonances coupled to the $0_2^+$ state from those of the ground state is an evidence that the $0_2^+$ state is deformed.

The spectroscopic factor between the $0_2^+$ state and the parent state of $^{97}$Zr will be deetermined by taking into accout the angular distribution.

In summary, the inelastic decay channel to the $0_2^+$ state was proved as a powerful tool to study the shape coexistence nature. The method will be applied to the nuclei around the island of inversion and other nuclei like $^{98,100}$Zr at OEDO to understand the origin of the shell evolution.

## References

[1] K. Heyde and J.L. Wood, Rev. Mod. Phys. 83, 1467 (2011).

[2] T. Fukui, M. Matsuo, and K. Matsuyanagi, PTP 85, 281 (1991).

[3] Tomoaki Togashi, Yusuke Tsunoda, Takaharu Otsuka, and Noritaka Shimizu Phys. Rev. Lett. 117, 172502 (2016).

[4] W.R. CoKer, and C.F. Moore, Physics Today 22, 4, 53 (1969).

[5] R. Tsunoda, N. Imai et al. CNS Annual Report 2020.

# Three quasiparticle isomers in odd-even $^{159,161}$Pm: Calling for modified spin-orbit interaction for the neutron-rich region

R. Yokoyama[a,b], E. Ideguchi[c], G. Simpson[d], Mn. Tanaka[c], Yang Sun[e], Cui-Juan Lv[e], Yan-Xin Liu[f], Long-Jun Wang[g], S. Nishimura[h], P. Doornenbal[h], G. Lorusso[h], P. A. Söderström[h], T. Sumikama[i], J. Wu[j,h], Z. Y. Xu[k], N. Aoi[c], H. Baba[h], F. L. Bello Garrote[l], G. Benzoni[m], F. Browne[n,h], R. Daido[o], Y. Fang[o], N. Fukuda[h], A. Gottardo[p,m], G. Gey[q,h], S. Go[a], S. Inabe[h], T. Isobe[h], D. Kameda[h], K. Kobayashi[r], M. Kobayashi[a], I. Kojouharov[s], T. Komatsubara[t,u], T. Kubo[h], N. Kurz[s], I. Kuti[v], Z. Li[j], M. Matsushita[a], S. Michimasa[a], C. B. Moon[w], H. Nishibata[o], I. Nishizuka[i], A. Odahara[o], Z. Patel[x,h], S. Rice[x,h], E. Sahin[l], H. Sakurai[k,h], H. Schaffner[y,h], H. Sinclair[y,h], H. Suzuki[h], H. Takeda[h], J. Taprogge[z,aa], Zs. Vajta[v], H. Watanabe[ab], A. Yagi[o],

[a]Center for Nuclear Study, Graduate School of Science, University of Tokyo
[b]Department of Physics and Astronomy, University of Tennessee, Koxville, TN 37996, USA
[c]Research Center for Nuclear Physics, Osaka University, 10-1 Mihogaoka, Ibaraki, Osaka 567-0047, Japan
[d]LPSC, 53 Rue des Martyrs, F-38026 Grenoble Cedex, France
[e]School of Physics and Astronomy, Shanghai Jiao Tong University, Shanghai 200240, China
[f]School of Science, Huzhou University, Huzhou 313000, China
[g]School of Physical Science and Technology, Southwest University, Chongqing 400715, China
[h]RIKEN, Nishina Center, 2-1 Hirosawa, Wako, Saitama 351-0198, Japan
[i]Department of Physics, Tohoku University, Aramaki-aza-aoba, Aoba, Sendai, Miyagi 980-8578, Japan
[j]Department of Physics, Peking University, Beijing 100871, China
[k]Department of Physics, University of Tokyo, 7-3-1 Hongo, Bunkyo-ku, Tokyo 113-0033, Japan
[l]Department of Physics, University of Oslo, Oslo NO-0316, Norway
[m]INFN, Sezione di Milano, I-20133 Milano, Italy
[n]School of Computing, Engineering and Mathematics, University of Brighton, Brighton BN2 4GJ, United Kingdom
[o]Department of Physics, Osaka University, 1-1 Machikaneyama, Toyonaka, Osaka 560-0043, Japan
[p]Dipartimento di Fisica dellUniversità degli Studi di Padova, I-35131 Padova, Italy
[q]Institut Laue-Langevin, B.P. 156, F-38042 Grenoble Cedex 9, France
[r]Department of Physics, Rikkyo University, 3-34-1 Nishi-Ikebukuro, Toshima-ku, Tokyo 171-8501, Japan
[s]GSI Helmholtzzentrum für Schwerionenforschung GmbH, 64291 Darmstadt,Germany
[t]Research Facility Center for Pure and Applied Science, University of Tsukuba, Ibaraki 305-8577, Japan
[u]Rare Isotope Science Project, Institute for Basic Science, Daejeon 305-811, Korea
[v]MTA Atomki, P.O. Box 51, Debrecen, H-4001, Hungary
[w]Hoseo University, Asan, Chungnam 336-795, Korea
[x]Department of Physics, University of Surrey, Guildford GU2 7XH, United Kingdom
[y]Department of Physics, University of York, Heslington, York YO10 5DD, United Kingdom
[z]Instituto de Estructura de la Materia, CSIC, E-28006 Madrid, Spain
[aa]Departamento de Física Teórica, Universidad Autónoma de Madrid, Spain
[ab]International Research Center for Nuclei and Particles in the Cosmos, Beihang University, Beijing 100191, China

The nuclear properties of neutron-rich rare-earth nuclei around $Z = 60$ are the possible key to understanding the formation of the rare-earth peak in the elemental abundance at $\approx 160$. The pronounced abundance peaks at $A \approx 130$ and $A \approx 195$ are understood in terms of the enhanced stability of nuclei at the magic numbers. However, the production mechanism of the smaller peak of rare-earth elements is still under intensive investigation [1–3]. Simulations [4] found that the rare-earth peak is extremely sensitive to the nuclear-physics input, such as nuclear deformation and fission decay properties.

Analogous to the stability associated with large shell gaps in the spherical picture, a large shell gap between Nilsson single-particle (SP) orbitals stabilizes the nuclear shape at high deformation. Some theoretical work based on the relativistic mean-field theory predicted a deformed shell gap at $N = 100$ around $Z \sim 62$ [6], and Ghorui et al. [5] argued that the stability of $N = 100$ nuclei would make them serve as a waiting point in the nucleosynthesis of the $r$-process. It was discussed [7] that none of the Woods-Saxon, the Nilsson modified oscillator with "universal" parameters, and the folded Yukawa potentials succeeded in describing the correct ordering of the neutron SP states for the neutron-rich ($N = 98 - 102$) light rare-earth ($_{60}$Nd, $_{62}$Sm, and $_{64}$Gd) nuclei.

Liu *et al.* [8] recently proposed an isotope-dependent
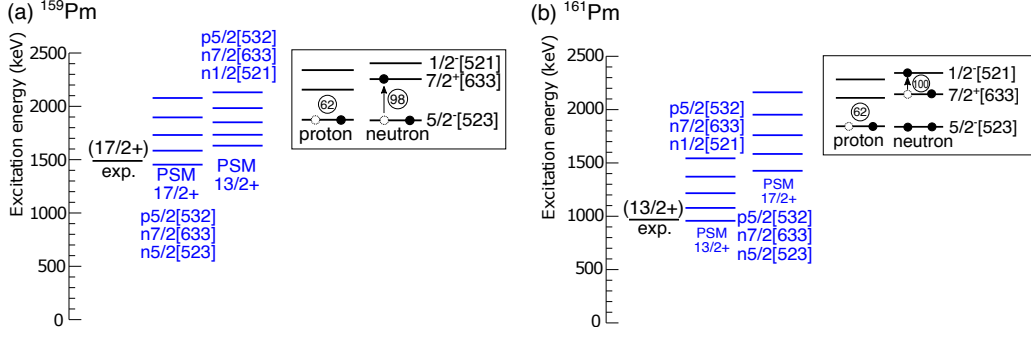
Figure 1. Calculated excitation energies of (a) $^{161}$Pm and (b) $^{159}$Pm by PSM. Levels with the caption "exp." below show experimental values.

spin-orbit term for the "standard" Nilsson model suggested by Bengtsson and Ragnarsson in 1985 [9] for the $A = 160$ region. It was emphasized in his paper [8] that study of isomeric states is of great importance since the energy of the isomeric states is sensitive to the spin-orbit interaction.

We performed isomer spectroscopy on neutron-rich $_{61}$Pm isotopes at RI Beam Factory at RIKEN, Nishina Center using the in-flight fission of the $^{238}$U$^{86+}$ beam. The delayed fl rays from the implanted ions were detected by a cluster-type Ge detector array, EURICA [10]. As a result, we observed new isomers in $^{159,161}$Pm. These are interpreted as 3-quasiparticle (qp) isomers with $^{\circ}7/2[633] \otimes {}^{\circ}5/2[523]$ and $^{\circ}7/2[633] \otimes {}^{\circ}1/2[521]$ two-quasineutron isomers observed at $N = 98$ and $N = 100$ isotones in this region [11–13] coupled with an odd proton in ß5/2[532].

In order to understand the observed 3-qp isomeric states in $^{159,161}$Pm, we apply the projected shell model (PSM) [14, 15]. The PSM became capable of calculating the 3-qp isomer discussed in the present experiment only very recently, thanks to the introduction of the Pfaffian algorithm for fast computation [16]. In the calculation, we use deformation parameters $\varepsilon_2 = 0.31$ and $\varepsilon_4 = 0.03$ for $^{159}$Pm, and $\varepsilon_2 = 0.30$ and $\varepsilon_4 = 0.01$ for $^{161}$Pm, which are consistent with those for other nuclei in this mass region [8].

Figure 1 compares the calculated and experimental levels in $^{159,161}$Pm. The calculated 3-qp isomers are reproduced at energies close to both data points. In $^{159}$Pm, the prediction that a $13/2^+$ lies higher than the $17/2^+$ state is consistent with the fact that the $13/2+$ state is not observed as an isomer. If we use the SP states generated by the standard Nilsson parameters in Ref. [9], this 3-qp state energy is calculated at higher than the $13/2^+$ state. In $^{161}$Pm, the calculated 3-qp state reproduces the $13/2^+$ data point at 966 MeV nicely. The $17/2^+$ 3-qp isomer is predicted above the $13/2^+$ state, which is consistent with the fact that we do not observe a $17/2^+$ state in the isomer decay scheme.

The significance of the present work is that it undoubtedly requests new Nilsson parameters for understanding the delicate relative positions between the $17/2^+$ isomer in $^{159}$Pm and $13/2^+$ isomer in $^{161}$Pm. These results indicate that the size of the spin-orbit interaction changes by adding neutrons from 98 to 100 and it pulls the $\nu 7/2^+[633]$ orbital

lower than expected in the standard Nilsson model.

In summary, we observed fl-rays from new isomers in $^{159,161}$Pm. These isomers are interpreted as 3-qp isomers with $^{\circ}7/2[633] \otimes {}^{\circ}5/2[523]$ and $^{\circ}7/2[633] \otimes {}^{\circ}1/2[521]$ two-quasineutron isomers observed at $N = 98$ and $N = 100$ isotones in this region coupled with an odd proton in ß5/2[532]. PSM calculations are performed to understand the observed 3-qp isomers and reproduced experimental data well only when the newly proposed Nilsson parameters [8] are used. This is the first clear case demonstrating that the "standard" Nilsson parameters for the stable nuclei need to be modified in exotic nuclei. This work raised the necessity of the modification to the Nilsson model in order to understand and predict nuclear properties especially the deformed shell gap of exotic nuclei outside the current reach of experiments which is an essential factor for the formation of the rare-earth peak in $r$-process abundance.

## References

[1] G. J. Mathews and J. J. Cowan, Nature **345** 491 (1990)

[2] R. Surman *et al.*, Phys. Rev. Lett. **79** 1809-1812 (1997)

[3] M. R. Mumpower *et al.*, Phys. Rev. C **85** 045801 (2012)

[4] M. R. Mumpower *et al.*, J. Phys G **44** 034003 (2017)

[5] S. K. Ghorui *et al.*, Phys. Rev. C **85** 064327 (2012)

[6] L. Satpathy and S. K. Patra, J. Phys. G **30** 771-781 (2003)

[7] D. J. Hartley *et al.*, Phys. Rev. Lett. **120** 182502 (2018)

[8] Y. X. Liu *et al.*, J. Phys. G **47** 055108 (2020)

[9] T. Bengtsson and I. Ragnarsson, Nucl. Phys. A **426** 14 (1985)

[10] P. A. Söderström *et al.*, Nucl. Instrum. Methods B **317** 323 (2013)

[11] Z. Patel *et al.*, Phys. Rev. Lett. **113** 262502 (2014)

[12] E. Ideguchi *et al.*, Phys. Rev. C **94** 064322 (2016)

[13] R. Yokoyama *et al.*, Phys. Rev. C **95** 034313 (2017)

[14] K. Hara and Y. Sun, Int. J. Mod. Phys. E **4** 637 (1995)

[15] Y. Sun, Phys. Scr. **91** 043005 (2016)

[16] L. J. Wang *et al.*, Phys. Rev. C **90** 011303(R) (2014)

# Tri-neutron search via the $^3$H$(t,^3$He$)^3n$ reaction – the first tritium target experiment at RIBF –

K. Miki [a,c], K. Kameya [a,c], N. Imai [b], S. Michimasa [b], S. Ota [b], M. Sasano [c], H. Takeda [c],
T. Uesaka [c], Y. Hatano [d], M. Hara [d], H. Haba [c], T. Hayamizu [c], T. Chillery [b], M. Dozono [e,c],
N. Fukuda [c], J. Gao [f], S. Hanai [b], S. Hayakawa [b], Y. Hijikata [e,c], K. Himi [g], J. Hwang [h],
T. Kawabata [g,c], K. Kishimoto [i,c], S. Kitayama [a,c], K. Kusaka [c], J. Li [b], Y. Maeda [j,c],
Y. Maruta [a,c], T. Matsui [a,c], H. Nishibata [i,c], M. Otake [c], H. Sakai [c], A. Sakaue [b], H. Sato [c],
K. Sekiguchi [a,c], Y. Shimizu [c], S. Shimoura [b], L. Stuhl [h,c], T. Sumikama [c], H. Suzuki [c],
R. Tsuji [e,c], S. Tsuji [g], H. Umetsu [a], R. Urayama [a,c], Y. Utsuki [a,c], T. Wakasa [i], K. Yako [b],
Y. Yanagisawa [c], N. Yokota [i,c], C. Yonemura [i,c], K. Yoshida [c], and M. Yoshimoto [c]

[a] Department of Physics, Tohoku University
[b] Center for Nuclear Study, the University of Tokyo
[c] RIKEN Nishina Center
[d] Hydrogen Isotope Research Center, University of Toyama
[e] Department of Physics, Kyoto University
[f] School of Physics, Peking University
[g] Department of Physics, Osaka University
[h] Center for Exotic Nuclear Studies, Institute for Basic Science
[i] Department of Physics, Kyushu University
[j] Faculty of Engineering, University of Miyazaki

If multiple neutrons are gathered in one place, how do they behave? This question has been fascinating to nuclear physicists for more than a half century. The interaction between two neutrons is attractive at medium- and long-range ($r \gtrsim 1$ fm), and therefore one expects some cluster structure, where neutrons stay together. For two neutrons, the interaction is not strong enough to make bound or resonant states, but one can observe a virtual state close to the threshold. How about more than two neutrons such as tri-neutron ($^3n$) and tetra-neutron ($^4n$)? Those multi-neutrons have been searched already from the 1960s. In the 20th century, sometimes positive results were reported, but such results were usually rejected by further studies. At that time, the production and detection of multi-neutron were both difficult and one had to rely on complicated methods. Recently, with the development of the experimental techniques with radioactive isotopes, the access to the vicinity of the nucleon drip line has become more feasible. Accordingly, new experiments with higher sensitivities to multi-neutrons have been performed and provided some positive results for tetra-neutrons. For example, $^{14}$Be breakup reaction [1] at GANIL, $^4$He$(^8$He,$^8$Be$)^4n$ reaction [2] and $^1$H$(^8$He, $p\alpha)^4n$ reaction [3] at RIBF. Compared with those tetra-neutron cases, the tri-neutron has been left unstudied. The tri-neutron is the simplest isospin $T = 3/2$ system, and its study is of fundamental significance. To investigate this exotic system, we performed the missing-mass spectroscopy of the $^3$H$(t,^3$He$)^3n$ reaction at 170 MeV/u.

An important challenge of this experiment was in the development and safe handling of the radioactive tritium target. For the experiment, we have developed a new tritiated

titanium (Ti-$^3$H) target at the Hydrogen Isotope Research Center (HRC) at the University of Toyama. We chose the target with the physical form of Ti-$^3$H for the following two reasons. In the Ti-$^3$H target, the tritium is tightly confined in the titanium lattice, which is beneficial for the target handling. The target is compact, compared with gas or liquid target, which is good for detecting decay particles from the target.

To accumulate enough statistics for the rare process such as tri-neutron production, we produced a target with a large tritium thickness of 3.5 mg/cm$^2$. It is about 90 times thicker than the ones used in the past nuclear physics experiments [4]. By optimizing the production conditions (temperature, vacuum, and so on) and also establishing the safe handling methods, such a thick target has been realized and used at RIBF.

The target produced at HRC was sent to the hot laboratory (HL) at RIBF. In the HL, the target was transferred from the transport container to the target chamber, and the chamber was pumped out to the vacuum. The chamber was then brought to the E20 experimental hall and attached to the scattering chamber. The target was kept under vacuum all the way and never exposed to the atmosphere after leaving the HL. During all the experiment, the tritium level of the experimental hall was monitored by the tritium detectors. All the procedures were safely done without any emergency nor any unexpected detection of tritium.

The overall layout of the experimental setup is shown in Fig. 1. The $^4$He particles were accelerated up to 200 MeV/u and bombarded the $^9$Be target with a thickness of 6 cm. Among various reaction products, the tritons of 170 MeV/u
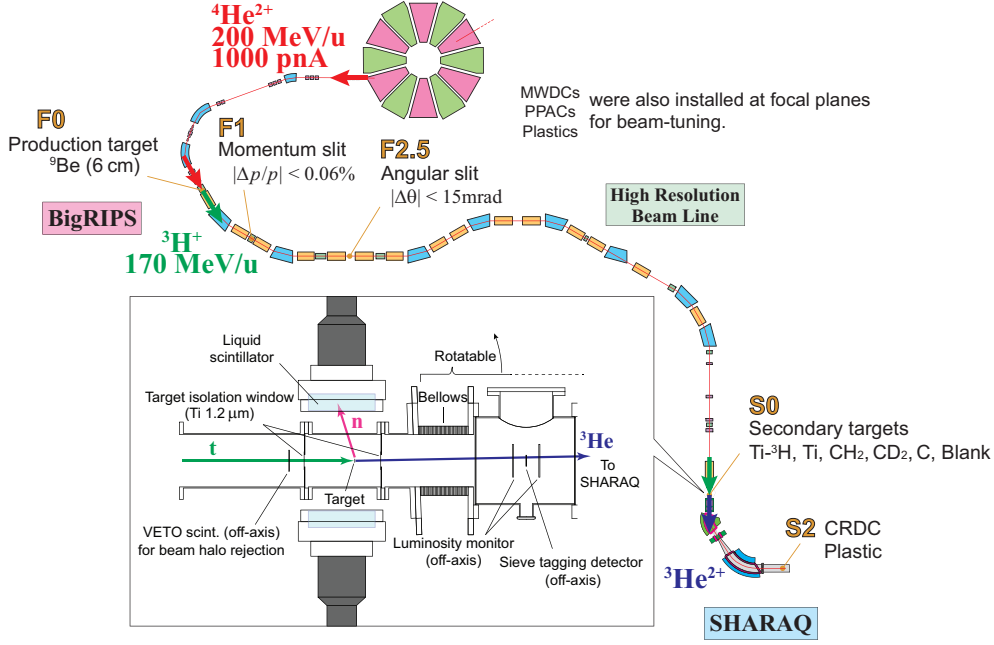
Figure 1. The overall setup of the $^3$H$(t, {}^3\text{He})^3n$ experiment. The $(t, {}^3\text{He})$ setup was based on the one in Ref. [5].

were selected by the BigRIPS separator. The emittance of the secondary beam was collimated by the momentum and angular slits at F1 and F2.5 positions, respectively. The beam was transported through the high-resolution beam line to the SHARAQ target position. With the primary beam intensity of 1000 pnA, the triton beam intensity of 50 MHz was achieved at the secondary target. It was the highest secondary beam intensity ever provided at RIBF. The $^3$He particles scattered from the target was momentum-analyzed by the SHARAQ spectrometer and detected by the CRDCs and plastic scintillators installed at the S2 focal plane. The decay neutrons from the target were detected by a pair of liquid scintillation counters. We took the data for Ti-$^3$H, Ti, CD$_2$, CH$_2$, C and blank targets for both spectrometer angles of 0 and 3 degrees. From those data, the missing mass spectra for $^{1,2,3}n$ systems will be obtained in a consistent manner.

Figure 2 shows the $XY$ spectra for the CH$_2(t, {}^3\text{He})$ reaction. The top and bottom figures represent the spectra at 0 and 3 degrees, respectively. For both cases, one can see the curved locus due to the $^1$H$(t, {}^3\text{He})^1n$ reaction kinematics, and upright loci of $^{12}$C$(t, {}^3\text{He})$ reactions. Those figures show that the missing-mass measurement was done properly. Further analyses are in progress.

**References**

[1] F.M. Marqués et al., Phys. Rev. C **65** (2002) 044006.
[2] K. Kisamori et al., Phys. Rev. Lett. **116** (2016) 052501.
[3] M. Duer et al., Nature **606** (2022) 678.
[4] K. Wimmer et al., Phys. Rev. Lett. **105** (2010) 252501.
[5] K. Miki et al., Phys. Rev. Lett. **108** (2012) 262503.
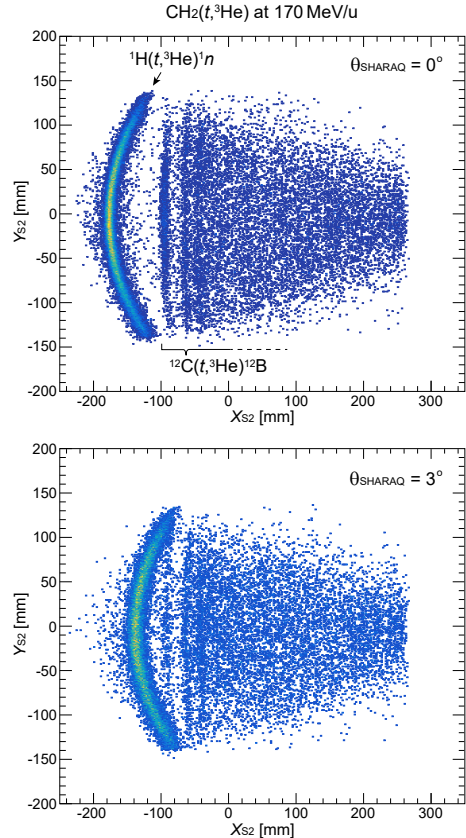
Figure 2. The $XY$ spectra at the S2 focal plane for the CH$_2(t, {}^3\text{He})$ reaction obtained with $\theta_{\text{SHARAQ}} = 0°$ (top) and $3°$ (bottom). For both angles, the kinematical curves for the $^1$H$(t, {}^3\text{He})^1n$ reaction were clearly observed.

# Study of the production of high-spin isomers in fragmentation reaction of $^{58}$Ni and $^{59}$Co beams at 350 MeV/u

Keita Kawata [a,b], Shinsuke Ota [a], Masanori Dozono [a], Juzo Zenihiro [b], Chihiro Iwamoto [a], Noritaka Kitamura[a], Hideyuki Sakai[b], Shoichiro Masuoka[a,b], Shin'ichiro Michimasa[a], Kentaro Yako[a], Tomoya Harada[b,c], Hiroki Nishibata[b], Rieko Tsunoda[a], Nobuaki Imai[a], Jongwon Hwang[a], Ningtao Zhang[d], Fumitaka Endo [e]

[a]*Center for Nuclear Study,University of Tokyo, Hongo, Tokyo 113-0033, Japan*
[b]*Riken Nishina Center, Wako, Saitama 351-0198, Japan*
[c]*Toho University, Toho University, Tokyo 143-8540, Japan*
[d]*Institute of Modern Physics, Lanzhou 73000, People's Republic of China*
[e]*Tohoku University, Miyagi 980-8578, Japan*

Projectile fragmentation is one of the most effective methods of producing unstable nuclei. Calculations of the reaction cross-section can be based on the abrasion-ablation model [1]. Fragments are produced from the projectile in two steps in the abrasion-ablation model. The first step is called the abrasion step, where some nucleons are stripped from the projectile nucleus to form a pre-fragment via peripheral reaction. The second step is called the ablation step, where the pre-fragment de-excites to "stable" states through an evaporation process with neutron and gamma-ray emission. The "stable" states include ground states and isomers, which are relatively long-lived metastable states.

While the total cross-section is calculated using the abrasion-ablation model, the momentum distribution is often described by the Goldhaber model [2], which considers the Fermi momentum in the nucleus focusing on the abrasion process. This simple model predicts secondary beams whose velocities are the same as those of primary beams with symmetric momentum distributions. On the other hand, the measured momentum distribution generally shows deceleration of the beam, and additional momentum spreads on the low-momentum side [3]. Attempts have been made to understand the fragmentation reactions through systematic data analysis, and an empirical model has been established by parametrization reflecting friction and deceleration, for example, but the detailed mechanism of these processes remains unclear [3, 4].

High-spin isomers are among the interesting products in fragmentation reactions. Isomer ratios of high-spin isomers are known to depend on the momentum of the secondary beams [5, 6]. We aim to study the role of the prefragment, a missing element in the Goldhaber model, by comparing the momentum distribution of (unbiased) fragments and that of high-spin isomers for the first time.

The experiment (project number H362) was performed at the SB2 course in HIMAC in Chiba. The primary beams of $^{58}$Ni and $^{59}$Co with 350 MeV/u bombarded the production target of a 14-mm thick $^{9}$Be target. The fragments of $^{52}$Fe, $^{53}$Fe, $^{54}$Co, and contaminants are separated by two dipoles magnets(D1 and D2), and the momentum is analyzed by a fragment separator consisting of two dipole magnets and quadrupole magnets. The angular acceptance is $\pm 4$ mr in the horizontal direction and $\pm 13$ mr in the vertical direction. The isomer is identified by measuring the de-excitation $\gamma$ rays. The detail of the experimental setup and data reduction is reported in Ref. [7].
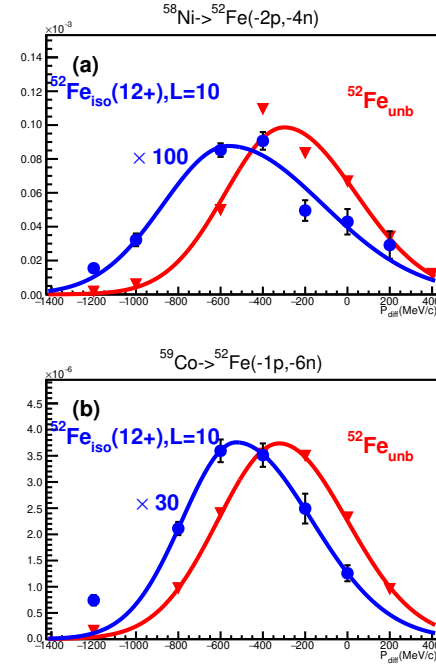


Figure 1. Example of momentum distributions of unbiased and isomer. The panel (a) shows the case of $^{52}$Fe from the $^{58}$Ni beam, and (b) shows the case of $^{52}$Fe from the $^{59}$Co beam. Red dots indicate unbiased and blue dots indicate isomer. The solid curves show the fitting results with asymmetric Gaussian functions.

Figure 1(a) and (b) show the momentum distributions of $^{52}$Fe fragments from the $^{58}$Ni and $^{59}$Co beams, respectively. The red points are the data for the unbiased $^{52}$Fe nuclei without detecting gamma rays, while the blue points are those for isomers. Here the vertical axis is the number of unbiased $^{52}$Fe nuclei divided by the number of primary beams, with correction of the effective solid angle at the slits in F2 depending on the B$\rho$ of the secondary

beam. The blue dots are similarly corrected values of the number of isomers produced divided by the number of primary beams. The horizontal axis is the momentum difference($p_{\text{diff}}$ (MeV/c)). The momentum difference is obtained from the momentum of the products where the origin ($p_{\text{diff}} = 0$ MeV/c) is defined as the same velocity before and after the reaction when a fragmentation reaction occurs at the half-point in the target. The momentum before the reaction was calculated from the primary beam energy, and the momentum after the reaction was obtained from the filed strength of D1.

The momentum of the unbiased fragments is generally lower than the beam, as studied in many cases [3,4]. Notani et al. discussed the momentum peak shift as well as the deviation at the tails of isotopic chains from the general behavior [3]. The momentum of the isomers is significantly lower than that of unbiased fragments. Each momentum distribution is fitted with asymmetric gaussian with four free parameters where the width parameters of the left-hand half and right-hand half are different. From here on, only the peak positions are discussed.

The production mechanism of high-spin isomers like $^{52}$Fe(12+) was discussed in terms of momentum obtained from the abrasion process [5, 6]. Likewise, we discuss the angular momentum introduced to the fragment kinematically by using the representative angular momentum of $L = 10$ for $^{52}$Fe(12+).
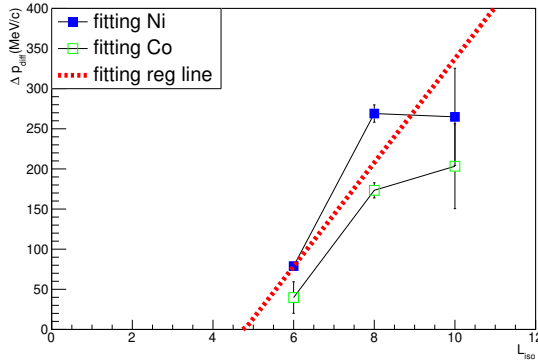


Figure 2. $L_{\text{iso}}$ vs $\Delta$p plot. Blue squares indicate each fragment from $^{58}$Ni beam. Green open squares indicate each fragment from $^{59}$Co beam. The red dotted line shows the regression line.

Figure 2 shows the difference on the central values of $p_{\text{diff}}$ between unbiased and isomer defined by $\Delta p_{\text{diff}} = p_{\text{diff}}(\text{unb}) - p_{\text{diff}}(\text{iso})$ as a function of representative $L_{\text{iso}}$ values ($L = 8$ for $^{53}$Fe(19/2−) and $L = 6$ for $^{54}$Co(7+)). One can see a correlation, presumably a linear relationship, between the $\Delta p_{\text{diff}}$ and $L_{\text{iso}}$. The correlation coefficient is $r = 0.82$ and the regression line is $\Delta p_{\text{diff}} = (64.7 \pm 3.8)(\text{MeV}/\hbar c) \times (L_{\text{iso}} - 4.8 \pm 0.1)$. The $\Delta p_{\text{diff}}$ is related to the angular momentum transfer for the following reason. As mentioned before, the fragmentation reaction in this report with a few nucleon removals in the intermediate energy is through peripheral reaction, where the nucleons in the projectile and target collide with one another near the nuclear surface, transferring momentum. In such a case the addi-

tional momentum transfer ($\Delta p_{\text{diff}}$) is related to the added angular momentum by $\Delta p_{\text{diff}} = \text{a} \times \Delta \text{L}$, where $\Delta L$ is the additional angular momentum transfer ($\Delta L = L_{\text{iso}} - L_{\text{unb}}$). Note that the unbiased angular momentum ($L_{\text{unb}}$), the angular momentum of the pre-fragment, is not necessarily the same as that of g.s.

Here $1/a = (3.0 \pm 0.2)$ fm is 70% of the expected value of the radius of the fragment ($R = 1.2 fm \times \text{A}^{1/3} = 4.5$ fm, and A means the mass number of the fragment). We note the correlation in Fig.2 is understood by taking a common $L_{\text{unb}}$ among all the fragments, the best-fit value being $(4.8 \pm 0.1)$ $\hbar$. These results suggest that the pre-fragment generally has a finite angular momentum, and the fragment further gaining the necessary angular momentum through the abrasion process can become an isomer.

Finally, the effect of $L_{\text{prj}}$ in high-spin isomer production can be assessed by closely examining Fig.2 in principle. Since $^{59}$Co(g.s.; $J^{\pi} = 7/2-$) has a representative angular momentum of $L = 3$, this can contribute to isomer formation resulting in a reduction of $\Delta p_{\text{diff}}$. One can see a slightly different correlation for $^{58}$Ni and $^{59}$Co beam with a small offset of $^{59}$Co correlation shifting downward. The quantitative argument whether we are looking at the effect of $L_{\text{prj}}$ by this plot is among the future work.

## References

[1] Gosset *et al.*, PhysRevC **16**.629 (1977)

[2] A.S. Goldhaber *et al.*, Physics Letters B**53** 306−308 (1974).

[3] M. Notani *et al.*, Phys. Rev. C.**15** 044605 (2007).

[4] B. Mei *et al.*, Phys. Rev. C, **95** 034608 (2017).

[5] J. M. Daugas, *et al.*, Phys. Rev. C, 63 064609 (2001).

[6] W.-D Schmidt *et al.*, Z. Phys A **350** 215-219 (1994)

[7] K.Kawata *et al.*, CNS Annual report (2019)

# The search for double Gamow–Teller giant resonance at RIBF

A. Sakaue for the RIBF-141R1 collaboration

*Center for Nuclear Study, Graduate School of Science, University of Tokyo*

The double Gamow–Teller (DGT) transition is a nuclear process such that the spin and isospin are changed twice by a $(\sigma\tau)^2$ operator, where $\sigma$ and $\tau$ are the spin and isospin operators, respectively. Double $\beta$ decay is also driven by the same operator. Its transition strength is limited to a small proportion of the total DGT transition strength, but experimental information about the DGT is currently limited to this rare process. Existence of giant resonance which occupies most of the transition strength was first proposed in 1989 [1]. This resonance, called the DGT giant resonance (DGTGR), remains undiscovered experimentally. The experimental observation of DGTGR will provide information about two-phonon excitations which is not examined with the nuclear spin-dependent correlations.

Experimental information of the DGTGR is also potentially important for determining the nature of neutrinos. The transition strength and centroid energy of the DGTGR are suggested to be strongly correlated with the nuclear matrix element of a neutrinoless double $\beta$ decay [2]. Theoretically predicted values of the nuclear matrix element have a large uncertainty depending on the chosen model [3]. Experimental information of the DGTGR will provide reference for the calculation of the nuclear matrix element.

We are aiming at the observation of the DGTGR using the double charge exchange reaction ($^{12}$C, $^{12}$Be($0_2^+$)). This reaction is effective for the observation of the DGTGR for the following reasons. First, the transition from $^{12}$C($0_{g.s.}^+$) to $^{12}$Be($0_2^+$) through the intermediate state of $^{12}$B($1^+$) is expected to be strong since these states are all dominated by $0\hbar\omega$ configurations. Second, we can utilize an isomeric decay of $^{12}$Be($0_2^+$), for event selection. $^{12}$Be($0_2^+$) has a lifetime of $331 \pm 12$ ns and decays into the ground state by emitting an electron-positron pair [4]. Detecting back-to-back photons with an individual energy of 511 keV from the positron serves to tag the events of the double spin-flip mode.

A pilot experiment using the ($^{12}$C, $^{12}$Be($0_2^+$)) reaction was performed at Research Center for Nuclear Physics (RCNP) [5–8]. In this experiment, a 100 MeV/nucleon $^{12}$C beam with an intensity of 17 particle nA impinged on $^{48}$Ca target and the momentum of an ejected $^{12}$Be was measured by Grand Raiden spectrometer. $^{12}$Be was implanted in a plastic scintillator stopper downstream of the focal plane of the spectrometer and photons originating from $^{12}$Be($0_2^+$) were detected by NaI(Tl) detectors. The identification of the $^{12}$Be($0_2^+$) by detecting the 511 keV photon worked well. The conclusive evidence of the DGTGR was not obtained due to the background coming from the plastic stopper and the lack of the statistics. The main background was $^3$H from the target; it hit the plastic stopper and produced the $\beta^+$ emitting nuclei.

We performed the experiment at the RI Beam Factory (RIBF) considering the experience in the pilot experiement.

In this experiment, we used a part of BigRIPS separator, F0–F5, as a spectrometer, as established in pionic atoms experiments [9]. A $^{12}$C primary beam with an intensity of 500 particle nA was accelerated to 250 MeV/nucleon and bombarded on a target at F0 focal plane of the BigRIPS separator. The momentum spread of the beam, $\delta p/p \sim 0.6\%$, was reduced to about 0.026% by applying dispersion-matching optics. We used $^{48}$Ca or $^{116}$Cd as the target, which are important double $\beta$ decaying nuclei. The thickness of the target was 10 mg/cm$^2$ for $^{48}$Ca and 50 mg/cm$^2$ for $^{116}$Cd. The ejected particle was momentum-analyzed by the magnets between F0 and F5. The track of the particle was measured by the low-pressure multiwire drift chambers (MWDCs) at F5 focal plane. After passing through F5, the particle was transferred to F8 focal plane and stopped in a $^9$Be stopper with a thickness of 18.8 mm. Delayed $\gamma$ rays deriving from $^{12}$Be($0_2^+$) were detected by a DALI2 array at F8. We chose $^9$Be as a stopper since it does not produce $\beta^+$-decaying nuclei. We set degraders at F5 and F7 to stop at F8 for $^{12}$Be and to sweep background particles such as $^3$H, $^6$He, and $^9$Li.

During the beam time, we measured the double-charge exchange reaction for 40 h for $^{48}$Ca and 20 h for $^{116}$Cd, respectively. Figure 1 shows the energy spectrum of the photons measured by DALI2 for the $^{48}$Ca target. A peak at the energy of 511 keV is noticeable in the spectrum. Figure 2 shows the timing of the photon detection relative to the signal from a plastic scintillator at F7. Here, the timing distribution of the events in the energy region of $500 \pm 100$ keV is shown. The decay histogram is fitted by an exponential curve and a constant background. The decay constant is $302.3 \pm 8.2$ ns, which is close to the known value of the lifetime of $^{12}$Be($0_2^+$). This suggests that $^{12}$Be($0_2^+$) is successfully detected. The contamination of backgrounds is estimated to be about 15% when the events between $500 \pm 100$ keV in energy are selected. The background rate was improved from the experiment at RCNP, in which the signal-to-background ratio was about 1:1 [7].

The preliminary spectrum of the excitation energy of $^{48}$Ti is shown in Fig. 3. The event selection is such that the timing of the photon is 20 ns after from prompt $\gamma$-rays and the energy is in the region of $500 \pm 100$ keV. Each fill color corresponds to the scattering angle in the laboratory system within 0.0–0.3° (the lightest color), 0.3–0.6°, 0.6–0.9°, 0.9–1.2°, and 1.2–1.5° (the darkest color). The energy resolution and the angular resolution was evaluated as 1.6 MeV and 0.17°, respectively. There seems to be an enhancement around 30 MeV in the excitation energy spectrum, which stands out especially in the forward angle. We are now dedicated to more precise analysis and the interpretation of the structure of the spectra.
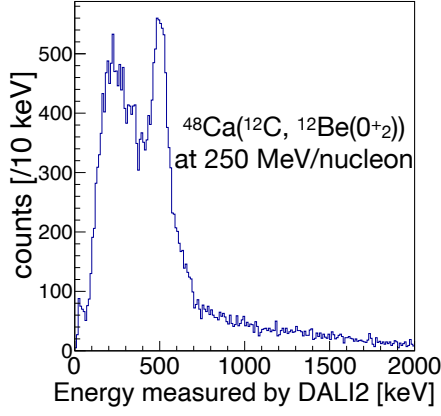
Figure 1. Energy distribution of delayed $\gamma$ rays measured by DALI2.
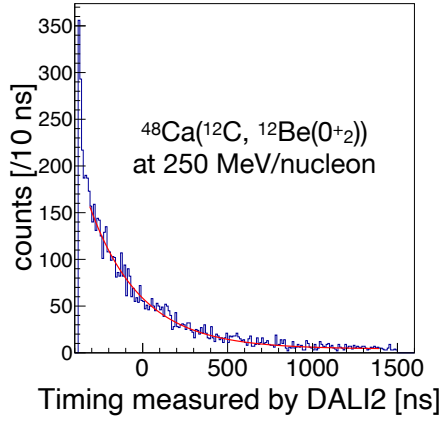


Figure 2. Timing distribution of delayed $\gamma$ rays for events in energy region of $500 \pm 100$ keV. Red curve is fitting result.

### References

[1] N. Auerbach, L. Zamick, and D. Zheng, Ann. Phys. **192**, 77 (1989).

[2] N. Shimizu, J. Menéndez, and K. Yako, Phys. Rev. Lett. **120**, 142502 (2018).

[3] J. Engel and J. Menéndez, Rep. Prog. Phys. **80**, 046301 (2017).

[4] S. Shimoura *et al.*, Phys. Lett. B **654**, 87 (2007).

[5] M. Takaki *et al.*, CNS Rep. **94**, 9 (2016).

[6] M. Takaki *et al.*, CNS Rep. **95**, 15 (2017).

[7] M. Takaki *et al.*, CNS Rep. **96**, 3 (2018).

[8] M. Takaki *et al.*, CNS Rep. **97**, 23 (2019).

[9] T. Nishi *et al.*, Nucl. Instrum. Methods Phys. Res. B **317**, 290 (2013).
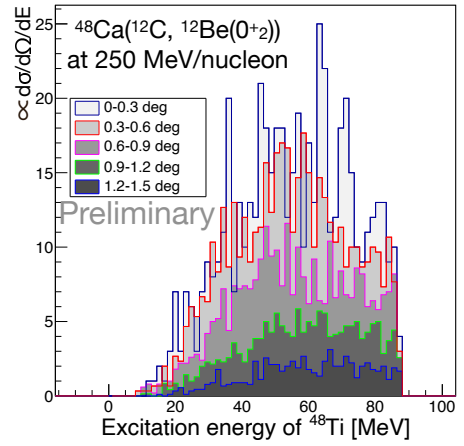
Figure 3. Preliminary result of $^{48}$Ti excitation energy spectrum. Fill colors correspond to selected regions of scattering angles.

# Development and performance evaluation of Mini TPC for tracking heavy-ion high-intensity beam in CAT-M

F. Endo, S. Ota[a], R. Kojima[b],

*Department of Physics, Tohoku University*
*[a]Research Center for Nuclear Physics, Osaka University*
*[b] Center for Nuclear Study, Graduate School of Science, University of Tokyo*

The equation of state (EOS) of nuclear matter plays an important role in understanding nuclear synthesis, neutron star, massive star mergers [1]. The EoS is expressed as a power expansion of the density, with the second-order coefficient being the incompressibility in nuclear matter. The contribution of the second-order is expected to be significant in extreme environments such as neutron stars. The incompressibility in nuclei can be expressed by using the one in infinite nuclear matter based on the droplet model as described below. [2]. This indicates that the incompressibility in infinite nuclear matter can be extracted from the systematic measurement of the incompressibility in nuclei.

$$K_A = K_0 + K_s A^{-1/3} + \left( K_\tau + K_{\tau s} A^{-1/3} \right) \alpha^2$$
$$+ K_C Z^2 A^{-4/3}. \tag{1}$$

Here, $K_s$ and $K_{\tau s}$ are surface terms and $K_C$ is the Coulomb term. $K_C$ can be assumed to be known because the model dependence is very small. In previous studies, It has been determined as an $K_\tau = -550 \pm 100$ MeV. On the other hand, $K_{\tau s}$ has not been determined yet [3]. Quantitative evaluation of the surface term from systematic ISGMR measurements using various nuclei including unstable nuclei may deduce the $K_\tau$ with higher precision. In the case of ISGMR measurement for unstable nuclei, the gas-active target is optimal because the only other option is to use an RI beam, which must measure low-energy recoil particles in the vicinity of the reaction point.

We have developed an active target (CAT-M) that can be irradiated with high-intensity heavy-ion beam and that is employed for the systematic measurement of the ISGMRs [4]. In the most recent upgrade, a dipole magnet was installed in the beam region to remove the $\delta$-rays produced by the beam particles. As a result, the SN ratio was improved by a factor of 100. However, beacuse the magnet shields the read-out pads, it is impossible to measure the beam particle, so a new beam position detector near the reaction point needs to be developed. In this paper, we first present an overview of a new compact TPC named Mini TPC and its performance based on simulations. Next, the setup and results of experiment are reported.

We describe the structure of the newly developed Mini TPC and the expected resolution based on the electric field simulations. A schematic view of the Mini TPC is shown in Fig. 1. The Mini TPC consists of a field cage, thick gas electron multipliers, and a readout board. Two types of THGEMs are used in Mini TPC. The Normal THGEM has holes with a radius of 200 $\mu$m and a pitch of 500 $\mu$m, while the Flower THGEM has the same hole diameter but
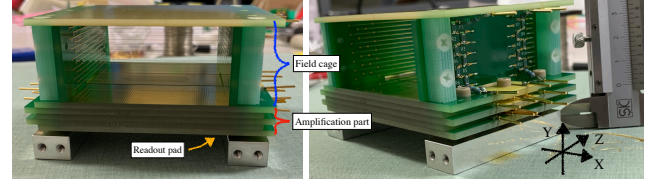


Figure 1. Photos of the Mini TPC. The details of the structure is described in the text.

is arranged around the holes of the Normal THGEM. The schematic figure of the hole positions of Normal THGEM and Flower THGEM is shown in Fig. 2.
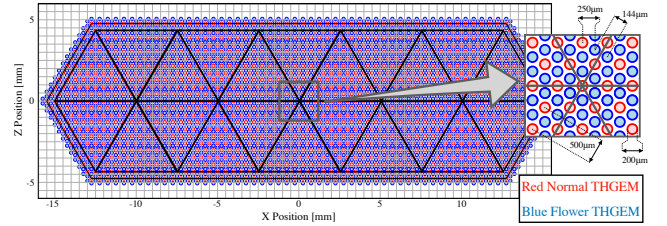


Figure 2. Design of the two THGEMs and the readout. Red and blue holes indicates that the hole positions of the Normal and Flower THGEMs, respectively. The black line shows the border of the readout pads. See the text for the details.

Equilateral triangular pads of 5 mm per side are used for the readout electrodes. There are 2 rows for the beam direction and 11 pads in each row, then 22 pads in total. In the Mini TPC, the position in the readout plane is determined from the weighted average of the amount of charges which are measured by these pads, and the position along the drift field is determined from the drift velocity. The design of the readout pad is also shown in Fig. 2.
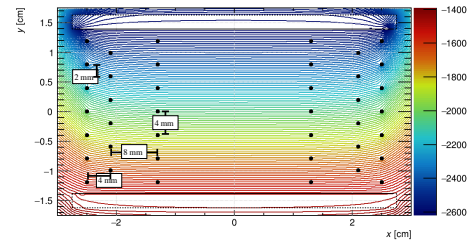


Figure 3. Electric field at the center plane in parallel to the beam path in the mini TPC calculated by using Garfield++.

The volume of the field cage is $60 \times 28 \times 50$ mm$^3$. An electric field is formed by supplying a voltage to the electrodes on the PCB and the wires using a divider circuit. The active area is not the entire field cage but $42 \times 12.1 \times 28$

mm$^3$. The field cage consists of two side PCB and gold-coated Cu-Be wires with a diameter of 50-um, as shown in the Fig. 1. The divider circuit and 250 $\mu$m wide electrodes with a 2 mm pitch are mounted on the PCBs. The positions of the wires are optimized to form the uniform field as described below. As shown by the black dots in Fig. 3, three layers of 4-mm pithced wires are attached to the side PCBs. The distances between the inner and the middle is 8 mm, and one between the middle and the outer is 4 mm. The middle layer is displaced by 2 mm.

The electric field was simulated by using the finite element method with Garfield++. Figure 3 shows the simulation results at the center plane in parallel to the beam axis. As can be seen in Fig. 3, the largest distortion in the active region can be seen at the edge of the active region, where the largest distortion is below 1%.
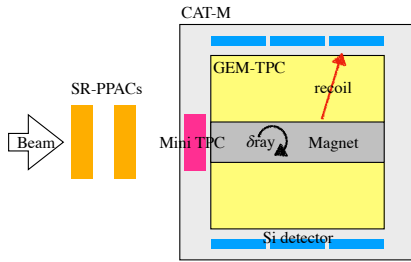


Figure 4. Experimental Setup

Figure 4 shows the setup for resolution evaluation. The Mini TPC is located upstream of the CAT-M field cage, and the beam particles are injected into the CAT-M field cage after passing through the Mini TPC. The chamber is filled with D2 gas at 40 kPa. The GET system is used for the readout system. In addition, two SRPPACs were installed upstream of the CAT chamber to evaluate the Mini TPC resolution by comparing the extrapolated positions with those of the two SRPPACs.
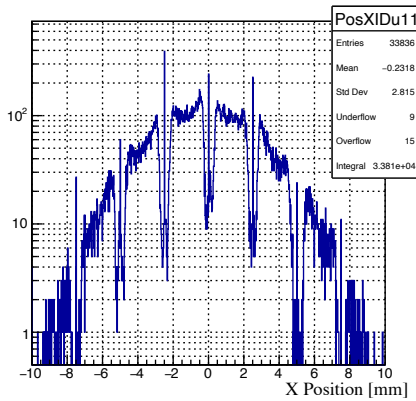


Figure 5. Position distribution by weighted average

The experiments were performed on HIMAC. The beam particles were $^{136}$Xe at 115 MeV/u and the beam intensity was 1 kppp. The position in the Mini TPC was determined by weighted average of the measured charge at the position of the pad. Figure 5 shows the measured position of the Mini TPC in the horizontal direction. In Fig. 5, sharp peaks can be seen at 2.5mm pitch intervals. This gap is caused by the inability to measure charges on adjacent pads due to low

gain, and the distance of the gap corresponds to the distance of the center of gravity between adjacent pads. Especially when the beam passes near the pad for center of gravity, the induced charge on adjacent pad is relatively small, so a low gain makes it impossible to measure the charge. Therefore, this means that if the beam particles pass near the center of gravity of the pad, the accuracy of position determination will be poor.

The position resolution was evaluated from the difference between the extrapolated position by SRPPACs and the position of Mini TPC. The left figure of Fig. 6 shows the distribution of the difference between the extrapolated positions and measured position, using only the first row of pads of the Mini TPC, and the right figure shows the distribution when only the second row of pads of the Mini TPC is used. The deviation of these distributions represents the convoluted position resolution of SRPPAC and Mini TPC. Assuming that the position resolutions of the two SRPPACs are the same, the position resolution of the Mini TPC is evaluated to be $\sigma_X = 600$ ̄m and $\sigma_Y = 400$ ̄m, respectively for horizontal (X) and vertical (Y) direction. The assumed resolution of SRPPAC is 150 ̄m in the X direction and 165 ̄m in the Y direction, the same values as those reported in the development of SRPPAC [5].
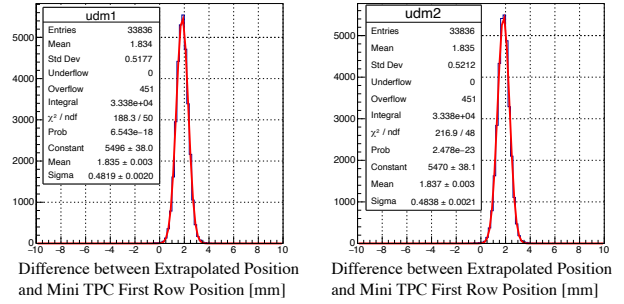


Figure 6. Correlation with extrapolated position.

In this study, we have newly developed a compact TPC that can measure beam particles in the vicinity of the reaction point. When the beam intensity was low, the positional resolutions of $\sigma_X = 600$ ̄m and $\sigma_Y = 400$ ̄m have been achieved. On the other hand, the position resolution is found to depends on the position. In the next step of the development, the performance with high-intensity beams and the position dependence of the position resolution will be evaluated.

## References

[1] J. M. Lattimer *et al.*, Phys. Rep. **333-334**, 121-146, (2000).
[2] J. Piekarewicz *et al.*, Phys. Rev. C. **79**, 054311 (2009) .
[3] K.B. Howard *et al.*, Phys. Lett. **B 807**, 135608 (2020) .
[4] S. Ota *et al.*, CNS Annual Report 2017, **97**, 41, (2019).
[5] S. Hanai *et al.*, CNS Annual Report 2019. **99**, 034303 (2020).

# Constraining the Primordial Lithium Abundance: New Cross-Section Measurement of the $^7$Be + $n$ Reactions Updates the Total $^7$Be Destruction Rate

S. Hayakawa[a] M. La Cognata[b] L. Lamia[b,c,d] H. Yamaguchi[a] D. Kahl[e,f] K. Abe[a] H. Shimizu[a]
L. Yang[g,a] O. Beliuskina[h,a] S. M. Cha[o,i] K. Y. Chae[i] S. Cherubini[b,c] P. Figuera[b] Z. Ge[h,q]
M. Gulino[b,j] J. Hu[k] A. Inoue[l] N. Iwasa[m] A. Kim[n] D. Kim[o,n] G. Kiss[p,q] S. Kubono[q,k,a]
M. La Commara[r,s] M. Lattuada[b,c] E. J. Lee[i] J. Y. Moon[o] S. Palmerini[t,u] C. Parascandolo[r]
S. Y. Park[n] V. H. Phong[q] D. Pierroutsakou[r] R. G. Pizzone[b] G. G. Rapisarda[b] S. Romano[b,c,d]
C. Spitaleri[b,c] X. D. Tang[k] O. Trippella[t,u] A. Tumino[b,j] and N. T. Zhang[k]

[a]Center for Nuclear Study, Graduate School of Science, University of Tokyo
[b]Istituto Nazionale di Fisica Nucleare - Laboratori Nazionali del Sud
[c]Department of Physics and Astronomy "Ettore Majorana", University of Catania
[d]Centro Siciliano di Fisica Nucleare e Struttura della Materia, CSFNSM
[e]Extreme Light Infrastructure – Nuclear Physics, IFIN-HH
[f]School of Physics and Astronomy, University of Edinburgh
[g]China Institute of Atomic Energy
[h]Department of Physics, University of Jyväskylä
[i]Department of Physics, Sungkyunkwan University
[j]Faculty of Engineering and Architecture, Kore University of Enna
[k]Institute of Modern Physics, Chinese Academy of Sciences
[l]Research Center for Nuclear Physics, Osaka University
[m]Department of Physics, Tohoku University
[n]Department of Physics, Ewha Womans University
[o]Institute for Basic Science (IBS)
[p]Institute for Nuclear Research (Atomki)
[q]RIKEN Nishina Center
[r]Istituto Nazionale di Fisica Nucleare - Section of Naples
[s]Department of Physics 'E. Pancini', University of Naples Federico II
[t]Istituto Nazionale di Fisica Nucleare - Section of Perugia
[u]Department of Physics and Geology, University of Perugia

This is condensed from the article in Astrophys. J. Lett. **915**, L13 (2021) [1].

Big Bang nucleosynthesis [2, 3] is a critical probe to understand the early universe, describing the primordial production of light nuclides. However, the cosmological lithium problem (CLP) stems from the outstanding discrepancy between theoretical predictions and astronomical observations of primordial lithium abundances, which is still an open issue to be challenged by astronomy, nuclear physics and non-standard cosmology. For the radiogenic production of $^7$Li, increase and decrease mechanisms of $^7$Be plays a pivotal role in the Big Bang nucleosynthesis (BBN). Despite of several recent experimental progresses [4–11], the data for neutron-induced $^7$Be destruction processes were still sparse, and especially lacked information on the contributions of transitions to the $^7$Li excited states.

In this work, we have determined the $^7$Be($n,p_0$)$^7$Li (going to the $^7$Li ground state), $^7$Be($n,p_1$)$^7$Li$^*$ (going to the $^7$Li first excited state) and the $^7$Be($n,\alpha$)$^4$He reaction cross sections by means of the Trojan Horse method (THM [12]), which enables us to measure neutron-induced reactions via substitutional reactions thanks to quasi-free mechanism. We performed the experiment at Center-for-Nuclear-Study RI Beam separator (CRIB [13]), which provided a $^7$Be RI beam at 3.16 MeV/nucleon on target with a typical intensity of $1 \times 10^6$ pps. The $^7$Be beam was tracked by two PPACs, irradiating a 64-$\mu$g/cm$^2$-thick deuterated polyethylene (CD$_2$) target, and the $^2$H($^7$Be,$^7$Li $p$)$^1$H and $^2$H($^7$Be,$2\alpha$)$^1$H THM reactions were observed by six $\Delta E$-$E$ silicon telescopes with $45 \times 45$-mm$^2$ active areas, surrounding the target at distances of 20 cm symmetrically to the beam axis at forward angles $\pm 12°$, $\pm 34°$ and $\pm 56°$. We confirmed the predominance of the quasi-free mechanism by analyzing the shape of the observed $p$-$n$ momentum distributions for both three-body reaction channels. By reconstructing the $Q$-value spectra from the observed $^7$Li-$p$ coincidence, we identified the $^7$Be($d$,$^7$Li$^*$ $p_1$)$^1$H reaction channel with a significant yield. The normalized cross sections multiplied by $\sqrt{E_{c.m.}}$ of the $^7$Be($n,p_0$)$^7$Li, $^7$Be($n,p_1$)$^7$Li$^*$ and $^7$Be($n,\alpha$)$^4$He reaction channels are shown in Figure 1. The present and the previous data were analyzed together by a multi-channel $R$-matrix fit with AZURE2 [14] consistently with the $^8$Be resonance structure. We introduced nine resonances at the known excited states and one background pole, and identified that the first four resonances above the $n$ threshold mostly characterized the cross section behaviors

around BBN energy region, specified by arrows with spins and parities in Fig. 1. The fitted curves to the $^7\text{Be}(n,p_0)^7\text{Li}$, $^7\text{Be}(n,p_1)^7\text{Li}^*$ and $^7\text{Be}(n,\alpha)^4\text{He}$ channels are also shown in Fig 1. The $R$-matrix analysis concluded a slightly smaller $^7\text{Be}(n,p_0)^7\text{Li}$ cross sections with a better uncertainty evaluation than those of Damone2018 [4], and quantified the $^7\text{Be}(n,p_1)^7\text{Li}^*$ contribution in the BBN energy range for the first time.

Figure 2 shows the $^7\text{Be}(n,p)^7\text{Li}$ reaction rates relative to that of [19]. Their uncertainties are represented by shaded bands. One can see that the present $p_0$ rate appears significantly lower than Damone2018 $p_0$, and also with much improved uncertainty in the BBN temperature range as expected from the $R$-matrix analysis. Our recommended $p_0 + p_1$ rate is ultimately comparable to Damone2018 $p_0$ in the BBN range, but with different temperature dependence due to the $(n,p_1)$ contribution.

We have then calculated the $^7\text{Li/H}$ abundances by using one of the most recent BBN codes PRIMAT [3], replacing the default $^7\text{Be}(n,p)^7\text{Li}$ reaction rate Descouvemont2004 [21] with the present $p_0 + p_1$ rate, without changing any other initial conditions. We highlight that the present $p_0 + p_1$ rate yields a significantly smaller $^7\text{Li/H}$ value $(5.18^{+0.22}_{-0.25} \times 10^{-10})$ than that with Descouvemont2004 $p_0$ $(5.63^{+0.22}_{-0.24} \times 10^{-10})$ by about one tenth or 2 standard deviations at the known baryon-to-photon number density ratio $\eta = 6.09 \times 10^{-10}$ [3] determined from the cosmic microwave background observation. It also significantly improved the uncertainty compared to that of Damone2018 [4] $(5.26^{\pm 0.40} \times 10^{-10})$. Therefore, the recommended rate may impose a more strict constraint on the primordial $^7\text{Li/H}$ abundance owing to the reevaluation of the $(n,p_0)$ uncertainty and the first-ever quantified $(n,p_1)$ contribution, which should be adopted in future BBN investigations although we obviously need additional contributions to get closer to the observed $^7\text{Li/H}$ value $1.58 \pm 0.3 \times 10^{-10}$ [22]. We expect that the present nuclear-physics data would offer a less uncertain foundation to further theoretical investigations for the complete CLP solution.

Figure 1. The present cross sections multiplied by $\sqrt{E_{\text{c.m.}}}$ of the $^7\text{Be}(n,p_0)^7\text{Li}$, the $^7\text{Be}(n,p_1)^7\text{Li}^*$ and the $^7\text{Be}(n,\alpha)^4\text{He}$ reactions are shown as open red circles, blue triangles, green squares, respectively. The previous experimental data and evaluations [4,5,7–11,15–18] are also plotted for comparison. The solid lines are the present $R$-matrix fits with light-colored bands as their uncertainties.
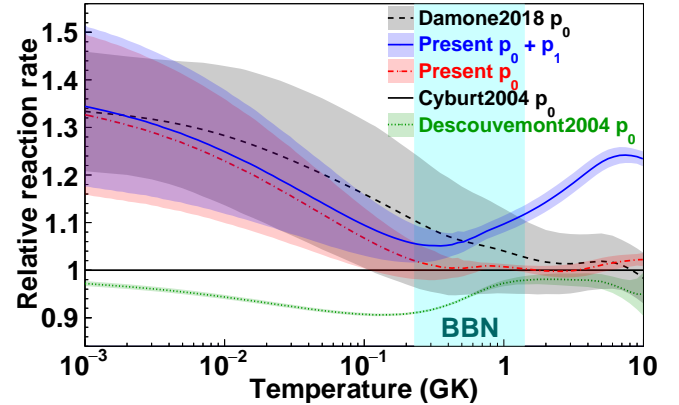


Figure 2. Comparison of the previous (Damone2018 [4], Descouvemont2004 [21]) and the present $^7\text{Be}(n,p)^7\text{Li}$ reaction rates relative to that of Cyburt2004 [19] together with uncertainties in light-colored bands.

**References**

[1] S. Hayakawa *et al.*, Astrophys. J. Lett. **915**, L13 (2021).

[2] R. H. Cyburt *et al.*, Rev. Mod. Phys. **88**, 015004 (2016).

[3] C. Pitrou *et al.*, Phys. Rep. **754**, 1 (2018).

[4] L. A. Damone *et al.*, Phys. Rev. Lett. **121**, 042701 (2018).

[5] I. Tomandl *et al.*, Phys. Rev. C, **99**, 014612 (2019).

[6] N. Iwasa *et al.*, Phys. Rev. C, **103**, 015801 (2021).

[7] S. Q. Hou *et al.*, Phys. Rev. C **91**, 055802 (2015).

[8] M. Barbagallo *et al.*, Phys. Rev. Lett. **117**, 152701 (2016).

[9] T. Kawabata *et al.*, Phys. Rev. Lett. **118**, 052701 (2017).

[10] L. Lamia *et al.*, Astrophys. J. **850**, 175 (2017).

[11] L. Lamia *et al.*, Astrophys. J., **879**, 23 (2019).

[12] C. Spitaleri *et al.*, Phys. Atom. Nucl. **74**, 1725 (2011).

[13] Y. Yanagisawa *et al.*, NIM A **539**, 74 (2005).

[14] R. E. Azuma *et al.*, Phys. Rev. C **81**, 045805 (2010).

[15] K. Sekharan *et al.*, NIM **133**, 253 (1976).

[16] R. R. Borchers and C. H. Poppe. Phys. Rev. **129**, 2679 (1963).

[17] C. H. Poppe *et al.*, Phys. Rev. C **14**, 438 (1976).

[18] P. Koehler *et al.*, Phys. Rev. C **37**, 917 (1988).

[19] R. H. Cyburt, Phys. Rev. D **70**, 25 (2004).

[20] A. Adahchour and P. Descouvemont, JPG **29**, 395 (2003).

[21] P. Descouvemont *et al.*, Atom. Data and Nucl. Data Tables, **88**, 203 (2004).

[22] L. Sbordone *et al.*, Astron. Astrophys. **522**, 1 (2010).

# An improved reaction rate for the $^{22}$Mg($\alpha$, p)$^{25}$Al and its implications on understanding type-I X-ray bursts

J. Hu[a], H. Yamaguchi, Y. H. Lam[a], A. Heger[b], D. Kahl[c], A. M. Jacobs[d], Z. Johnston[d], S. W. Xu[a],
N. T. Zhang[a], S. B. Ma[a], L. H. Ru[a], E. Q. Liu[a], T. Liu[a], S. Hayakawa, L. Yang, H. Shimizu,
C. B. Hamill[c], A. St J. Murphy[c], J. Su[e], X. Fang[f], K. Y. Chae[g], M. S. Kwag[g], S. M. Cha[g],
N. N. Duy[g], N. K. Uyen[g], D. H. Kim[g], R. G. Pizzone[h], M. La Cognata[h], S. Cherubini[h],
S. Romano[h], A. Tumino[h], J. Liang[i], A. Psaltis[i], M. Sferrazza[j], D. Kim[k], Y. Y. Li[a], and S. Kubono[l]

*Center for Nuclear Study, Graduate School of Science, University of Tokyo*
[a]*Institute of Modern Physics, Chinese Academy of Sciences, China*
[b]*School of Physics and Astronomy, Monash University, Australia*
[c]*School of Physics & Astronomy, University of Edinburgh, United Kingdom*
[d]*Department of Physics and Astronomy, Michigan State University, USA*
[e]*College of Nuclear Science and Technology, Beijing Normal University, China*
[f]*School of Physics, Sun Yet-sen University, China*
[g]*Department of Physics, Sungkyunkwan University, Korea*
[h]*INFN-LNS, Laboratori Nazionali del Sud, Italy*
[i]*Department of Physics & Astronomy, McMaster University, Canada*
[j]*Départment de Physique, Université Libre de Bruxelles, Belgium*
[k]*Department of Physics, Ewha Womans University, Korea*
[l]*RIKEN (The Institute of Physical and Chemical Research)*

Type I X-ray bursts (XRBs) are the most frequently observed thermonuclear explosions in galaxy [1, 2]. The $^{22}$Mg($\alpha$, p)$^{25}$Al is thought to play a critical role in XRBs and its reaction rate is predicted to have a significant impact on the light curve of XRBs [3]. However, experimental information is insufficient to deduce a precise $^{22}$Mg($\alpha$, p)$^{25}$Al reaction rate for the respective XRB temperature range.

A new measurement of $^{25}$Al+p resonant scattering was performed at CRIB [4] up to the astrophysically interested energy region of $^{22}$Mg($\alpha$, p)$^{25}$Al. Several resonances were observed in the excitation functions, and their level properties have been determined based on an R-matrix analysis [5]. In particular, proton widths and spin-parities of four natural-parity resonances above the $\alpha$ threshold of $^{26}$Si, which can contribute the reaction rate of $^{22}$Mg($\alpha$, p)$^{25}$Al, were first experimentally determined.

An improved reaction rate of $^{22}$Mg($\alpha$, p)$^{25}$Al was determined based on the level properties of the corresponding resonances, and the comparison with previous rates was shown in the Fig. 1. The NON-SMOKER rate [6] differs from ours by a factor of $\sim$ 10 from 0.4 to 1 GK, and varies up to a factor of 160 at 3 GK. There is a discrepancy of about 1 to 5 orders of magnitude between our new rate and the Matic *et al.* rate [7] for $T$ = 0.7 - 3 GK. The $^{22}$Mg($\alpha$, $p$) rate by Randhawa *et al.* [8] approximated with the `NON-SMOKER` $^{22}$Mg($\alpha$, $p$) rate divided by 8, is also shown in Fig. 1. Although our rate dose not largely deviate from the Randhawa *et al.* rate [8], we caution that their evaluation may underestimate the uncertainty due to the theoretical extrapolation.

To demonstrate the impact on the modeled lightcurve with the $^{22}$Mg($\alpha$, $p$) rate deduced from the present experiment, the GS 1826$-$24 burster was selected to perform the XRBs model calculation. The GS 1826$-$24 burster is referred to as "textbook" burster, which exhibits regular bursting behaviour with highly consistent properties from burst to burst. To quantitatively compare with the GS 1826$-$24 burster (Fig. 2), we adopt the best fit model from Jacobs *et al.* [9], which has a ratio of accreted $^1$H to $^4$He of 2.39, a CNO metal mass fraction of 0.0075, and an accretion rate of $3.325 \times 10^{-9}$ $M_\odot \mathrm{yr}^{-1}$, as our *baseline* model. We update it with the present $^{22}$Mg($\alpha$, $p$) rate to represent the *Present* model. The generated burst luminosity, $L_x$, by the 1D multizone hydrodynamic `KEPLER` code [10] is related to observational flux, $F_x$ by scaling with $\left[4\pi d^2 \xi_b (1+z)^2\right]^{-1}$, where $d$ is the distance, $\xi_b$ incorporates the possible burst-emission anisotropy, and the redshift, $z$, expands the lightcurve when transforming into an observer's frame. Instead of specifically selecting data close to the burst peak at $t=-10$ to 40 s, we impartially select all observational data of the entire burst timespan to fit our modeled bursts. The modeled bursts are averaged and fitted to the averaged lightcurve of GS 1826$-$24 epoch *Jun 1998* [11], which were recorded by the *Rossi X-ray Timing Explorer* (RXTE) Proportional Counter Array [12].

The *baseline* lightcurve at $t=16$–76 s is enhanced and the discrepancy with observed data becomes only up to 6% due to the present and lower $^{22}$Mg($\alpha$, $p$) rate, which at low temperature competes with $^{22}$Mg($\beta\nu$) decay and overcomes $^{22}$Mg($p$, $\gamma$) at higher temperature $T > 1.67^{+0.15}_{-0.13}$ GK instead of at $T > 1.16$ GK compared to the NON-SMOKER $^{22}$Mg($\alpha$, $p$) rate (Fig. 1). The alternative $J^\pi = 3^+/4^+$ rate yields only 3% deviation from the observed data at $t=16$–76 s, which is not discernible in Fig. 2. The matter flow is
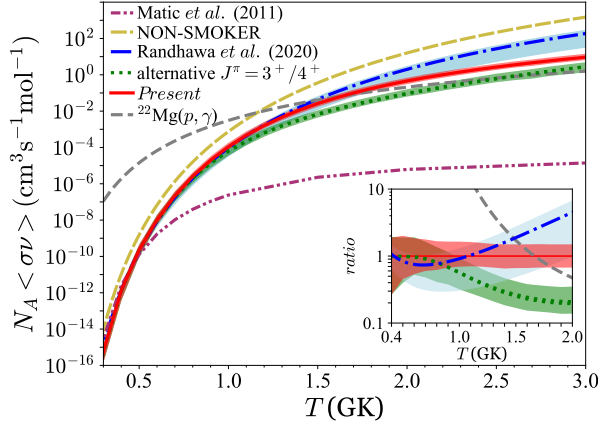
Figure 1. The $^{22}$Mg($\alpha$, p)$^{25}$Al rates. The uncertainty of the present rate (red zone) is estimated via Monte Carlo calculation considering all errors from the present experimental measurement. Both possible rates with $J^\pi$(10.875 MeV)= $3^+$ or $4^+$ are not distinguishable, plotted as a green line and labeled as ¡°alternative $J^\pi$= $3^+$ or $4^+$.¡± Randhawa et al. [8] rate uncertainty is the blue zone. Inset: the ratios of Randhawa et al., or alternative $J^\pi$= $3^+$ or $4^+$ or $^{22}$Mg(p, $\gamma$)$^{25}$Al rate to the present $^{22}$Mg($\alpha$, p)$^{25}$Al rate.

more siphoned out to $^{22}$Mg($p,\gamma$)$^{23}$Al($p,\gamma$)$^{24}$Si($\alpha,p$), enriching more proton-rich nuclei nearer to dripline past the *sd*-shell. These nuclei burn hydrogen after the burst peak and enhance the lightcurve at *t*=16–76 s, depleting hydrogen that is to be burnt by further ($p,\gamma$) reactions at later time *t*=80–150 s. Hence, the observed lightcurve profile at *t*=80–150 s is noticeably reproduced. Therefore, the present work experimentally validates the predicted lightcurve trend in Ref. [3] and enhances a state-of-the-art model to remarkably reproduce the GS 1826−24 lightcurve with mean deviation <9 %. In the latest model by Randhawa et al. [8] (the blue line in Fig. 2), a similar trend is manifested at *t*=8–64 s, however, it deviates their baseline model farther away from observation.

In summary, we performed a new measurement of $^{25}$Al+p resonant scattering with the capability to select and measure proton resonances contributing to the $^{22}$Mg($\alpha,p$) reaction at XRB temperature. The $^{22}$Mg($\alpha,p$) rate was deduced based on the level properties of the corresponding resonances. The improved nuclear physics input permits us to better reproduce the observed GS 1826−24 light curves than the previous model. For more details please refer to our published paper [13].

## References

[1] W.H.G. Lewin, J.V. Paradijs and R.E. Taam, Space Science Reviews **62** (1993) 223.

[2] H. Schatz, and K.E. Rehm, Nucl. Phys. A **777** (2006) 601.

[3] R.H. Cyburt et al., Astrophys. J. **830** (2016) 55.

[4] Y. Yanagisawa et al., Nucl. Instr. Meth. **539** (2005) 74.

[5] R.E. Azuma et al., Phys. Rev. C **81** (2010) 045805.

[6] NON-SMOKER [http://nucastro.org/nonsmoker.html].

[7] A. Matic et al., Phys. Rev. C **84** (2011) 025801.

[8] J.S. Randahawa et al., Phys. Rev. Lett. **125** (2020) 202701.

[9] A.M. Jacobs et al., Multi-zone x-ray burst reaction rate sensitivities, in *Proceedings of the Burst Environment, Reactions and Numerical Modelling Workshop, Monash Prato Centre, Tuscany, Italy* (2018), [https://burst.sci.monash.edu/bern18/].

[10] A. Heger et al., Astrophys. J. Lett. **671** (2007) L141.

[11] D.K. Galloway et al., Pub. Astron. Soc. Aust. **34** (2017) e019.

[12] D.K. Galloway et al., Astrophys. J. Suppl. Ser. **249** (2020) 32.

[13] J. Hu et al., Phys. Rev. Lett. **127** (2021) 172701.

Figure 2. The best fit *baseline* and *Present* modeled lightcurves to the observed lightcurve of epoch *Jun 1998*, and the best fit Randhawa et al. [8] lightcurves to epoch *Sep 2000*. The magnified lightcurves at the burst peak and *t*=20–70 s are shown in the left and right insets, respectively.

# Astrophysical $^{26}$Si($\alpha,p$)$^{29}$P nuclear reaction rate study

M. J. Kim,[a] K. Y. Chae,[a] S. Hayakawa,[b] S. Adachi,[c] S. M. Cha,[d] T. Chillery,[b] N. N. Duy,[a] T. Furuno,[c] G. M. Gu,[a] S. Hanai,[b] N. Imai,[b] D. Kahl,[e] T. Kawabata,[c] C. H. Kim,[a] D. Kim,[d] S. H. Kim,[a] S. Kubono,[f] M. S. Kwag,[a] J. Li,[b] N. R. Ma,[b] S. Michimasa,[b] K. Okawa,[b] K. Sakanashi,[c] H. Shimizu,[b] O. Sirbu,[e] N. K. Uyen,[a] H. Yamaguchi[b] R. Yokoyama[b] and Q. Zhang[b]

[a]*Department of Physics, Sungkyunkwan University*
[b]*Center for Nuclear Study, University of Tokyo*
[c]*Department of Physics, Osaka University*
[d]*Center for Exotic Nuclear Studies, Institute for Basic Science (IBS)*
[e]*Extreme Light Infrastructure Nuclear Physics (ELI-NP)*
[f]*RIKEN Nishina Center*

X-ray burst is a stellar phenomenon that occurs in a certain type of binary star system. During the X-ray bursts, heavy elements up to the Sn-Sb-Te region can be synthesized within few seconds. The study of $\alpha$ $p$-process, which is composed of alternating ($\alpha$, $p$) and ($p$, $\gamma$) reactions, is important to understand the mechanism of X-ray burst. Due to the difficulties of implementing experiments, most of the important reaction rates for $\alpha$ $p$-process reactions are experimentally less understood.
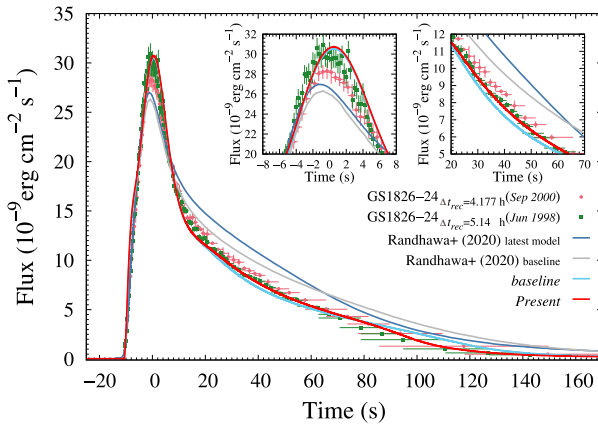
The $^{26}$Si($\alpha$, $p$)$^{29}$P reaction rate is related with abundance of $^{26g}$Al ($T_{1/2} = 7 \times 10^5$ y). During decay of $^{26}$Al, the characteristic 1.808-MeV $\gamma$-rays are emitted. By comparing the observational results and experimental predictions, the $\gamma$ rays may provide useful information about nucleosynthesis. The effect of nuclear reaction rate variations in the abundances of nuclei in the X-ray burst were investigated by Parikh et al. [1]. The results indicate that the $^{26}$Si($\alpha$, $p$)$^{29}$P reaction rate significantly affects the abundance of $^{26g}$Al.

Another motivation for the $^{26}$Si($\alpha$, $p$)$^{29}$P reaction measurements comes from the light curves of X-ray burst. Cyburt et al. [2] investigated the many thermonuclear reactions that might affect the shape of the light curve of X-ray bursts. Among the various nuclear reactions, the $^{26}$Si($\alpha$, $p$)$^{29}$P reaction was classified as one of the 'Category 1' and 'Category 2' reactions for the single zone and multi zone model, respectively, which means that the $^{26}$Si($\alpha$, $p$)$^{29}$P reaction plays a significant role in understanding the burst light curves.

To estimate the $^{26}$Si($\alpha$, $p$)$^{29}$P reaction rate, the properties of energy levels in $^{30}$S should be studied. Considering the Gamow window of the reaction at X-ray burst temperatures ($T$ = 1 - 3 GK), $^{30}$S energy levels at the energy range of $E_x$ = 10 - 14 MeV are important for the astrophysical reaction rate. Although energy levels in $^{30}$S have been studied many times over the years [3–6], the levels located above the $\alpha$ threshold are not well studied. In Ref [6], several energy levels in the Gamow window region were studied through the $^{28}$Si($^3$He, $n$)$^{30}$S- and $^{32}$S($p$, $t$)$^{30}$S- transfer reaction measurement. The energy levels only up to about $E_x$ = 12.4 MeV were investigated. Moreover, the spectroscopic factors of the levels above $E_x$ = 10 MeV could not be
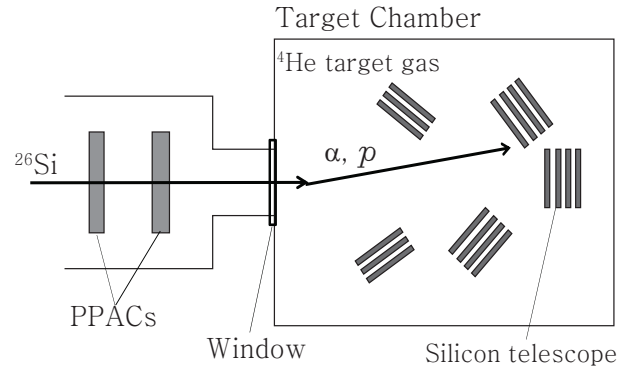


Figure 1. A schematic diagram of the experimental setup at the last focal plane is shown.

constrained.

In order to study the energy levels in $^{30}$S, the $^{26}$Si($\alpha$, $\alpha$)$^{26}$Si resonant scattering was measured in inverse kinematics at Center for Nuclear Study Radioactive Ion Beam Separator (CRIB) [7] of the University of Tokyo. By adopting the thick target method [8], wide energy range of $^{30}$S levels ($E_x$ = 10.9 - 16.3 MeV) could be investigated. The radioactive $^{26}$Si($T_{1/2} \sim 2.23$ s) beam was produced through the $^3$He($^{24}$Mg, $^{26}$Si)$n$ reaction. A primary $^{24}$Mg$^{8+}$ beam from the AVF cyclotron at $E_{beam}$ = 7.56 MeV/u bombarded the $^3$He gas target of 1.15 mg/cm$^2$. The $^3$He gas was confined in a gas cell by 3-$\mu$m-thick Mo foils. The gas cell was cooled by liquid nitrogen [9] to increase areal density of the target. To separate the $^{26}$Si$^{14+}$ ions from rest of secondary particles, the magnetic rigidity of 0.571 Tm and a slit of 20 $\pm$ 10 mm placed at the momentum dispersive focal plane were set. The Wien Filter voltage of $\pm$ 86 kV were also set to increase $^{26}$Si$^{14+}$ beam purity.

A schematic diagram of the experimental setup at the last focal plane of CRIB is shown in Figure 1. The $^{26}$Si beams at the energy of 2.01 MeV/u were delivered to the target chamber. The position and time information of beam particles were measured by two Parallel Plate Avalanche Counters (PPACs). To identify the $^{26}$Si beam particles, the time-of-flight (TOF) between the AVF cyclotron and PPAC was used. The TOF between two PPACs was also used. The typical $^{26}$Si beam intensity was $1.4 \times 10^4$ pps and the beam
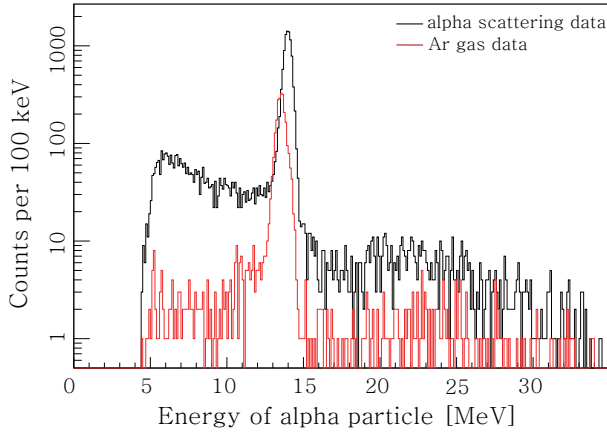
Figure 2. A preliminary alpha energy spectrum is shown. The black solid histogram and red solid histogram indicate the $\alpha$ particles energies from $^4$He- and Ar-gas runs, respectively.

**References**

[1] A. Parikh, J. Jose, F. Moreno, and C. Iliadis, Astrophys. J. Suppl. Ser. **178**, (2008) 110.

[2] R.H. Cyburt *et al.* Astrophys. J. **55** (2016) 830.

[3] D. W. Bardayan *et al.* Phys. Rev. C **76** (2007) 045803.

[4] K. Setoodehnia *et al.* Phys. Rev. C **82** (2010) 022801.

[5] G. Lotay *et al.* Phys. Rev. C **86** (2012) 042801.

[6] S. Almaraz-Calderon *et al.* Phys. ReV. C **86** (2012) 065805.

[7] Y. Yanagisawa et al., Nucl. Inst. Metho. Phys. Res. A, **539**, (2005) 74.

[8] K. P. Artemov *et al.*, Sov. J. Nucl. Phys. **52** (1990) 408.

[9] H. Yamaguchi *et al.*, Nucl. Inst. Meth. Phys. Res. A **589** (2008) 150.

purity was $\sim$ 18.8 %. The reaction target chamber was filled with $^4$He gas target at 250 Torr. The aluminized mylar window with a thickness of 10-$\mu$m was used to isolate the $^4$He gas from the vacuum.

The recoiling particles were identified by five silicon detector telescopes using the standard energy loss techniques. The W1-type silicon detectors of the Micron Semiconductor were used to form the telescopes. The W1-type silicon detector has $50 \times 50$ mm$^2$ active area and 16 strips. Each strip of silicon detectors was calibrated by using $\alpha$-emitting source. The $\alpha$ and proton beams at various energies (6, 10, 16, 19, 21 and 24 MeV) were also used for the calibration. In order to investigate backgrounds, the measurement with 53.5 Torr of noble argon gas target was also performed.

To identify the events coming from the $^{26}$Si($\alpha$, $\alpha$)$^{26}$Si reactions, the coincidence between the $\alpha$ particles and the $^{26}$Si beams was required. By requiring the coincidence, the events from contamination could be rejected. To estimate the contribution from the beam-like $\alpha$ particles, the timing gate for alpha particles was applied. The preliminary result for the $\alpha$ energy spectrum obtained at the 0 degree telescope is shown in Figure 2. The spectrum obtained with argon gas target is also shown in the figure as the red solid line. The strong peak near $E_\alpha$ = 14 MeV is evident in the both spectra, which is originated from the contaminations in the secondary beam. Comparing the normalized background run and the $^4$He gas run, the effects of contaminated beam particles could be subtracted.

To obtained the excitation function of $^{26}$Si($\alpha$, $\alpha$)$^{26}$Si reaction, the $\alpha$ energy will be converted to the center-of-mass energy of the $^{26}$Si + $\alpha$ system ($E_{\text{c.m.}}$) by considering the kinematics of reaction and the energy loss of particles in the gas target. Using the position and energy information of the beam and alpha particles, the reaction vertex will be also reconstructed. Comparing the empirical excitation function with the theoretical R-matrix calculations, the information of levels in $^{30}$S such as excitation energy, spin, parity and $\alpha$ partial width will be extracted. The $^{26}$Si($\alpha$, $p$)$^{29}$P reaction rate will be obtained based on the level information.

# Development of the cold Francium source with laser cooling technique for the atomic electric dipole moment search

S. Nagase, H. Nagahama[a], K. Nakamura[a], T. Nakashita[b] and Y. Sakemi[a]

*Graduate School of Science, University of Tokyo*
[a]*Center for Nuclear Study, University of Tokyo*
[b]*Graduate School of Arts and Sciences, University of Tokyo*

Precise laser spectroscopy of radioisotopes has a potential to lead to the discovery of nuclear structure and fundamental symmetries. In particular, it is known that Fr has an enhancement effect of permanent electric dipole moment (EDM) of electrons to be 799 times [1]. The effect of eEDM appears as a slight shift of resonant frequency between the atomic energy levels. To detect the frequency shift it is necessary to cool and trap Fr atoms and to do high-precision laser spectroscopy. A laser cooling experiment using unstable isotopes is challenging because of its short lifetime and low production rate. In this report, a description of a magneto-optical trap (MOT) apparatus we have developed is provided and an evaluation result of our Fr production-trapping beamline is reported.

MOT is a technique that produces cooled atoms using magnetic gradient and circularly polarized laser. In order to create magnetic gradient in 3D for confining cooled atoms, anti-Helmholtz coil is often used. The loss rate from the trap depends on the pressure of the trap region due to collisions between trapped atoms and background gas so a pressure below $10^{-9}$ Torr is typically required. The lifetime of the trapped atoms at $10^{-9}$ Torr is a few seconds. The producing rate of Fr is very low so we should prepare Ultra-High Vacuum (UHV) pressure equipment.

Shown in Figure 1, the coils are installed in the vacuum apparatus, which makes the coil size small. We need less current to produce magnetic gradient due to the compact size coils. The outside diameter of the bobbin used to wind the coil is 11 mm and the height is 18 mm. The magnetic gradient generated by the anti-Helmloltz coils was 9.1 G/cm for an applied current of 0.479 A.

The trap apparatus is shown in Figure 2. To produce UHV system we use turbomolecular pump, sputter ion pump, and non evaporable getter (NEG) pump. NEG pump which is made of active metals and alloys can remove molecular gas such as $H_2O$, CO, $CO_2$, $O_2$, and $N_2$ using chemical changes that occur on the active surface. Inert gases such as noble gases cannot be pumped with NEG, but the sputter ion pump which is connected to the NEG can remove these gases. The benefits of using the NEG pump are that it does not need power supply and does not vibrate with mechanical motion. The pressure of the system reached below $10^{-11}$ Torr using these pumps and the lifetime of the trapped $^{87}$Rb atoms achieved 60 seconds.

Unlike other experiments using stable atoms, the production rate of Fr is very small so the number of trapped Fr atoms may be very small. Therefore, an observation system that can detect slight fluorescence emitted by trapped atoms is necessary. Figure 3 shows the construction of the obser-
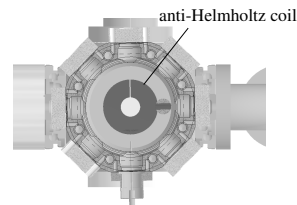


Figure 1. Sketch of anti-Helmholtz coils. These coils are mounted inside the MOT apparatus.
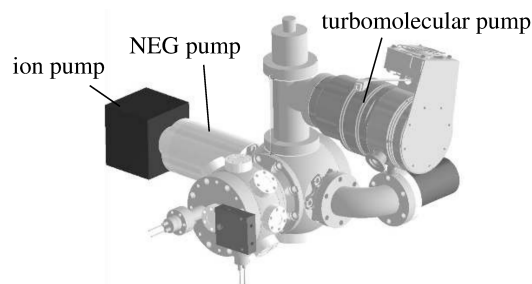


Figure 2. Magneto-optical trap apparatus for trapping Fr atoms. A turbomolecular pump, sputter ion pump, non evaporable pump are indicated.

vation optical system we assembled. When we detect the fluorescence of trapped atoms, the major noise is laser light scattered on the viewports. The trapping laser light power is typically a few mW and the fluorescent power emitted by a few atoms in the MOT is below pW using our detection system. To reduce the scattered light we installed a pinhole that shut off the light coming in except for the trap center and an anti-reflective coating is applied to the viewports. In addition, we use a bandpass filter (BPF) that transmits the light whose wavelength is the same as fluorescent light emitted by trapped atoms. The fluorescence is detected using a CMOS camera and a photomultiplier (PMT). With the CMOS camera, we define a region of interest and we achieved the detection of the fluorescent light emitted by a few atoms in the trap region.

We installed the MOT apparatus to our beamline. Then we did the test of the beamline using rubidium (Rb) atoms and evaluated the efficiency of the atom production, transport, and trapping. Main components of our beamline are a surface ionizer, neutralizer, and MOT apparatus. In the sur-
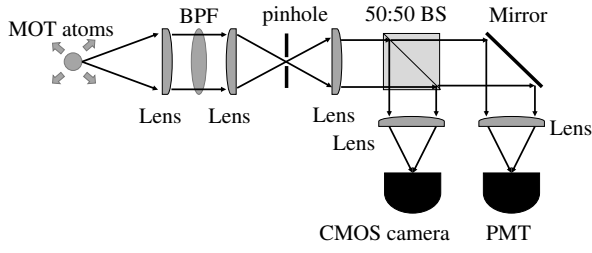
Figure 3. Schematic diagram of the optical system (BPF = band-pass filter, BS = beam splitter, PMT = photomultiplier). The fluorescence of trapped atoms is detected by two detectors, the CMOS camera and PMT.



Figure 4. Typical detection signal of trapped atoms by the CMOS camera (a) and PMT (b). An exporsure time of the CMOS camera was set 500 ms.

face ionizer, Fr atoms are produced via the nuclear fusion reaction, $^{197}\text{Au}(^{18}\text{O}, xn)^{215-x}\text{Fr}$, and are extracted using electrodes. We can produce a $^{210}\text{Fr}$ ion beam of $5 \times 10^6$/s [2]. The beam energy is typically 100 eV. $^{210}\text{Fr}$ ions are accumulated on the surface of a yttrium (Y) foil for 3 minutes. After accumulating $^{210}\text{Fr}$ ions Y is moved to the position under the MOT apparatus and is heated to 800 K using an infrared (IR) heater. $^{210}\text{Fr}$ atoms are desorbed from Y surface as neutral atoms since the work function of Y is smaller than the ionization potential of Fr. Then neutral $^{210}\text{Fr}$ atoms pass through a capillary with anti-absorption coating on the inside wall and reach the MOT chamber.

Frequency-stabilized lasers are needed for the MOT of alkali atoms. We use a Ti:sapphire laser as a trapping laser (Fr D2 line, 718 nm) and a homemade interference-filter type external-cavity diode laser (ECDL) as a repumping laser (Fr D1 line, 817 nm) to trap Fr atoms. In addition, we use a homemade Littrow-type ECDL (Rb D2 line, 780 nm) and DFB laser (Rb D1 line, 795 nm) to trap Rb atoms. These lasers are simultaneously stabilized using a wavelength meter. The lasers are overlapped and divided into three passes for 3D MOT, then propagate to the MOT apparatus through 400 m plus 40 m polarization maintaining (PM) fibers [3]. The 40 m PM fibers are connected to three collimators attached to the MOT apparatus and the collimators expand the laser beam diameter to 17 mm. The collimator, a polarizing beam splitter, a half-wave plate, a quarter-wave plate, and an aperture are connected using a cage system. The aperture shapes the beam diameter by 10 mm. The trapping laser power is 14 mW/axis and the repumping laser power is 1 mW/axis. The magnetic gradient is 13 G/cm. The pressure of the trap region is $10^{-10}$ Torr and gets worse to $10^{-8}$ Torr during the heating of the Y foil.

Optimization and evaluation of the beamline are performed using $^{87}\text{Rb}$ atoms provided by a Rb dispenser that is installed in the Fr ionizer. Figure 4 (a) shows a picture of the trapped $^{87}\text{Rb}$ atoms with the CMOS camera and Figure 4 (b) shows a current signal from the PMT. We have confirmed that the surface ionizer, the neutralizer, and the MOT apparatus functioned reasonably using $^{87}\text{Rb}$ atoms. It is possible to measure the beam intensity of ions extracted from the Au target by detecting the beam current from a Faraday cup. We estimated that $4.7 \times 10^{11}$ $^{87}\text{Rb}$ ions accumulated on the surface of the Y foil. Then we moved the
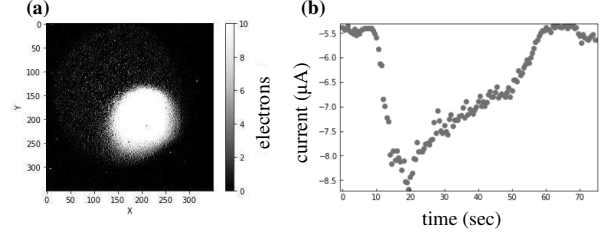
Y foil under the MOT apparatus and heated the Y foil for five seconds. As a result, we observed 1300 trapped atoms. Therefore the ratio of the number of accumulated atoms on the Y foil to the number of trapped atoms is estimated at about $10^{-9}$. Here the current detected by the Faraday cup attributed only to Rb atoms. The number of atoms accumulated on the Y foil can be estimated more precisely using $^{210}\text{Fr}$ atoms by detecting alpha particles that are produced by the decaying $^{210}\text{Fr}$ nuclei. A detection chamber of alpha decay is attached to our beamline. A silicon semiconductor detector (SSD) is put in the detection chamber to detect the alpha particles which come from $^{210}\text{Fr}$ nuclei on the Y foil. Before and after heating the Y foil, it is moved under the SSD in the detection chamber and a count rate is measured for a few seconds. We confirmed that $10^8$ $^{210}\text{Fr}$ atoms accumulated on the Y foil and at most 30 % of the $^{210}\text{Fr}$ atoms are desorbed from the Y foil by heating. During a sequence of the Fr production, accumulation, and heating of the Y foil, we constantly measured the fluorescent signal with the CMOS camera and PMT. We compared the signal before and after heating the Y foil but we have not observed significant differences which means that the amount of trapped Fr atoms was not enough to observe with our fluorescence detection system.

We developed and installed an MOT apparatus. To produce laser cooled Fr source, optimization of the beamline is in progress.

## References

[1] N. Shitara, N. Yamanaka, B.K. Sahoo, T. Watanabe, and B.P. Das, J. High Energy Phys. **2021** (2021) 124.

[2] N. Ozawa, H. Nagahama, T. Hayamizu, K. Nakamura, M. Sato, S. Nagase, Y. Kotaka, K. Nakamura, K. S. Tanaka, M. Otsuka, T. Aoki, Y. Ichikawa, A. Takamine, H. Haba, H. Ueno and Y. Sakemi, RIKEN Accel. Prog. Rep. **54** (2021) 117.

[3] K. Nakamura, S. Nagase, T. Nakashita, T. Hayamizu, T. Aoki, H. Nagahama, N. Ozawa, M. Sato, K. Yamane, M. Fukase, D. Uehara, A. Takamine and Y. Sakemi, J. Phys.: Conf. Ser. **2249** (2022) 012010.

# Experimental Nuclear Physics: PHENIX Experiment at BNL-RHIC and ALICE Experiment at CERN-LHC

# Global commissioning of the ALICE upgrade in 2021

T. Gunji

*Center for Nuclear Study, Graduate School of Science, The University of Tokyo, Japan*

## 1. Introduction

ALICE is one of the large experiments at the Large Hadron Collider (LHC) in CERN [1]. ALICE is designed to study the strongly interacting matter composed of deconfined quarks and gluons, called quark-gluon plasma, at extreme energy densities by ultra-relativistic heavy-ion collisions. The ALICE detector consists of central barrel and a forward muon spectrometer and provides the capabilities to measure as many observables as possible for a wide coverage of transverse momentum and pseudo-rapidity [1].

A major upgrade of the ALICE detector has been conducted during the 2nd Long Shutdown (LS2, 2019-2021) of the LHC. ALICE will inspect 50 kHz Pb-Pb collisions in Run3 and 4 (2022-2029) and record all minimum bias events delivered by the LHC, which increases the integrated luminosity of Pb-Pb collisions by $\times 50$-100 compared to that in Run 2. The 6 layers of silicon detectors (ITS) are replaced with a 7 layers of new silicon pixel detectors. This new tracker is made up of about 25000 Monolithic Active Pixel Sensors with fast readout and with reduced material thickness down to 0.3% (inner layers) - 1% (outer layers) of the radiation length and a granularity of $28 \times 28$ $\mu m^2$ [2]. The second major upgrade is to replace the MWPC-based readout chambers of the Time Projection Chamber (TPC) with Micro Pattern Gaseous Detectors [4]. The new readout chambers consist of stacks of 4 Gas Electron Multiplier (GEM) foils with different hole pitches to suppress ion backflow less than 1%. The third major upgrade is the new readout and online DAQ system, which handles 3 TB/s raw data rate [5]. This new DAQ system is called $O^2$ (Online-Offline). The data is read out continuously from detectors and is reconstructed in several steps synchronously in the First Level Processors (FLP) and Event Processing Nodes (EPN) to compress the data rate down to $\sim$100 GB/s. Traditional CPUs are unable to handle such huge data rate for synchronous reconstruction and therefore ALICE employs GPUs to accelerate the processing in the EPN. The EPN farm consists of 250 computing servers and each server houses 8 GPUs (AMD MI-50 GPU).

The author has been an ALICE Run Coordinator since 2019. In 2021, the author was fully responsible to complete the ALICE global commissioning and to validate data taking and processing with the new systems and infrastructure using $pp$ collisions at $\sqrt{s} = 900$ GeV, which was conducted as a part of the commissioning of the LHC machine in preparation for Run 3.

## 2. ALICE Global Commissioning

After three years of the upgrade activities and installation of the ALICE upgrades, ALICE started global commissioning in July 2021 to embark on a new data-taking period. Upgraded detectors and their new readouts were integrated into $O^2$. ALICE integrated all important workflows for synchronous processing in EPNs such as the TPC clustering and tracking in GPUs, ITS clustering and tracking, and global track matching between ITS, TPC, and outer detectors. Those workflows were extensively tested using cosmic data taking in September and October and their stability was verified with the large number of EPNs (70-140 out of 250). While ALICE was progressing with cosmic data taking and full chain of $O^2$ readout validation, ITS detector was commissioned with several calibrations (noise and threshold), which were essential to preserve online tracking capabilities with high efficiencies. After the optimized threshold was deployed, fake-hit rate of the ITS was below $10^{-8}$/pixel/event. Figure 1 shows the efficiency of ITS outer barrel layers (left: bottom layers, right: top layers) as a function of track quality for cosmics. More than 99% of efficiency was achieved.
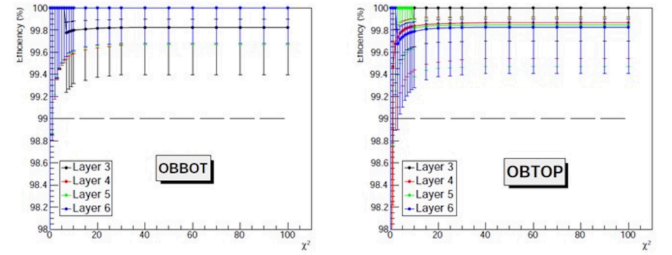


Figure 1. Hit detection efficiency for ITS outer layers as a function of cosmic track quality. Left and right shows for bottom and top ITS outer layers.

Noise performance and noise rejection in the cluster finders in the TPC were also optimized to preserve tracking and PID performances of the TPC. Moreover, krypton calibration was performed in the TPC for pad-by-pad gain equalization and a laser system was commissioned to calibrate drift velocity.

## 3. LHC Pilot Beam Tests

From middle of October, pilot beams were circulated in the LHC at the LHC injection energy corresponding $\sqrt{s} = 900$ GeV, as a part of the commissioning of the machine in preparation for Run 3. ALICE used this opportunity to understand the responses of the upgraded detectors with collisions and the performance of the new $O^2$ system as well as to advance the full offline reconstruction, global calibrations, and Run3 analysis framework.

On the first day of pilot beam collisions, ALICE commissioned two detectors providing the luminosity to the LHC. Afterwards, ALICE went into the steady continuous data

taking mode with all synchronous processing in EPN. Figure 2 shows the ALICE event display for one time frame data, which contains 128 orbits (11.5 msec) and 6 collisions on average. ITS and TPC matched tracks are shown in the central barrel, where the TPC clustering and tracking are done synchronously via GPUs in EPN. Figure 3 shows the online reconstructed energy loss $dE/dx$ in the TPC as a function of momentum, where clear separation of charged particles (e, $\mu$, $\pi$, $K$, proton, deuteron) are visible. Newly upgraded TPC shows excellent PID capabilities are preserved. Figure 4 shows the primary vertex reconstruction done synchronously by newly upgraded ITS.
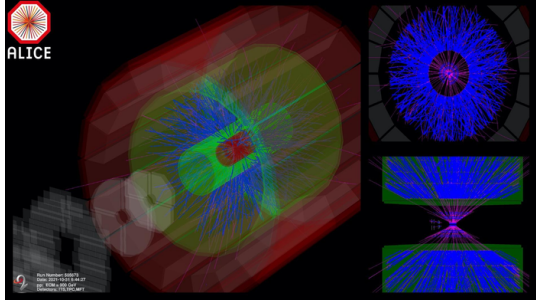


Figure 2. ALICE event display from one time frame
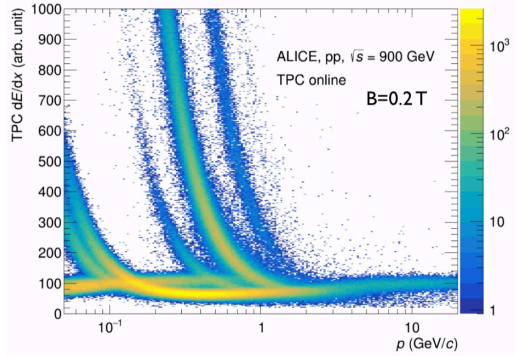


Figure 3. TPC $dE/dx$ as a function of momentum

During the pilot run, ALICE took data with three different magnet settings for Solenoid and Dipole magnets for the study of global alignment. In total, data taking lasted for 28 hours out of 42 hours of collisions, during which time ALICE accumulated sufficient statistics for making further studies. The online systems were validated with large numbers of EPNs, where stable data taking with all online processing for many hours was achieved. ALICE collected about 60 million collisions and fed into asynchronous reconstruction for further deep analysis and development of calibration and analysis framework for Run 3. Figure 5 shows the comparison of efficiency-corrected charged particle multiplicity density in $pp$ collisions at $\sqrt{s} = 900$ GeV measured in the pilot beam tests and published results, where one can see the good agreement over the measured pseudo-rapidity ranges.

The success of the LHC pilot beam tests marks a precious milestone for ALICE ensuring that detectors and new $O^2$ systems are fully operational.
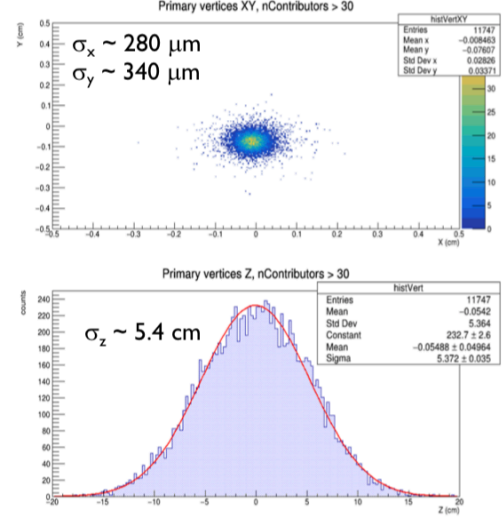




Figure 4. ITS primary vertex reconstruction in transverse plane (upper) and collision axis (lower)
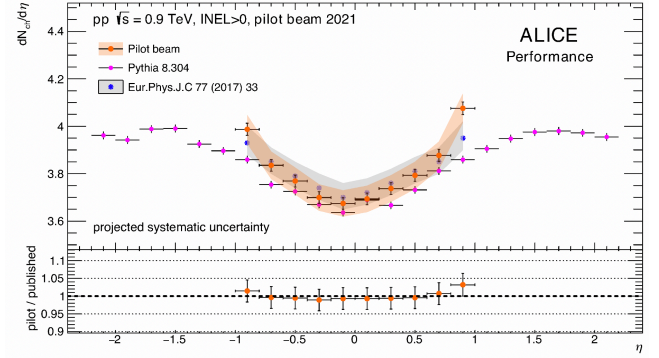


Figure 5. Charged particle multiplicity density measured in pilot beam tests

## References

[1] ALICE Collaboration, Int. J. Mod. Phys. A 29 (2014) 1430044
[2] ALICE Collaboration, CERN-LHCC-2012-013, CERN-LHCC-2013-024
[3] ALICE Collaboration, CERN-LHCC-2015-001
[4] ALICE Collaboration, CERN-LHCC-2013-020Â
[5] ALICE Collaboration, CERN-LHCC-2013-019, CERN-LHCC-2015-006

# Production of direct photons via internal conversions in Pb–Pb collisions at $\sqrt{s_{\mathrm{NN}}}$ = 5.02 TeV with ALICE at the LHC

D. Sekihata and T. Gunji

*Center for Nuclear Study, Graduate School of Science, University of Tokyo*

## 1. Introduction

The goal of performing high-energy heavy-ion collisions is to understand the properties of the quark-gluon plasma (QGP), which is a phase of matter composed of deconfined quarks and gluons under extreme conditions at high temperature and high energy density [1, 2]. Photons and dileptons are one of the tools to investigate the space-time evolution of the high-energy heavy-ion collisions. These electromagnetic probes are produced by various sources during the entire evolution and traverse the medium without strong interaction. Thus, they carry undistorted information at the time of their production [3].

Thermal Photons emitted from partonic and hadronic phases, and prompt photons produced by the initial hard scattering are called direct photons. Thermal photons carry information on the thermodynamics of the system and prompt photons are suitable for testing perturbative QCD (pQCD) calculations. Experimentally, the hadronic background is dominated and subtracted from inclusive photons by "hadronic cocktail" which simulates photons from all known hadronic decays. Photons from hadron decays are simulated based on their measured yields with detector realistic resolution. For the non-measured hadrons, their transverse momentum ($p_T$) spectra are scaled from the measured pions called $m_T$-scaling technique.

The measurement of real direct photons at low $p_T$ is challenging due to the large background from $\pi^0$ decays which amounts $\sim$ 85 % of total backgrounds, followed by $\eta \sim$ 12%, $\omega \sim$ 2% and $\eta' \sim$ 1%. Alternative approach to measure the direct photons is to measure direct virtual photons via dielectron channels. One of the advantages of dielectrons compared to real photons is that the dominant background of $\pi^0$ decays is significantly reduced by measuring virtual direct photons in the dielectron invariant mass ($m_{ee}$) region above $\pi^0$ mass 135 MeV/$c^2$. The fraction of direct virtual photons over inclusive virtual photons in the kinematic range of quasi-real photons ($p_{T,ee} \gg m_{ee}$) is expected to be equivalent to that of real photons in the mass-less limit $m_{ee} \to 0$. Therefore, the measurement of direct virtual photons decaying into dielectron is independent and complementary to that of direct real photons [4].

## 2. Analysis

In November and December of 2018, ALICE took data in Pb–Pb collisions at $\sqrt{s_{\mathrm{NN}}}$ = 5.02 TeV with enhanced triggers for central semi-central collisions. The number of events for physics analyses is 65 M in the 0-10% and 55 M in the 30-50% centrality classes respectively. In this analysis, charged particles with $p_T > 0.2$ GeV/$c$ and pseudorapidity $|\eta| < 0.8$ are selected. The tracking detectors at the central barrel of ALICE are Inner Tracking System (ITS) consisting of 6 silicon layers and Time Projection Chamber (TPC). For the electron identification, the specific ionizing energy loss in unit length dE/dx measured in ITS, TPC and the time of flight with the TOF detector are used.

In the pair analysis, there are huge combinatorial backgrounds in unlike-sign pairs (ULS: $e^+e^-$). The combinatorial background is estimated by the like-sign technique (LS: $e^+e^+$ or $e^-e^-$). Signal $S$ is defined as

$$S = N_{+-} - 2R \times \sqrt{N_{++} \cdot N_{--}},$$

where $R$ is a correction factor for different detection efficiencies between electrons and positrons obtained from the event mixing technique by

$$R = \frac{N_{+-}^{\mathrm{mix}}}{2 \times \sqrt{N_{++}^{\mathrm{mix}} \cdot N_{--}^{\mathrm{mix}}}}$$

The reconstruction efficiency for dielectron pairs is evaluated in the Monte-Carlo simulation together with detector response.

## 3. Results and discussions

The efficiency-corrected dielectron invariant mass ($m_{ee}$) spectrum is shown in Figure 1.
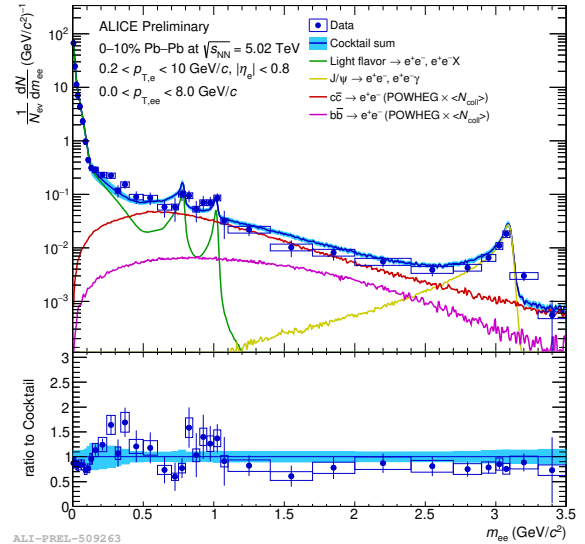


Figure 1. The $m_{ee}$ spectrum in 0–10% central Pb–Pb collisions at $\sqrt{s_{\mathrm{NN}}}$ = 5.02 TeV. The vertical bar shows statistical error, while the box shows the systematic error.

Then, the direct virtual photon signal is extracted from the $m_{ee}$ spectrum with the template fit consisting of 3 components. The fitting function is defined as

$$\frac{dN}{dm_{ee}} = r \times f_{\mathrm{dir}} + (1-r) \times f_{\mathrm{LF}} + f_{\mathrm{HF}},$$

where $f_{LF}$ is the light-flavor cocktail, $f_{HF}$ is the heavy-flavor cocktail and $f_{dir}$ is the direct photon template given by Kroll-Wada formula [5] which describes the relation between real photon production and dielectron production. The r is the only free parameter and is interpreted as direct photon fraction ($\gamma^{direct}/\gamma^{inc}$). In order to avoid the $\pi^0 \to e^+ e^- \gamma$ (Dalitz) decays, The fitting is performed in the mass range of $0.12 < m_{ee} < 0.34$ GeV/$c^2$. Both $f_{dir}$ and $f_{LF}$ are separately normalized to the data at $m_{ee} < 30$ MeV/$c^2$, because a process dependent factor of the $pi^0$ Dalitz decay is close to unity in this mass region. Thus, the functional forms of $f_{dir}$ and $f_{LF}$ are identical. $f_{HF}$ is absolute normalization. An example of the template fit is shown by Figure 2.



ALI-PREL-508295
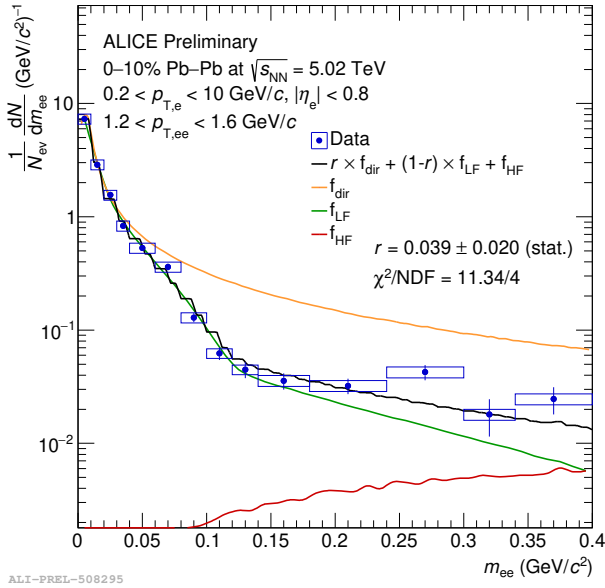
Figure 2. The template fit for direct photon extraction in 0–10% central Pb–Pb collisions at $\sqrt{s_{NN}}$ = 5.02 TeV for $1.2 < p_T < 1.6$ GeV/$c$.

Finally, the direct photon yields are constructed by $\gamma^{dir} = r \times \gamma^{inc}$. The inclusive photon $\gamma^{inc}$ is measured with photon conversion method at the same energy in the same centrality class. Figure 3 shows the $p_T$ spectrum of the direct photon in 0–10% central Pb–Pb collisions at $\sqrt{s_{NN}}$ = 5.02 TeV compared with theoretical models. The dominant systematic uncertainty is due to the fit range variation and the light-flavor cocktail. The new ALICE data points are slightly higher than the pQCD calculation (i.e. photons from hard scatterings at the initial stage). On the other hand, the state-of-the-art model including photons from pre-equilibrium, thermal radiations and hard photons [6] tends to overpredict the direct photon yields at low $p_T$.

## 4. Summary and outlook

The measurement of dielectron production is performed in 0–10 % central Pb–Pb collisions at $\sqrt{s_{NN}}$ = 5.02 TeV recorded in 2018. The virtual photon signal is extracted from the mass range of $0.12 < m_{ee} < 0.34$ GeV/$c^2$. The direct photon yields are higher than the pQCD calculation, which can be interpreted as thermal contributions. On the



ALI-PREL-524092
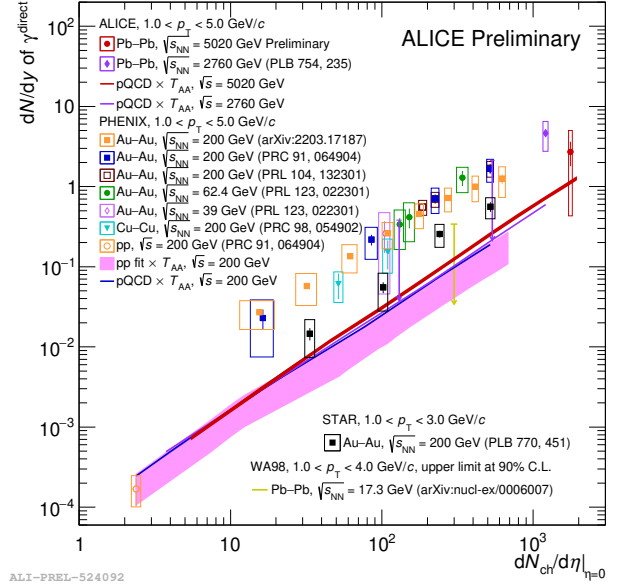
Figure 3. The direct photon spectrum in 0–10 % central Pb–Pb collisions at $\sqrt{s_{NN}}$ = 5.02 TeV compared with theoretical models.

other hand, the state-of-the-art model including photons from pre-equilibrium, thermal radiations and hard photons tends to overpredict the direct photon yields at low $p_T$.

## References

[1] A. Bazavov et al., Phys. Rev. D 85, 054503 (2012)

[2] S. Borsányi et al., Phys. Lett. B 730 (2014) 99-104

[3] J. E. Alam et al., Phys. Rep. 273, 243 (1996)

[4] A. Adare et al. (PHENIX Collaboration), Phys. Rev. C 81, 034911 (2010)

[5] Norman M. Kroll and Walter Wada, Phys. Rev. 98, 1355 (1955)

[6] C.Gale et al., Phys. Rev. C 105, 014909 (2022)

# Direct photon production in inelastic and high-multiplicity proton-proton collisions at $\sqrt{s}$ = 13 TeV via internal conversion technique

H. Murakami and T. Gunji

*Center for Nuclear Study, Graduate School of Science, University of Tokyo*

## 1. Introduction

Dielectron production is a powerful tool to investigate the properties of the quark-gluon plasma (QGP) created in relativistic heavy-ion collisions, as they carry information about the temperature of the medium and its space-time evolution without any distortion due to final-state interactions. Dielectron measurements in pp collisions serve as a reference for heavy-ion studies. Up to date, results of such measurements at the LHC and at RHIC, no significant sign of medium modification has been reported. However, in recent studies, the collective behavior of hadrons has been observed in high-multiplicity pp and p-Pb collisions at the LHC [1,2] and at RHIC similar to previous observations in heavy-ion collisions. If a hot QGP-like medium is created in such small colliding systems, it should give rise to an additional contribution of electromagnetic radiation in the direct photon spectrum. For each real direct photon production mechanism, an associated process producing a virtual photon that converts to a low mass dilepton exists as well. These processes referred to as internal conversions, allow for the measurement of virtual photons with a better signal-to-background ratio compared to real direct photon analysis at low transverse momentum, which is where the thermal radiation signal sits. In the previous measurement [3], virtual photon measurement was performed using 2016 data set and only upper limits are set due to large systematic uncertainties. In this analysis, we measured dielectron spectra and extract direct photon fraction using the full ALICE Run 2 datasets.

## 2. Analysis

Minimum-bias (MB) and high charged particle multiplicity (HM) triggered events are analyzed. Both events triggered requiring simultaneous inputs of V0 detectors made of two arrays of scintillation counters placed on forward and backward of the ALICE interaction point. MB and HM triggers have the same trigger logic, but the latter additionally requires a signal above a threshold that is determined by V0 detectors. Corresponding integrated luminosity are $L_{\text{int,MB}}$ = 30.3 nb$^{-1}$, $L_{\text{int,HM}}$ = 6.08 pb$^{-1}$ respectively. Tracking is performed using ALICE central detector system consists of the Inner tracking system (ITS), the Time Projection Chamber (TPC). Tracks are selected in the kinematic range of $|\eta_e| < 0.8$ and $p_{T,e} > 0.2$ GeV/$c$. Particle identification is based on the energy loss of TPC and Time-of-Flight information of TOF detector. The selected electron pairs are combined into Unlike-sign pairs (ULS). The ULS mass distribution contains correlated signal pairs and combinatorial background which has uncorrelated nature. The background is estimated by constructing a like-sign (LS) pairs

and subtracted from LS pairs considering different acceptance for ULS and LS using the event mixing technique. Then, the spectrum is corrected for the pair reconstruction efficiency using Monte Carlo simulation. Dielectron contributions from known hadron decays are estimated from a MC simulations. Light-flavor hadrons ($\pi^0, \eta, \eta', \rho, \omega, \phi$), $J/\psi$ semileptonic decay of heavy-flavor hadrons are considerd. $\pi^0, \eta, \phi$ and $J/\psi$ spectra measured in pp collisions at $\sqrt{s}$ = 13 TeV are taken as inputs. They are parameterized by a fitting. For $\eta$ meson, instead of direct fitting to the spectrum, a method which makes use of particle ratio $\eta/\pi^0$ was developed and adopted [4]. In this method, $\eta$ is built from the product of $\eta/\pi^0$ and $\pi^0$ which allows us to reduce systematic uncertainty significantly. $\eta', \rho, \omega$ are parameterized using phenomenological scaling law called $m_T$ scaling. $e^+e^-$ from heavy-flavor hadron decays are estimated using PYTHIA6 and normalized to the measured cross section at mid-rapidity. For the HM cocktail, cross sections are scaled by multiplying $p_T$ dependent enhancement factor as $J/\psi$ and heavy-flavor contributions depend on charged particle multiplicity. Figure 1 and 2 show the dielectron invariant mass spectra in MB and HM events. Data and cocktail are consistent with unity and full mass range is under control.
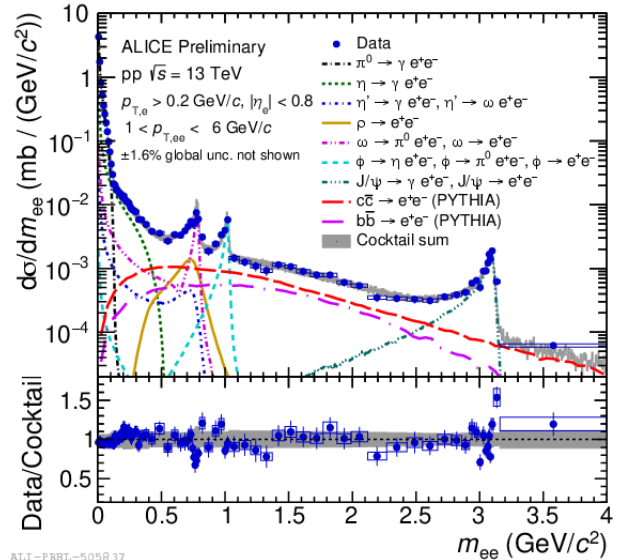


Figure 1. Dielectron invariant mass spectra in MB events.

The fraction of virtual photon is defined as the ratio of direct to inclusive photon, which is the same as for real as well as virtual photon at massless limit

$$r = \frac{\gamma_{\text{dir}}}{\gamma_{\text{incl}}} = \frac{\gamma^*_{\text{dir}}}{\gamma^*_{\text{incl}}}\bigg|_{m=0}. \tag{1}$$

$r$ can be extracted in the kinematic region of $m_{ee} \ll p_{T,ee}$,

27

by a fitting to the $e^+e^-$ invariant mass distribution above $\pi^0$ mass. The function is given by

$$d\sigma/dm_{ee} = r f_{dir}(m_{ee}) + (1-r) f_{LF}(m_{ee}) + f_{HF}(m_{ee}), \quad (2)$$

where $f_{LF}(m_{ee})$ and $f_{HF}(m_{ee})$ are contributions from light-flavor and heavy-flavor decays, $f_{dir}(m_{ee})$ is the shape of direct photon contribution described by Kroll-Wada formula [6]. Here $f_{HF}(m_{ee})$ is fixed to produced open charm and beauty cross sections at mid-rapidity. $f_{LF}(m_{ee})$ and $f_{dir}(m_{ee})$ are normalized independently to the data below 40 MeV/$c^2$ in which Dalitz decay and direct photons where they have same $1/m_{ee}$ dependence. Then, the direct photon fraction $r$ is the only fit parameter, determined by the fitting to the data in the mass interval $0.14 < m_{ee} < 0.32$ GeV/$c^2$ as shown in Fig.2.



Figure 4. Virtual photon fraction as a function of $p_T$ (GeV/$c$) in HM events

## References

[1] CMS collaboration, J. High Energy Phys. 09 (2010) 091.
[2] CMS collaboration, Phys. Lett. B718 (2013) 795.
[3] ALICE collaboration, Phys. Lett. B 788 (2019) 505.
[4] ALICE collaboration, Phys. Rev. Lett. 127 (2021) 042302.
[5] ALICE collaboration, J. High Energy Phys. 09 (2010) 091.
[6] N.M. Kroll and W. Wada PR 98 (1955) 1355.
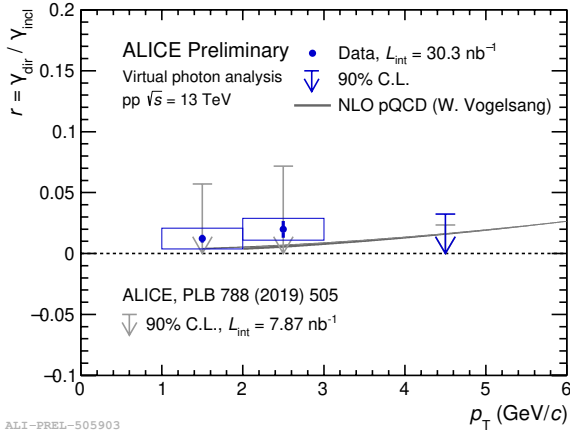
Figure 2. Extraction of virtual photon fraction $r$ in MB events.
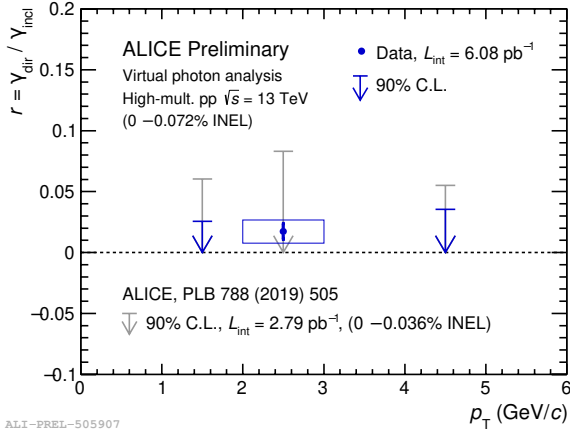


Figure 3. Virtual photon fraction as a function of $p_T$ (GeV/$c$) in MB events

## 3. Results and summary

Extracted $r$ as a function of $p_T$ are shown together with previous study (Fig.3 and Fig.4). Systematic uncertainty is significantly reduced and allows us to extract virtual photon fraction. Results compatible with pQCD calculation and no significant direct photon fraction in MB. No sign of an increase direct photon fraction in HM was found.

# Measurement of long-range two-particle correlation and pseudorapidity dependence of $v_2$ with ALICE

Y. Sekiguchi for the ALICE Collaboration

*Center for Nuclear Study, Graduate School of Science, the University of Tokyo*

## 1. Introduction

The long-range correlations in the rapidity space, called "ridge", were first observed in Au–Au collisions at $\sqrt{s_{NN}}$= 200 GeV at RHIC  [1, 2].  The long-range correlations are well understood as derived from the collective expansion of the initial collision geometry and its fluctuations in heavy-ion collisions.  Similar long-range correlations have been observed in high-multiplicity pp and p–Pb collisions at the LHC [3]. The measurements of ridge structure with large rapidity gap and different collision systems are important for quantifying the final-state interactions. We present results on long-range two-particle correlations with pseudorapidity gap $|\Delta\eta| \sim 8$, which is an unprecedented $\Delta\eta$ range at the LHC, and extracted the second-order azimuthal anisotropy as a function of pseudorapidity ($v_2(\blacksquare)$) at $-3.1 < \eta < 4.8$ in pp collisions at $\sqrt{s}$=13 TeV, and p–Pb and Pb–Pb collisions at $\sqrt{s_{NN}}$=5.02 TeV.

## 2. Experimental setup

The main sub-detectors in this analysis are the Time Projection Chamber (TPC) and the Forward Multiplicity Detector (FMD). The TPC is used for charged particle tracking.  It covers a pseudorapidity of $|\eta| < 0.8$, where a $2\pi$ coverage in azimuthal angle is ensured. The FMD is located at $-3.4 < \eta < -1.7$ (FMD3) and $1.7 < \eta < 5.1$ (FMD1,2) with $2\pi$ acceptance in azimuthal angle. The FMD is not a tracking detector. However, it can measure the multiplicities with a granularity of $\Delta\varphi = 1/20\pi$ and $\Delta\eta = 0.05$. For event trigger and centrality determination, the V0 detectors, which are located at $-3.7 < \eta < -1.7$ (V0C) and $2.8 < \eta < 5.1$ (V0A), are used.  Minimum-bias events are triggered by using a coincidence signal between V0A and V0C. The high-multiplicity trigger based on the sum of V0A and V0C multiplicity is used for the pp analysis. The positive pseudorapidity is in the Pb-going direction in p–Pb collisions.

## 3. Analysis

The two-particle correlations between trigger and associated particles are measured as a function of the pseudorapidity difference $\Delta\eta$ and the azimuthal angle difference $\Delta\varphi$ for a given event. The TPC can measure the track of charged particles one by one, however, the FMD is not a tracking detector and the multiplicity measured in each FMD segment is treated as the number of tracks in the average $\varphi$ and $\eta$ of each segment. The correlation function as a function of $\Delta\eta$ and $\Delta\varphi$ between two charged particles is defined as

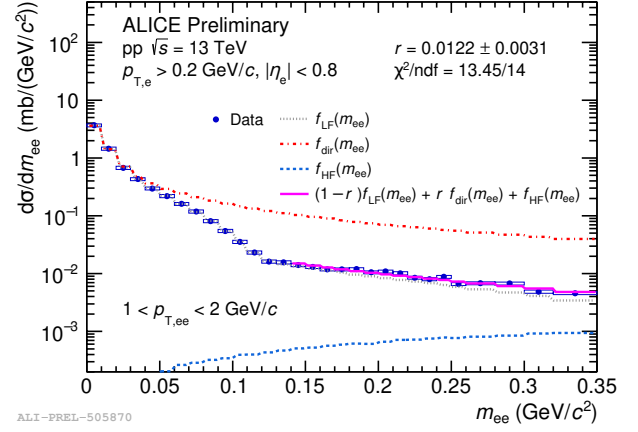$$\frac{1}{N_{\text{trig}}}\frac{\mathrm{d}^2 N_{\text{asso}}}{\mathrm{d}\Delta\blacksquare\mathrm{d}\Delta'} = \frac{S(\Delta\eta, \Delta\varphi)}{B(\Delta\eta, \Delta\varphi)}, \qquad (1)$$

where $N_{\text{trig}}$ is the total number of triggered particles in the event class, the signal distribution $S(\Delta\eta, \Delta\varphi) = \frac{1}{N_{\text{trig}}}\frac{\mathrm{d}^2 N_{\text{same}}}{\mathrm{d}\Delta\blacksquare\mathrm{d}\Delta'}$ is the associated yield per trigger particle in the same event, and the background function $B(\Delta\eta, \Delta\varphi) = \alpha\frac{\mathrm{d}^2 N_{\text{mixed}}}{\mathrm{d}\Delta\blacksquare\mathrm{d}\Delta'}$ is the pair yield between trigger in one event and associated particles from other events with the same multiplicity and primary-vertex position along the beam direction. The $\alpha$ factor is chosen so that $B(\Delta\eta, \Delta\varphi)$ is unity at the maximum bin. By dividing $S(\Delta\eta, \Delta\varphi)$ by $B(\Delta\eta, \Delta\varphi)$, pair acceptance and pair efficiency are corrected. Figure 1 shows the associated yield per unidentified hadron trigger particles for TPC-FMD1,2 (left) and TPC-FMD3 (center) with $0.2 < p_T^{trig} < 3$ GeV/$c$ and FMD1,2–FMD3 correlations (right) in pp, p–Pb, and Pb–Pb collisions with the similar multiplicity class ($\langle N_{ch,|\eta|<0.8}\rangle \sim 43$ in Pb–Pb, $\langle N_{ch,|\eta|<0.8}\rangle \sim 47$ in p–Pb, and $\langle N_{ch,|\eta|<0.8}\rangle \sim 33$ in pp), where these multiplicities correspond to top 20% p–Pb and top 0.1 % pp collisions, respectively.  The long-range correlations in the near-side ($-\pi/2 < \Delta\varphi < \pi/2$) can be observed up to $\Delta\eta \sim 8(6)$ in all three collisions.



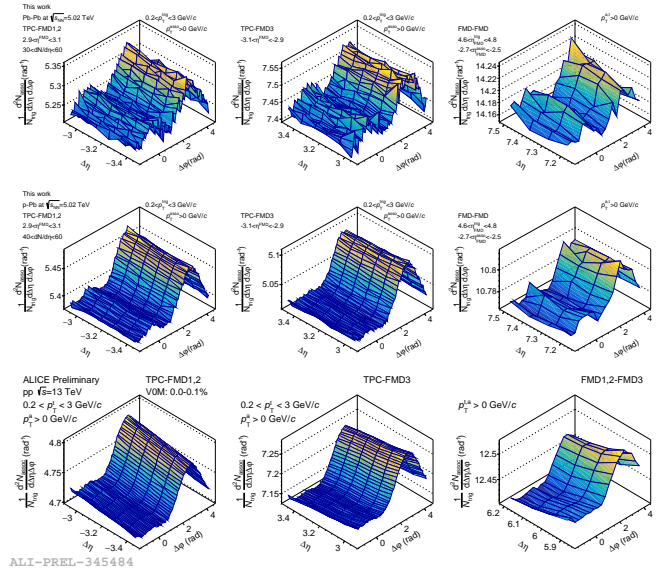Figure 1.  Correlation functions between TPC-FMD1,2 (left), TPC-FMD3 (center), and FMD1,2-FMD3 (right) in pp (top), p–Pb (middle), and Pb–Pb (bottom) collisions with similar multiplicity, respectively.

The template fitting procedure [4] is applied to reduce the non-flow contamination due to jets and resonance decay. The correlation function is assumed to be a superposition of scaled distributions in low multiplicity events and flow
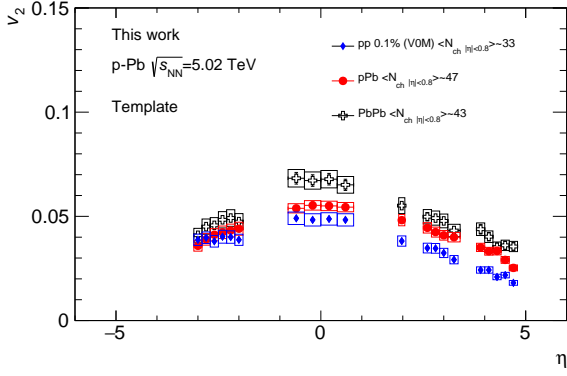
Figure 2. $v_2(\eta)$ in pp, p–Pb, Pb–Pb collisions with similar multiplicity
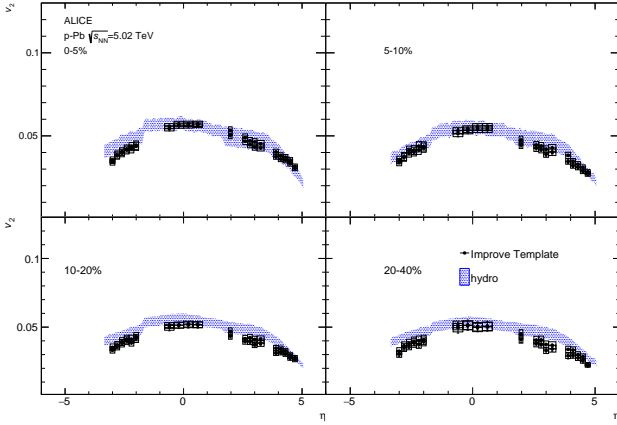


Figure 3. $v_2(\eta)$ compared to the hydro calculation in p–Pb collisions

components as below.

$$Y_{\text{high}}(\Delta\varphi) = FY_{\text{low}}(\Delta\varphi) + G\{1 + 2\sum_{n=2}^{3} V_n \cos(n\Delta\varphi)\} \quad (2)$$

$Y_{\text{high}}(\Delta\varphi)$ and $Y_{\text{low}}(\Delta\varphi)$ are the correlation functions in high and low multiplicity events, respectively. $F, G, V_n$ are free parameters. $V_2$ is the product of $v_2(\eta_1)$ and $v_2(\eta_2)$. The azimuthal anisotropy, $v_2$, at a certain acceptance is obtained by three relative modulations as

$$v_2(\eta^A) = \sqrt{\frac{V_2(\eta^A, \eta^B)V_2(\eta^A, \eta^C)}{V_2(\eta^B, \eta^C)}}, \quad (3)$$

where (A,B,C)=(FMD1,2,TPC, FMD3). Since the measured $p_T$ region is different between TPC and FMD, it is necessary to extrapolate $v_2$ of the TPC region to $p_T \sim 0$ in order to compare $v_2$ in the entire rapidity region. The extrapolation factor is extracted by using $p_T$ spectrum and $p_T$ differential $v_2$.

$$\kappa = \frac{\int_0 v_2 \frac{dN}{dp_T} dp_T}{\int_0 \frac{dN}{dp_T} dp_T} \Big/ \frac{\int_{0.2} v_2 \frac{dN}{dp_T} dp_T}{\int_{0.2} \frac{dN}{dp_T} dp_T} \quad (4)$$

The integrated $v_2$ is obtained as $v_2^{p_T > 0\text{GeV}/c} = \kappa v_2^{p_T > 0.2\text{GeV}/c}$. Figure 2 shows the extracted $v_2(\eta)$ in

pp, p–Pb, and Pb–Pb collisions after the $p_T$ extrapolation. Non-zero $v_2$ is observed at -3.1< $\eta$ <4.8 in all collision systems. The $v_2$ in Pb–Pb is larger than p–Pb with similar multiplicity. It suggests that the initial effect such as initial momentum anisotropy dominates in small systems, however, the effect due to geometry makes more large anisotropy in Pb–Pb collisions than p–Pb collisions. Figure 3 shows $v_2(\eta)$ compared to the hydro model calculation based on MUSIC, 3D Glauber initial conditions, and URQMD to simulate the dynamics in hadronic phase in four different centrality classes [5]. The hydro model describes data very well for all centrality classes over the entire pseudorapidity region. It suggests that collectivity exists at forward rapidity even in small systems and it can be interpreted by the hydro model as well as heavy-ion collisions.

## 4. Summary

The long-range two-particle correlations are measured by using TPC and FMD in pp, p–Pb, and Pb–Pb collisions with similar multiplicity. The long-range correlations are observed up to $\Delta\eta \sim 8(6)$ in all collision systems. The pseudorapidity dependence of $v_2$ is extracted by using the three-sub event method. We also compared the data to the hydro model calculation in p–Pb collisions. The hydro model describes the data very well over the entire rapidity region. It indicates that the collectivity exists over a wide rapidity region and it can be interpreted by the hydro model as well as heavy-ion collisions.

## References

[1] STAR Collaboration, Phys. Rev. C80 064912 (2009).
[2] PHOBOS Collaboration, Phys. Rev. Lett. 104 062301 (2010).
[3] CMS Collaboration, JHEP 09 091 (2010).
[4] ATLAS Collaboration, Phys. Rev. Lett. 116, 172301 (2016).
[5] W. Zhao et al. arXiv:2203.06094 (2022)

# Space-charge distortion correction for the ALICE-TPC using machine learning methods

## H. Baba, D. Sekihata and T. Gunji

*Center for Nuclear Study, Graduate School of Science, University of Tokyo*

## 1. Introduction

A Large Ion Collider Experiment (ALICE) [1] is an experiment at the Large Hadron Collider (LHC) dedicated to the study of high-energy heavy-ion physics. It aims to uncover the physical properties of strongly interacting matter known as the quark-gluon plasma (QGP) at the highest energy density that could be reached with currently existing accelerators. All matter in our universe is thought to have been in the QGP state at $10^{-6} \sim 10^{-5}$ seconds after the Big Bang.

The Time Projection Chamber (TPC) in ALICE [2] is a gaseous tracking detector designed to detect charged particles with mid-rapidity. There, the trajectories of charged particles are reconstructed and particle identification is carried out. The momentum of charged particles is measured by the curvature of the trajectories in the solenoid magnet at 0.5 T, and particle identification is performed by combining this information with each particle's energy loss in the gas. A 400 V/cm electric field with very high homogeneity is achieved inside the drift volume of TPC by the fine-segmented field cage on the inner and outer wall and a high voltage of -100 kV applied to the central electrode.

The readout chamber at the end cap ($z = \pm 250$ cm) is divided into 18 sectors in azimuthal angle $\varphi$. Installed in each sector are the inner and outer readout chambers, respectively called IROC and OROC. The active areas for the readout chambers are between 85 and 132 cm for the IROC, and 135 and 247 cm for the OROC in radial direction. They consisted of Multi-Wire Proportional Chambers (MWPC) with gating grids during LHC Run 1 (2009-2013) and 2 (2015-2018) before the ALICE TPC upgrade.

In Runs 3 (started in 2022) and 4 (planned in 2030), LHC experiments will take data in Pb–Pb collisions at a maximum of $\sqrt{s_{NN}} = 5.5$ TeV and a collision rate of 50 kHz. In order to accumulate the unprecedented amount of statistics, upgrade of the TPC [3] has been carried out during the LHC Long Shutdown 2 (LS2).

One significant issue that needs to be overcome in order to make the TPC detector function is the space-charge effect. Positive ions produced in the electron multiplication process at the readout chambers are known to flow back into the TPC field cage, becoming a major source of distortion to the homogeneity of the electric field (space-charge effect). During Runs 1 and 2 the gating grid prevented these positive ions from entering the TPC field cage, but this architecture could only handle collision rates of up to 3 kHz, which is significantly below the expected 50 kHz collision rate during the LHC Run 3. As part of the TPC upgrade, the MWPC and gating grid in the readout chambers were removed and were replaced with stacks of four Gas Electron Multiplier (GEM) foils in order to address this problem.

The four GEM foils are relatively effective on their own in keeping the space-charge effect to a tolerable level, but a mechanism to correct the distortions created by the space-charge is still necessary. If the gain of the GEMs is 2000 and the proportion of backflowing positive ions (Ion Backflow, IBF) is 1%, 20 ions per one single primary electron are expected to go back to the drift volume. With the positive ion drift time of 160 ms and the collision rate of 50kHz, space-charge from 8,000 collision events are expected to pile up inside the TPC field cage, resulting in an electron track distortion of $\mathcal{O}(10cm)$ (see figures 1 and 2). The strategies used to implement this calibration are discussed in the following sections.
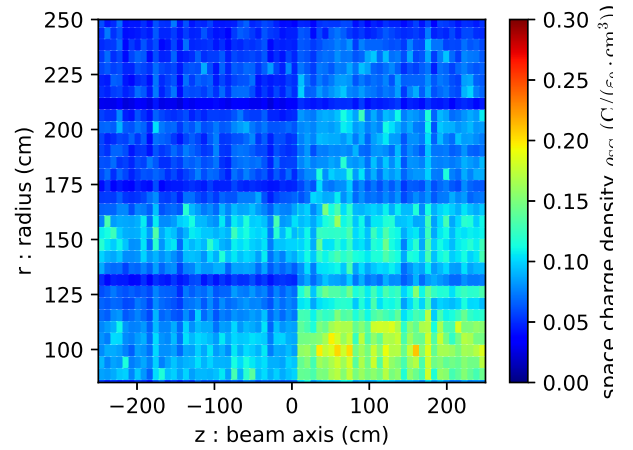


Figure 1. The simulated space-charge density $\rho_{SC}$ at 50 kHz of Pb-Pb collisions in r-z plane. The striped pattern in z originating from the fluctuation of the charged-particle multiplicity corresponds to timing structure of collisions.

## 2. Calibration strategy

The space-charge distortion calibration will be performed in two steps: online synchronous calibration and offline asynchronous calibration.

The online synchronous calibration will be performed with the goal of reducing the distortion to an amount that would allow for the cluster to track association ($\mathcal{O}(mm)$). To accomplish this the TPC clusters are corrected by a 3D correction map obtained by tracklets from the Inner Tracking System (ITS), Transition Radiation Detector (TRD) and Time-Of-Flight detector (TOF) as a reference for the true track position. The map is updated to the current average charged particles density in the time interval of $\mathcal{O}(\min)$ scaled by the digital currents from the readout chambers integrated over the drifting time of ions.

The offline asynchronous calibration will be performed with the goal of reducing the space-charge density fluctua-
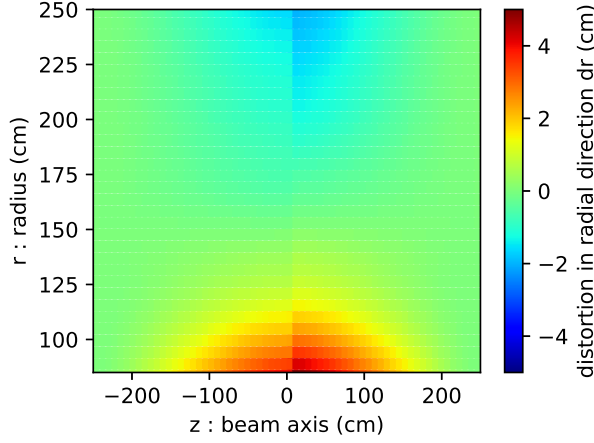
Figure 2. The expected electron track distortion in radial direction $dr$ at 50 kHz of Pb-Pb collisions in r-z plane obtained by solving the Poisson and Langevin equations. It can be seen that the electrons are diverted towards larger radii at inner points and vice versa. Distortions reach a maximum of 20 cm.

tions to the intrinsic resolution of TPC ($\mathcal{O}(200\mu m)$). The short-time distortion fluctuations must be addressed in order to accomplish this level of precision. This would require that the distortion correction be applied for about every 5 ms, where it is impossible to collect enough statistics for other methods such as the ITS-TRD-TOF extrapolation method to yield a prediction with adequate precision. Therefore, an alternative approach which would allow a relatively fast, efficient distortion prediction is desired.

## 3. Machine learning approach

As one possibly effective solution to the tasks discussed above, the authors have been studying ways to implement a machine learning approach. The machine learning scheme currently under discussion is as follows: First, input data from the TPC is integrated over some time and stored in the appropriate servers as the Integrated Digital Current (IDC). Then the IDCs are integrated over $r$ and $\varphi$ (1D IDC), and the 1D IDC, together with its Fourier coefficients with respect to time are fed to the machine learning as input data to predict the amount of distortion at each TPC space point (1D→3D correction). Some discussion on data preprocessing before the 1D→3D correction and additional 3D→3D correction after the 1D→3D correction are also in progress, but neither are in the implementation stage at the moment.

A boosted decision tree, random forest and dense neural network has so far been implemented for the 1D→3D correction. The distortion fluctuations for 400 maps were predicted, and figure 3 shows the mean and standard deviation of the difference between the predictions of the neural network and the expected distortion values. The mean is within 100 $\mu$m and standard deviation is within 300 $\mu$m, which suggest that the necessary precision of $\mathcal{O}(200\mu m)$ might eventually be reached by further tuning some of the training parameters. More research is needed in this direction.
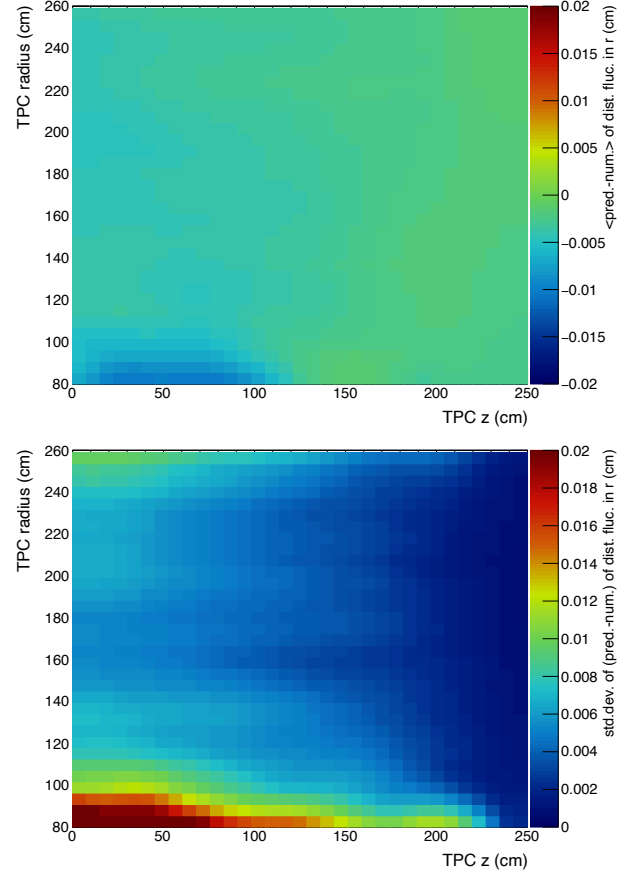


Figure 3. Difference between the distortion predicted by the neural network and the simulation results in radial direction $dr$ at 50 kHz of Pb-Pb collisions in r-z plane. The network was trained with 2,000 maps and 1,000 points per map. Mean and standard deviation over 400 maps.

## 4. Summary and outlook

Machine learning techniques so far seem to be a relatively promising solution to the ALICE-TPC space-charge distortion calibration. More in-depth study on training methods and machine learning model selection is necessary for optimal performance.

## References

[1] B. Abelev et al. (The ALICE Collaboration), Int. J. Mod. Phys. A 29 (2014) 1430044
[2] The ALICE Collaboration, CERN-LHCC-2000-001
[3] The ALICE Collaboration, CERN-LHCC-2013-020

# Accelerator and Instrumentation

# High-resolution spectroscopy at OEDO-SHARAQ — Demonstration of ion optics —

S. Michimasa, S. Hanai, T. Chillery, M. Dozono[a], J.W. Hwang[b], S. Ota[c], N. Imai, K. Yako, and S. Shimoura

*Center for Nuclear Study, Graduate School of Science, University of Tokyo*
[a] *Department of Physics, Kyoto University*
[b] *Center for Exotic Nuclear Science, Institute of Based Science, Korea*
[c] *RCNP, Osaka University*

The Optimized Energy Degrading Optics for radioactive ion beams (OEDO) system [1] was constructed in 2017, and successfully provides low-energy RI beams obtained by the OEDO slow-down scheme from $\sim 200$ MeV/u down to 15–50 MeV/u. The starting point of the OEDO system was an upgrade of the High-Resolution Beamline (HRB) [2] and the Spectroscopy with High-resolution Analyzer of RadioActive Quantum beams (SHARAQ) spectrometer [3] for opening up new possibilities in nuclear experimental studies with low-energy RI beams.

The original OEDO magnet arrangement was not suitable for high-resolution RI spectroscopy at 100–300 MeV/u although it is still attractive performance of the SHARAQ spectrometer. We reported a consideration about the minimum magnet rearrangement in the CNS annual report 2018 [4] in order to realize the high-resolution RI spectroscopy at the OEDO+SHARAQ scheme. Based on the result, we have done a rearrangement in 2021. This report describes a demonstration of ion optics for high-resolution studies at OEDO-SHARAQ.

The rearrangement of magnets was schematically indicated in Fig. 1, where the boxes with "STQ," "D," and without labeling indicate a Superconducting Triplet Quadrupole magnet, a Dipole magnet and a normal-conducting quadrupole magnet, respectively. The "E15"
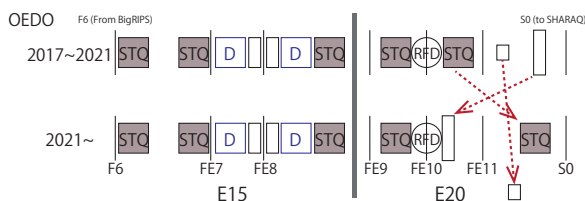


Figure 1. Magnet rearrangements for the high-resolution spectroscopic studies at OEDO-SHARAQ. Details are written in the text.

and "E20" are the names of the experiemental rooms, and the focus names of the OEDO beamline (F6, FE7, $\cdots$, and S0) are also shown. The upper is the original configuration from the OEDO construction, and the lower is the present arrangement. The three magnets between FE10 and S0 were moved: two of the three were relocated and the other became off the beamline. After the rearrangement, we have performed 2 irradiation measurements by using ion optics for high-resolution spectroscopy; a demonstration of the dispersion-matching (DM) beam transport at the new OEDO configuration; and the tri-neutron search via the

$^3$H($t$,$^3$He)$^3n$ reaction, which is reported in this annual report [5].

The DM transport at OEDO-SHARAQ was examined by using 82-MeV/u triton beam. The ion-optical design is shown in Fig. 2 to show clearly ion-optical features at the beamline foci, which were slightly improved from the consideration discussed in Ref. [4]. The beam parameters at F3
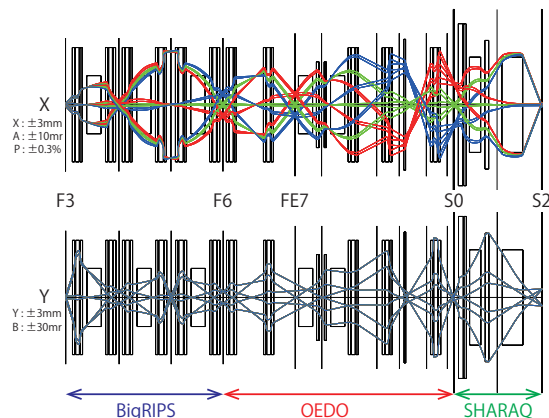


Figure 2. Ion-optical trajectories of the DM mode in BigRIPS-OEDO-SHARAQ scheme.

is assumed to be 3 mm of horizontal spot size (X), 10 mr of horizontal outgoing angle (A), 3 mm of vertical spot size (Y), 30 mr of vertical outgoing angle (B), and 0.3% of momentum spread (P). The setting of SHARAQ spectrometer is similar to the previous setting for the SHARAQ03 experiment [6]. The S0 and S2 are the secondary target position and the final focal plane of the SHARAQ spectrometer, respectively.

The beam tuning was done by a similar procedure for the original DM transport at HRB-SHARAQ, which was buildup of focusing conditions from upstream at each ion-optical focus. Figure 3 shows the present result indicating how lateral and angular dispersion matching conditions. Figure 3(a) is a correlation plot between horizontal positions at S0 and S2. When the lateral dispersion matching condition is fulfilled from F3 to S2, the S2 position should be located at the center without depending on the S0 position. Figure 3(a) fits truly into such a situation. Figure 3(b) is a correlation plot between horizontal position at S0 and the horizontal angle at S2. Because a vertically straight locus was seen at $x_{S0}$ in this plot, this indicates satisfying the condition of angular dispersion matching through the
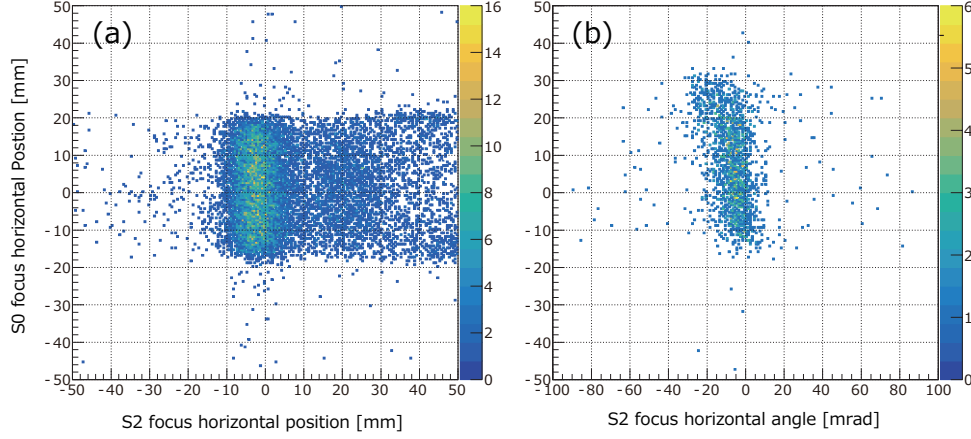
Figure 3. Ion-optical trajectories of the DM mode in BigRIPS-OEDO-SHARAQ scheme.

BigRIPS-OEDO-SHARAQ complex. Consequently, these figures indicate that both dispersion matching conditions were successfully satisfied in the rearranged configuration.

In order to perform a spectroscopy of the $(t,{}^3\mathrm{He})$ reaction, we applied an achromatic transport to S0 at 170-MeV/u triton beam successfully. The ion optical trajectory for the experiment was designed based on the high-resolution achromatic mode at HRB [2]. By this tuning procedure for the experiment, we demonstrated that the new magnet arrangement can provide achromatic RI beams. The details on the experiment appears in Ref. [5]

In the first half period of the fiscal year 2022, a TOF-B$\rho$ mass measurement was scheduled at OEDO-SHARAQ. For smooth performance of the planned experiments at OEDO-SHARAQ, the efficiency of the configuration switch between high-energy and energy-degraded modes of OEDO-SHARAQ is getting to be essential. To reduce or resolve a time consuming issue of the beamline configuration change, we recently started to consider OEDO transport mode by using the new configuration. The detailed discussion on this topic will be reported in Ref. [7].

However, for high-energy spectroscopy, a problematic limitation of the magnetic rigidity of OEDO-DM mode is still remaining, as discussed in Ref. [4]. The resolution of this limitation is essential for providing more neutron-rich RI beams toward the neutron dripline. Concretely, the first normal-conducting quadrupole magnet downstream from RFD should be strengthened roughly twice. We are aiming at a budget to perform more challenging experiments that accelerate the progress of nuclear physics.

## References

[1] S. Michimasa *et al.*, Prog. Theor. Exp. Phys. **2019**, 043D01 (2019).

[2] T. Kawabata *et al.*, Nucl. Istrum. Meth. Phys. Res., Sect. B **266**, 4201 (2008).

[3] T. Uesaka *et al.*, Prog. Theor. Exp. Phys. **2012**, 03C007 (2012).

[4] S. Michimasa *et al.*, CNS annual report 2018, CNS-REP-98, 35 (2020).

[5] K. Miki *et al.*, the CNS annual report 2021, (2022).

[6] S. Michimasa *et al.*, Phys. Rev. Lett. **121**, 022506 (2018).

[7] T. Chillery *et al.*, the CNS annual report 2021, (2022).

# Improved Optics for the OEDO Low Energy Mode
# Used in the $^{130}$Sn Experiment

T. Chillery, S. Michimasa, J.W. Hwang[a], N. Imai, S. Ota, S. Shimoura, K. Yako

*Center for Nuclear Study, Graduate School of Science, University of Tokyo, Wako, Saitama 351-0198, Japan*
*[a] Center for Exotic Nuclear Studies, Institute for Basic Science (IBS), Daejeon 34126, Rep. of Korea*

Construction of the OEDO (Optimized Energy Degrading Optics) system [1] was completed in 2017. The principle aim of OEDO is to provide medium-heavy energy-degraded radioactive ion (RI) beams for both nuclear physics and nuclear astrophysics studies. The system is designed to slow down beams provided by the BigRIPS SRC from $\sim 200$ MeV/u to $15 - 50$ MeV/u, thereby accessing a mass-energy region previously inaccessible by current RI beam facilities. Experiments performed at OEDO can also incorporate the high-resolution SHARAQ spectrometer located downstream of OEDO. Details of SHARAQ may be found in reference [2]. The OEDO system was commissioned in the day0 campaign by studying transfer reactions on $^{77}$Se, $^{93}$Zr, and $^{107}$Pd. During this, it was discovered the small bore radius of the quadrupole magnet QE19 significantly reduced the F3 - S0 transmission from 55% at FE9 to 18% at S0 [1], where S0 is the original secondary target position of OEDO.

Within the fiscal year 2021, two changes were made in a push to improve the transmission of the BigRIPS-OEDO beamline down to S0. The first was an improvement of the calculated F3 - FE9 trajectory, and the second was a reconfiguration of the FE10 - FE12 section of the OEDO beamline during spring 2021, with complimentary calculations performed to optimize the beam trajectory for the new condition. This report covers the work in fiscal year 2021 to prepare the beam transport optics for the low-energy mode of the OEDO-SHARAQ beamline, required for the $^{130}$Sn experiment scheduled in April 2022. In the following, the S0+ focal plane represents the secondary target position in the TINA silicon-detector array [3], planned for use in the $^{130}$Sn experiment.

The ion-optical transport code COSY-Infinity[1] (v9.0) was used to simulate beam transport through F3 - S0+. During preparation of the F3 - FE9 magnet parameters for the $^{130}$Sn experiment a new solution was found for the ion-optical transport. In the previous solution presented in reference [1], the conditions $(Y|Y)_{39} \sim 0$ and $(Y|B)_{39} = -0.45$ mm/mrad were applied. Following further tuning the new solution finds transmission may be improved with the condition $(Y|B)_{39} \sim 0$. Figure 1 shows the updated trajectories in the X and Y planes. Compared to the previous solution, the $\delta_p = \pm 2\%$ trajectories are now completely constrained within FE8 - FE9. Table 1 presents the matrix elements for F3 - FE9. As a compromise for meeting the $(Y|B)_{39} \sim 0$ condition, the Y-magnification is undesirably enhanced to $(Y|Y)_{39} \sim 5.33$. However given the typical beam size at F3 has Y width 6 mm, the calculated width at

[1] https://www.bmtdynamics.org/index_cosy.htm



Figure 1. COSY-calculated $1^{st}$ order beam trajectories in the X and Y planes between F3 - FE9 for low energy tuning at SHARAQ. This is the goal for the spring 2022 $^{130}$Sn experiment.

FE9 of 32 mm is acceptable for OEDO.

To improve the FE9 - S0+ transmission the FE10 - FE12 section of the OEDO beamline was reconfigured in the spring of 2021. Figure 2 shows a sketch of the original and new OEDO beamline configurations. In the new configuration the STQ18 and QE20 magnet positions are effectively swapped, and the QE19 magnet removed from the beamline entirely. This reconfiguration was similarly proposed in previous CNS annual reports [4,5].

Figure 3 shows the calculated trajectories between FE9 - S0+. The beam parameters (in 1 sigma) at FE9 are assumed to be $x = 30$mm, $a = 20$mrad, $y = 15$mm, $b = 10$mrad, and $\delta_p = 2\%$. The calculated trajectory for $^{77}$Se using the previous OEDO configuration is available in reference [1] figure 14b. Comparing with the new trajectory it is clear the re-

Table 1. COSY matrix elements of F3 - FE9. The reference particle is $^{130}$Sn at 170.4 MeV/u. x and y in mm, a and b in mrad, and $\delta_p$ is momentum dispersion in %.

|          | $\|x)$ | $\|a)$ | $\|y)$ | $\|b)$ | $\|\delta_p)$ |
|----------|--------|--------|--------|--------|---------------|
| $(x\|$   | +1.01  | -0.01  | +0.00  | +0.00  | +22.04        |
| $(a\|$   | +1.55  | +0.97  | +0.00  | +0.00  | +3.84         |
| $(y\|$   | +0.00  | +0.00  | -5.33  | +0.04  | +0.00         |
| $(b\|$   | +0.00  | +0.00  | -1.14  | -0.18  | +0.00         |
| $(\delta_p\|$ | +0.00 | +0.00 | +0.00 | +0.00  | +1.00         |

Figure 2. OEDO beamline configurations for a) original and b) new magnet configurations. Distances given in meters. In the new configuration the STQ18 and QE20 positions are effectively swapped, and the QE19 magnet has been removed entirely.

Table 2. COSY matrix elements of FE9 - S0+ for new OEDO configuration. The reference particle is $^{130}$Sn at 22.9 MeV/u. x and y in mm, a and b in mrad, and $\delta_p$ is momentum dispersion in %.

|        | $|x)$ | $|a)$ | $|y)$ | $|b)$ | $|\delta_p)$ |
|--------|-------|-------|-------|-------|-------|
| $(x|$  | -1.00 | +0.00 | +0.00 | +0.00 | +0.00 |
| $(a|$  | +0.46 | -1.00 | +0.00 | +0.00 | +0.00 |
| $(y|$  | +0.00 | +0.00 | -1.07 | +0.00 | +0.00 |
| $(b|$  | +0.00 | +0.00 | +0.40 | -0.94 | +0.00 |
| $(\delta_p|$ | +0.00 | +0.00 | +0.00 | +0.00 | +1.00 |

moval of the QE19 magnet should improve the FE9 - S0+ transmission. In addition, the placement of QE20 between STQ17 and 18 allows for fine tuning of the parallel beam condition, which was not possible in the previous configuration.

The most important quantities for focusing a beam along the desired point-parallel-point trajectory are (X|X) = (A|A) = (Y|Y) = (B|B) = -1. In the previous optics the matrix elements were (X|X) = -1.03, (A|A) = -0.97, (Y|Y) = -0.72, and (B|B) = -1.38. The matrix elements of FE9 - S0+ for the new trajectory, provided in table 2, closely meet the point-parallel-point conditions and show an improvement over the previous optics.

The new COSY matrix elements were input to Monte Carlo simulation code "beamsimu", originally developed by J. W. Hwang. The simulation included beamline materials, the opening of the beam pipes, and the OEDO RF Deflector (RFD). The RFD was tuned to reduce the beam spot size at S0+, where optimal parameters HV = 340kV, $\phi = 90^o$ achieved S0+ focus X (Y) = ± 8 (17) mm, within the target radius of 25 mm. From the same simulation, the F3 - S0+ transmission for $^{130}$Sn beam energy 20 ± 2 MeV/u was estimated to be 77% (46%) considering up to 1$^{st}$ (3$^{rd}$) order aberrations. Therefore the transmission is expected to increase by a factor 2 - 4 compared to the previous experiment [1], which had a measured F3 - S0 transmission of 18%. The corresponding beam rate at S0+ is 179 kpps (107 kpps) considering 1$^{st}$ (3$^{rd}$) order aberrations, where the
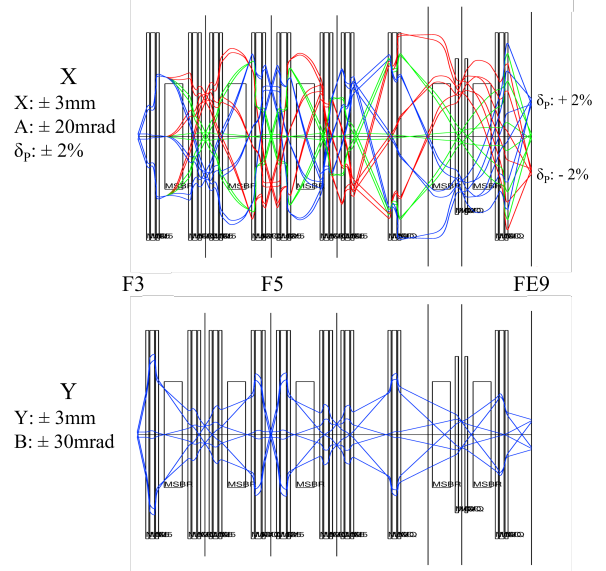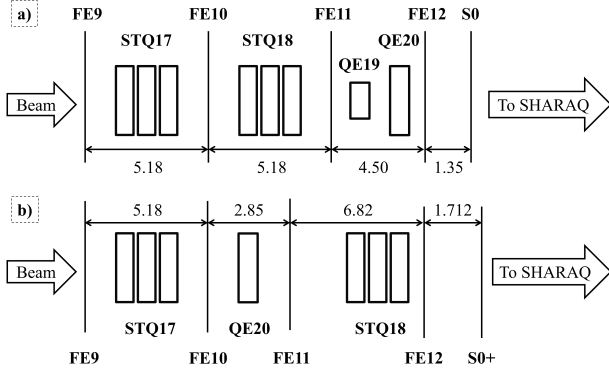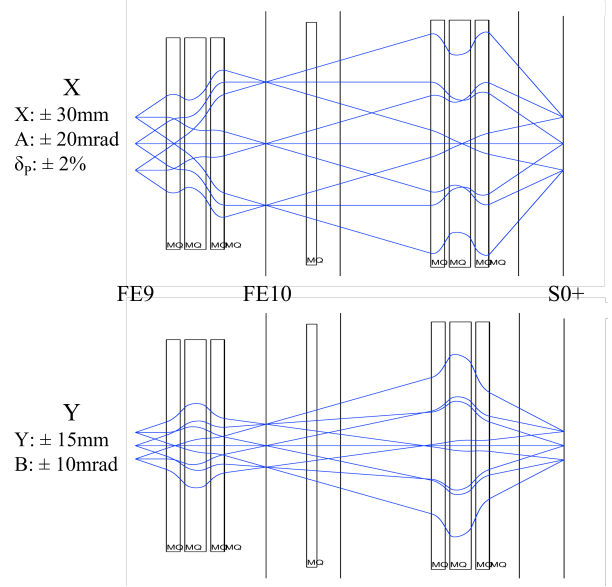


Figure 3. COSY-calculated 1$^{st}$ order beam trajectories in the X and Y planes between FE9 - S0+ for low energy tuning at SHARAQ. This is the goal for the spring 2022 $^{130}$Sn experiment.

rate at F3 was calculated using a LISECute[2] (v16.0.3) simulation.

The ion-optical transport through BigRIPS-OEDO has seen two improvements. The first is an updated trajectory through F3 - FE9 after tuning the matrix elements such that $(Y|B)_{39} \sim 0$. The second follows the magnet reconfiguration between FE10 - FE12 with a new ion-optical solution to meet the required point-parallel-point trajectory of OEDO's low-energy mode. The transmission is expected to increase up to fourfold compared to the OEDO day0 campaign. Ion-optical parameters are now ready for the $^{130}$Sn(d,p) experiment, the machine time of which is planned for April 2022.

**References**

[1] S. Michimasa *et al.* PTEP **043D01** (2019).
[2] S. Michimasa *et al.* NIM B **317** 305-310 (2013).
[3] P. Schrock *et al.* RIKEN Accel. Prog. Rep. **51** 20 (2018).
[4] S. Michimasa *et al.* CNS Annual Report 2018 **CNS-REP-98** 35-36 (2020).
[5] T. Chillery *et al.* CNS Annual Report 2020 **CNS-REP-100** 33-34 (2022).

---

[2]https://lise.nscl.msu.edu/lise.html

# Simulation studies of SR-PPAC

S. Hanai, S. Ota, R. Kojima, M. Dozono, N. Imai, S. Michimasa, S. Shimoura, J. Zenihiro[a],
K. Inaba[a], Y. Hijikata[a]

*Center for Nuclear Study, Graduate School of Science, The University of Tokyo*
*[a]Department of Physics, Kyoto University*

Parallel Plate Avalanche Counters (PPACs) have proven highly effective in measuring the tracking parameters of heavy ion beams [1]. In particular, Strip Readout PPAC (SR-PPAC) detectors have a high-speed response for heavy-ion beams owing to correcting the mirror charge of electrons drifting between narrow electrodes without delayline [2,3]. The charge information is obtained by using the Time over Threshold (ToT) method. The ToT method converts the pulse height of the signal to pulse duration over a preset threshold voltage. It has a distinct advantage in taking charge or pulse height information faster than the method of integrating pulses with a Flash ADC. However, the ToT method has a strong non-linearity in processing a signal and it is not obvious how the position resolution will be affected when the waveform fluctuated from a standard signal. To realistically estimate the resolution, we performed a simulation study to better understand of the process of electron avalanche in PPACs. This study will provide essential information for improving the resolution of SR-PPACs. In this paper, the details of the simulation and present results are reported.

We used Garfield++ [4], which is a toolkit for computing electric field, ionization, electron transportation, and avalanche in gas detectors [5, 6]. It provides a microscopic Monte Carlo calculation using the reaction cross-section of electrons and atoms by a Magboltz program [4]. The parameters of the simulation in this work are shown in Table 1. The sizes of electrodes and strips are the same as the standard-type SR-PPAC [3]. The counter gas was pure $i$-$C_4H_{10}$. Garfield++ has a library of mobility of ions for several gasses such as Ar and $CO_2$, however, it does not include that of $i$-$C_4H_{10}$. In this work, we referred to Ref. [7] to deduce the mobility of ions in $i$-$C_4H_{10}$.

Table 1. Parameters in the simulation model of SR-PPAC

| Anode | size | 240 mm × 150 mm |
|---|---|---|
| | anode - cathode gap | 4 mm |
| Cathode | size | 240 mm × 150 mm |
| | strip size | 2.5 mm × 150 mm |
| Gas | type | $i$−$C_4H_{10}$ |
| | temperature | 298 K |

A single electron was simulated to drift from a cathode (y=0 [cm]) to an anode (y=0.4 [cm]) with an electric field applied. The calculated trajectories of the resultant electron avalanche are shown in Figure 1. The applied biases to the anode and the cathode were set to 750 V and 0 V, respectively. The gas pressure was 10 Torr. As seen in Figure 1, the electron avalanche grows up as a single electron drifts from the center of cathode to anode planes. The signal collected from a strip of the cathode plane was also calculated using a convolution integration of the charge induced in the strip using the response function of the preamp [8,9]. The calculation result of analog output and the real signal of $\alpha$ source measured by oscilloscope are shown in Figure 2. The sharp peak around 100 ns is the signal of the mirror charge of electrons and the broad peak around 2 $\mu$s is one of the real ions. The signal of ions will be filtered by a shaper in the Amplifier-Shaper-Discriminator (ASD) board and it will not affect signal collection time using the ToT method.
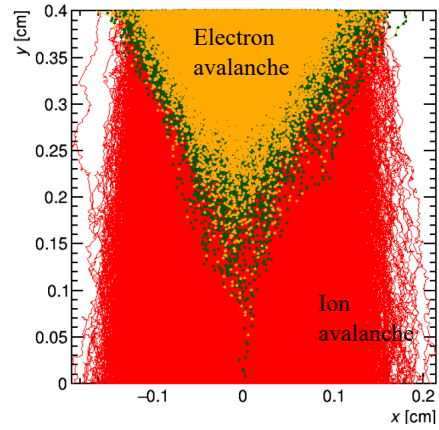


Figure 1. Track of electron and ion avalanche calculated by Garfield++. For details refer to text.

In the previous test experiment of SR-PPAC, we compared the impact of gas pressure on position resolutions of SR-PPAC operated under pressures of 5 Torr and 10 Torr. The resolution at 10 Torr was 1.2 times better than at 5 Torr. One possible factor which causes the worse resolution at lower pressure is lateral diffusion of the electron avalanche. The diffusion coefficients calculated by this simulation are shown in Table 2 for the two conditions. We calculated the distribution of the center of mass of the multiplied electrons. The result in the case of 10 Torr is shown in Figure 3. The standard deviations were obtained as 160 $\mu$m in the case of 10 Torr and 212 $\mu$m in the case of 5 Torr. It indicates that the diffusion in the lateral direction is larger in the case of 5 Torr than in the case of 10 Torr. The detailed analysis of processing signals converted from analog to digital in the ASD board is now ongoing.

Table 2. Calculated value of lateral diffusion coefficient

| condition | lateral diffusion coefficient [cm$^{\frac{1}{2}}$] |
|---|---|
| 10 Torr, 690 V | 0.0687 |
| 5 Torr, 530 V | 0.0791 |

**References**

[1] H.Kumagai, *et al.*, Nucl. Instrum. Meth. Phys. Res. A, **470**, 561 (2001).

[2] S.Hanai, *et al.*, CNS Annual Report.2019 **317**, (2021).

[3] S.Hanai, *et al.*, CNS Annual Report.2020 **317**, (2022).

[4] Garfield++ , https://garfieldpp.web.cern.ch/garfieldpp/

[5] A.Tanaka, *et al.*, 2013 *JINST* **8** C10023.

[6] Natália F. Silva, *et al.*, 2021 *J. Phys,: Conf. Ser.* **1826** 012046.

[7] A.F.V. Cortez, *et al.*, 2019, *JINST* **14** P04010.

[8] REPIC, RPA-132 64ch CHAMMBER PREAMP CARD, https://www.h-repic.co.jp/products/wirechamber/special_order/rpa_132

[9] ATLAS Thin Gap Chamber Amplifier-Shaper-Discriminator ICs and ASD Boards, ATLAS Internal Note MUON -NO- 1 October, 1999.

Figure 2. (Left) Simulated signal of one strip of cathode plane. The sharp peak represents signal of electrons and the broad peak around 2$\mu$s represents signal of ions. (Right) A signal of analog output of ASD board using $\alpha$ source measured by oscilloscope. The lower line represents the signal from one strip of a cathode. The polarity was inverted by preamp. The gas pressure was 10 Torr and the applied voltage was 750 V. The upper line is a signal from the anode and it's irrelevant to the present study.
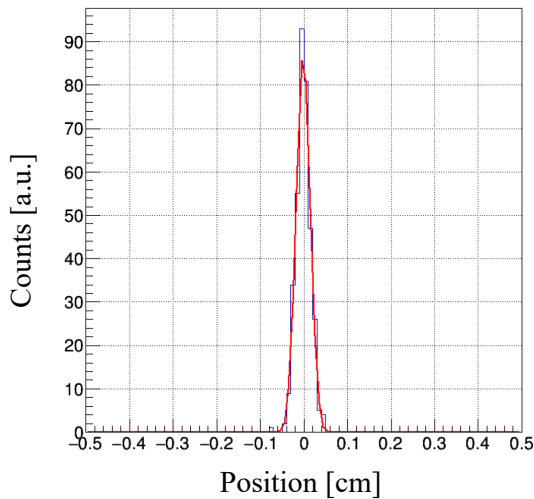


Figure 3. A calculated distribution of a center of mass of electron avalanche on the cathode plane. This figure shows the case of 10 Torr and 690 V. The standard deviation obtained by gaussian fitting was 160 $\mu$m.

In the furure this simulation will allow us to estimate the effect of non-linearity in the ToT method on the position extraction. SR-PPAC has a fast response and it is expected that the detector has a good time resolution using sharp electron signals. We also plan to estimate the effect of fluctuation in the process of electron avalanche on its time resolution.

# Development of position-sensitive mosaic detector

J. T. Li, N. Imai, R. Kojima, R. Yokoyama, T. Chillery and S. Michimasa *Center for Nuclear Study,*

*Graduate School of Science, University of Tokyo*

Search for Island of Stability is one of the most popular topics in nuclear physics. In order to design the experiments to explore Very Heavy (VH) / Super Heavy (SH) regions and furthermore towards Island of Stability, we need a model that can give precise predictions on reaction cross section. However, for the Fusion-Evaporation reaction which has been proved theoretically a feasible way to approach Island of Stability [1, 2], reaction dynamics has not been established yet. In particular, quantitative understanding of the fusion hindrance effect is far from being achieved due to lack of experimental studies. Experiments have been scheduled at Heavy Ion Medical Accelerator in Chiba (HIMAC) to study fusion hindrance effect.

Measurement of $\alpha$-decay energies is a conventional yet powerful way to identify Evaporation Residuals (ERs) produced in fusion reactions and to extract fusion cross sections. In our HIMAC experiments, the thickness of target and back material is determined so that, after the reaction, the beam will pass through while ERs will be stopped in the back material and emit $\alpha$ particles at various angles like shown in Fig. 1. Therefore, position sensitive detectors are needed to compensate for the angular difference as shown in Fig. 2.
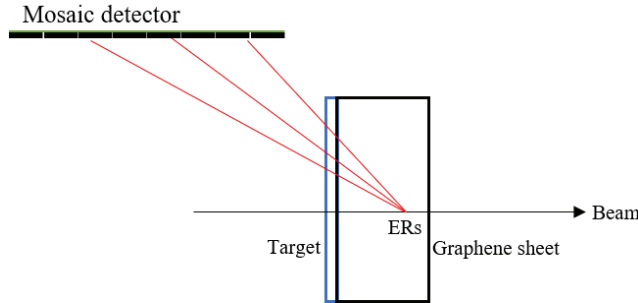


Figure 1. Side view of the experimental setup.
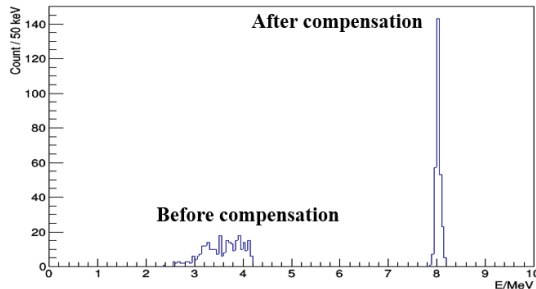


Figure 2. Simulated $\alpha$-energy spectrum for 8-MeV $\alpha$ particle.

Apart from the requirement of position sensitivity, testing the performance of our detectors against the high-intensity beam is another object of this study, therefore ex-

pensive Double-sided Silicon Strip Detector (DSSD) should be avoided. Based on reasons above, we have planned to develop a mosaic-type detector constituted by matrices of Si Photo-Diodes (PDs). Considering the position uncertainty as well as the price, the type of PD was chosen to be Hamamatsu S13955-01 with single size of $7.52 \times 7.52$ mm, as shown in Fig. 3. The intrinsic resolutions originated from the finite size of PD are simulated to be about 1% for $\alpha$ particles with energy of 6-10 MeV. The total price of a $10 \times 10$ matrix is 300,000 yen while one TTT (a DSSD) costs 2500,000 yen.
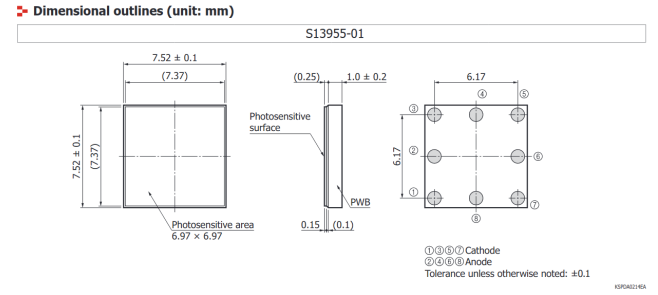


Figure 3. The dimensional plot of S13955-01 PD. Taken from [3].

Several tests have been performed. The dead layer of the PD was estimated by measuring $\alpha$ source, and the electric circuit is shown in Fig. 4.
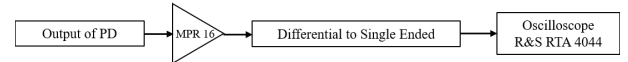


Figure 4. Electric circuit for estimation of the dead layer.
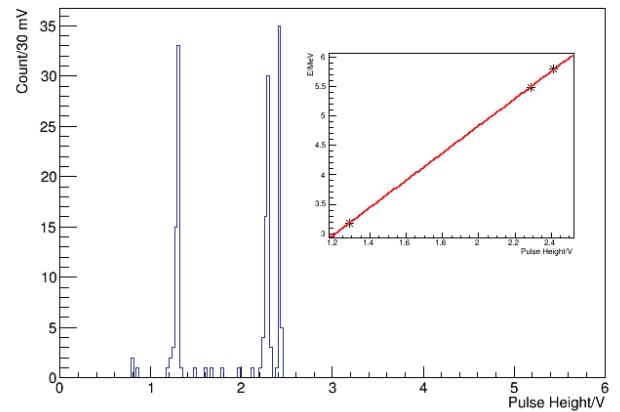


Figure 5. The spectrum of the pulse heights.

Figure 5 shows the obtained spectrum of 3 $\alpha$-lines, where the inset figure shows the linear fitting between the pulse heights and $\alpha$ energies. The offset $203 \pm 43$ keV corresponds to the energy loss of $\alpha$ particles in the dead layer,

and the thickness of the dead layer was calculated as 1.24 ± 0.14 ¯m.

In our experiments, we will measure the $\alpha$ particles with the energy range of 6-10 MeV. The effective range of the PD was tested using a 6.5 MeV/u $\alpha$ beam at E7B course. The $\alpha$ particles scattered by an Au foil (1 ¯m) were detected by the PDs. Al degraders with two kinds of thickness were placed in front of two PDs. We managed to observe the elastic scattering events with two energies as shown in Fig. 6. The large peak width was caused by the energy straggling in Al and noise. Since $\alpha$ particles with the energy deposit in the PD of 14 MeV were observed, the effective thickness of the Si is at least larger than 120 ¯m. Therefore, we conclude that such PD is capable to meet our experimental requirements to measure $\alpha$ particles with the energy up to 10 MeV (range in Si: 68 ¯m).
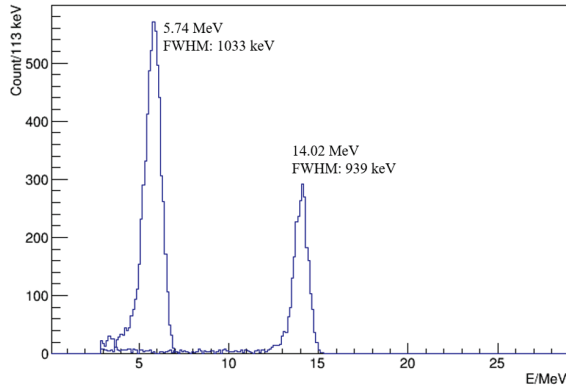
Figure 6. Experimental $\alpha$-energy spectrum.

Due to the small size of the electrodes on the PD, normal soldering is too difficult to apply, and the reflow soldering was considered instead. For that purpose, a readout Printed Circuit Board (PCB) was designed as shown in Fig. 7, where up to 10 PDs can be mounted. Signals are read by a 20-pin flat connector.
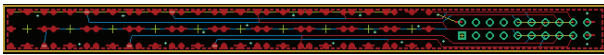
Figure 7. Readout PCB for mosaic detector.

Figure 8 shows a prototype of 10 PDs made by the reflow soldering using a hot plate. A few trials have been carried out while PDs can be easily removed from the PCB after reflow soldering. Finally, the optimized temperature condition was tuned to be 30 s for soldering after the temperature of PDs reaches 230 °C.

The prototype was tested by $\alpha$ source using the electric circuit as shown in Fig. 9.
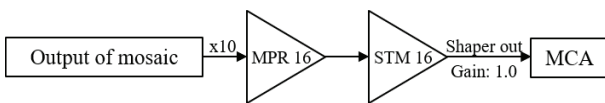
Figure 9. Electric circuit for test of the prototype.

Figure 10 shows the measured spectrum of one channel in the prototype, the normal intrinsic resolution was about 150 keV in $\sigma$ at around 5.5 MeV (the resolution is the same
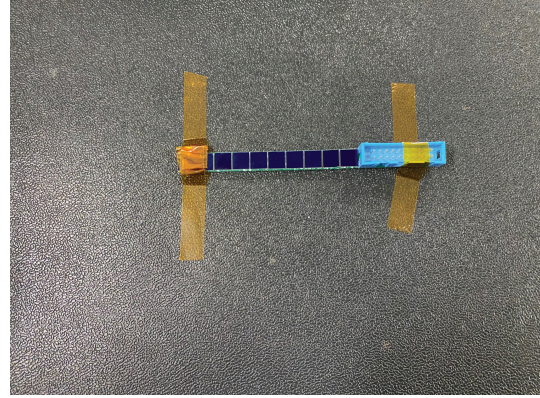
Figure 8. Reflow soldering of the prototype which was placed in a hot plate.

with and without the PCB). However, the intrinsic resolution obtained in Fig. 5 (with PCB) was about 40 keV in $\sigma$ at around 5.5 MeV. Clearly, the resolution was deteriorated when using the electronics in Fig. 9, the reason is unknown for now and we need to find out the problems causing the poor resolutions.
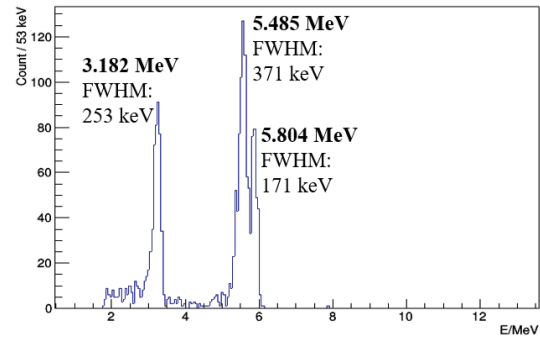
Figure 10. Measured $\alpha$-energy spectrum of one channel.

In conclusion, for the measurement of $\alpha$ decay of ERs produced in fusion-evaporation reactions, we plan to develop a position-sensitive mosaic detector made of Si PDs. A prototype has been made and tested. The manufacturing of the detector arrays will start soon.

### References
[1] L. Zhu et al., Phys. Lett. B **829**, 137113(2022).
[2] T. Nomura and Y. Abe. Journal of the Physical Society of Japan. **50**, 9(2005).
[3] Hamamatsu Photonics K.K. Back-illuminated photodiodes with CSP structure.

# Development of a Multiplexer circuit at CRIB

K. Okawa, S. Hayakawa, N. R. Ma, H. Shimizu, H. Yamaguchi and Q. Zhang

*Center for Nuclear Study, Graduate School of Science, University of Tokyo*

## 1. Introduction

The Center for Nuclear Study (CNS) low-energy Radio-Isotope Beam separator (CRIB) [1–3] is a facility providing the RI beam of around below 10 MeV/nucleon located at the RIKEN Nishina Center. Since the last year, experiments of the $^6$He beam production [4] and the $^{26}$Si$(\alpha, p)^{29}$P reaction have been performed.

The data taken from a scattering chamber at the last focal plane are transferred by coaxial cables to the counting room (J1) and processed by DAQ system in J1. The number of the channels that could be handled was limited by the number of feedthroughs in the chamber, the signal processing modules and the cables connecting the experimental room (E7) to J1. Therefore, a multiplexer circuit was introduced, Mesytec MUX [5], which can handle more channels compared with previous CRIB experiment.
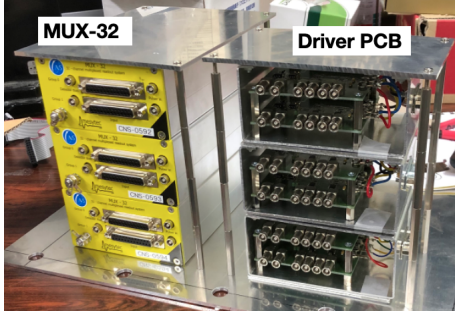


Figure 1. The picure of MUX and Driver PCB. (see section 2).

## 2. Detail of the MUX

The MUX module is a 16-channel multiplexed combination of preamps, shapers and discriminators that can accept up to two simultaneous hits within 50 ns. The output signals are two shaper (energy) signals, two position signals and a trigger (timing) signal. The position signals are discrete voltages corresponding to the number of the input channels. Figure 2 shows an example of the position signals from a 16 strip silicon detector after processing by an ADC. Each peak of the position signal corresponds to a single strip, therefore, when we select the events of the single peak, we can obtain energy data for each strip.

The output connector of the MUX itself is a 20-pin flat cable, but the connector of the cables that connected between the E7 and J1 is the LEMO connector. In addition, the energy outputs from the MUX itself is up to 3.5 V, but the ADC range we used (MADC [6]) can be set up to 10 V. Therefore we introduced the "Driver PCB" (Figure 1). It can convert the flat cable connector to the LEMO connectors, and the voltages can be amplified up to 10 V. By increasing the range of the signals, it becomes easier to remove smaller voltage noise.
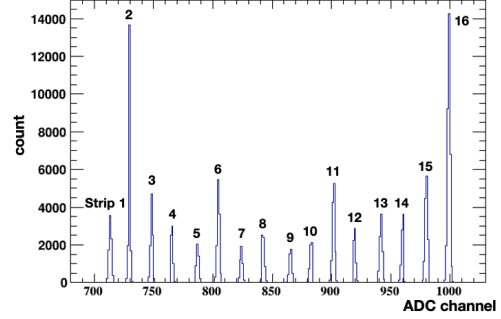


Figure 2. An example of the position outputs from the MUX. This shows the spectrum after processing by an ADC.

## 3. Development

Firstly, we put the MUX and Driver PCB into the E7 with a pulser. When the pulser signals were connected to the MUX, two consecutive channels responded as two simultaneous hits. Figure 3 shows the result of the pulser inputed test and the data had so large noise that each position signal could not be separated. Therefore, we checked the raw signal with an oscilloscope at J1 and we found $V_{pp} = 30$ mV and 100 Hz noise in the baseline. When we checked at E7, the large noise could not be seen, therefore, the source of the noise was caused by the long-distance transmission from E7 to J1.
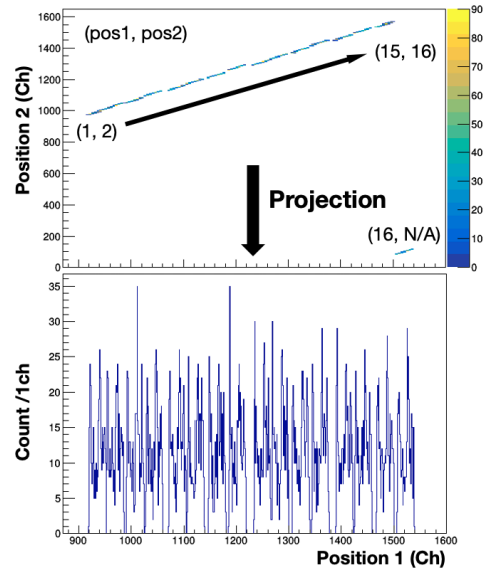


Figure 3. The upper figure shows the correlation of the signals from positions 1 and 2 and the lower figure shows the spectrum of position 1.

These cables were out of the control, so we decided to use a filter to reduce the noise. The frequency of the noise

was 100 Hz, and we tested a simple high-pass filter (HPF) to reduce the low frequency noise (Figure 4). The cut-off frequency ($f_c$) of this filter is given by

$$f_c = \frac{1}{2\pi CR}.$$

We then measured the peak-to-peak voltage of the noise ($V_{pp}$) and the range of the position output after processing them with an ADC by changing this $f_c$.
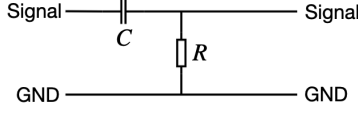
Figure 4. Circuit of a first-order high-pass filter.



Figure 5. The energy spectra of the alpha source. The left figure shows the data from the original circuit at CRIB and the right figure shows the MUX circuit. The detector and the DAQ setup were different for each circuit, but both were SSSD with a thickness of 20 $\mu$m. The energy resolution (FWHM/E) at the 3.148 MeV peak was 6.7% and 5.4% in the left and right figures respectively.

Table 1. Result of the HPF test. The $V_{pp}$ was measured with an oscilloscope and the errors included parallax error and noise fluctuations. The range was the ADC channels between the center of the peak of strip 1 and that of strip 16 peak and measured with an accuracy of 10 Ch from the spectrum.

| No. | $C$ | $R$ | $f_c$ | $V_{pp}$ | ADC Range |
|-----|-----|-----|-------|----------|-----------|
| #   | ($\mu$F) | (k$\Omega$) | (Hz) | (mV) | (Ch) |
| 1 | 0.1 | 0.10 | $\sim 1.6\times 10^4$ | 5(2) | 380 |
| 2 | 0.1 | 0.47 | $\sim 3.4\times 10^4$ | 6(2) | 530 |
| 3 | 0.1 | 1.0 | $\sim 1.6\times 10^3$ | 6(2) | 570 |
| 4 | 0.1 | 5.0 | $\sim 310$ | 20(4) | 580 |
| 5 | 0.1 | 10.0 | $\sim 160$ | 22(4) | 590 |
| 6 | | no filter | | 30(5) | 620 |

The result in Table 1 suggests that the circuits #4 and #5 could not reduce the noise completely. Also because the circuit #1 had a large $f_c$ value, the true signal was also attenuated and the range became smaller. If the consecutive peaks of the position outputs are narrower, the peaks are more likely to be overlapped by some noise, so it is desirable to make the distance between the peaks larger. Therefore, we adopted the circuit #3 and introduced this HPF after the Driver PCB for all the channels of the MUX circuit.

Figure 5 shows the alpha source test between the original circuit used at CRIB and the MUX circuit with the HPF. Both comparison figures represent the data from a single strip of Single-Sided Silicon Detector (SSSD). Although the input ranges of the ADC and the Si detectors we used were different, we were able to achieve almost the same energy resolution with the MUX circuit as with the original circuit.

## 4. Summary and outlook

In order to send more data to the counting room J1, a multiplexer module, the Mesytec MUX, was introduced, which could convert 16 channel signals into two energy signals, two position signals and a timing signal. In addition, the HPFs were introduced to reduce the noise, and the MUX could be used to take the data correctly.

This circuit was used in the $^{26}$Si($\alpha, p$)$^{29}$P experiment at CRIB in January 2022 in the long-distance transmission,

and data were obtained from many channels. However, we found some important problems in the experiment. The MUX and PCB driver were very sensitive to the noise, and sometimes the position outputs became so noisy that they could not be separated. Therefore, we need to find the cause of the noise, and noise reduction should be done thoroughly before using the MUX.

## References

[1] S. Kubono *et al.*, Eur. Phys. J. A. **13** (2002) 217.
[2] Y. Yanagisawa *et al.*, Nucl. Instrum. Meth. A. **539** (2005) 74.
[3] H. Yamaguchi, D. Kahl, and S. Kubono Nucl. Phys. News Int. **30** (2020) 21.
[4] H. Yamaguchi *et al.*, CNS Annual report. (2020) 9.
[5] Mesytec GmbH & Co., datasheet of MUX-16/-32/-64. https://www.mesytec.com/products/datasheets/MUX-16.pdf
[6] Mesytec GmbH & Co., datasheet of MADC-32. https://www.mesytec.com/products/datasheets/MADC-32.pdf

# Design of the optical lattice trap as a tool for precision spectroscopy using heavy atoms

N. Ozawa, K. Nakamura, S. Nagase, T. Nakashita[a,b], H. Nagahama, and Y. Sakemi

*Center for Nuclear Study, Graduate School of Science, University of Tokyo*
[a]*Graduate School of Arts and Sciences, University of Tokyo*
[b]*RIKEN (The Institute of Physical and Chemical Research)*

The permanent electric dipole moment (EDM) of the electron violates P (parity) and T (time reversal) symmetries, and is one of the probes for beyond-Standard-Model (BSM) searches. In particular, T-violation is equivalent to CP (charge–parity) violation under the CPT theorem, which is one of the requirements for the matter-antimatter asymmetry observed in our Universe to exist [1]. Relativistic coupled cluster calculation shows that the atom of the heaviest alkali, francium (Fr), enhances the electron EDM by a factor of 799 [2], and is a promising tool for a sensitive EDM search.

A large ensemble of laser-cooled Fr atoms is required for a high-sensitivity measurement of the EDM. $^{210}$Fr can be produced at the intensity of $10^6$ per second at the RIKEN Nishina Center for Accelerator-Based Science (RNC) [3], and conventional laser cooling techniques such as magneto-optical trap (MOT) and optical lattice (OL) are applicable thanks to the alkali atomic structure [4]. In particular, trapping the atoms in an OL can suppress spin decoherence by atomic collision and elongate the measurement duration. In this work, the design for the planned OL is described.

The one dimensional (1D) OL is the potential formed by a standing wave of off–resonant continuous–wave linearly polarized light, described in the form:

$$U_{\text{OL}} = \frac{4\alpha(\omega)P}{\pi\varepsilon_0 c w(z)^2} \exp\left(-\frac{2r^2}{w(z)^2}\right)\cos^2(kz), \quad (1)$$

where $\varepsilon_0$ is the permittivity of vacuum, $c$ is the speed of light, $\alpha(\omega)$ is the atomic polarizability against light of angular frequency $\omega$, $k = \omega/c$ is the wavenumber, and $P$ is the input beam power, assuming that it is retroreflected [3] by a mirror at one end. We take the $z$ axis as the beam axis and $r = \sqrt{x^2 + y^2}$ as the radial distance. $w(z)$ is the radius at position $z$ at which the beam intensity becomes $1/e^2$ of maximum ("$1/e^2$-radius"), and theoretically follows

$$w(z) = w_0\sqrt{1 + \left(\frac{z - z_0}{z_{\text{R}}}\right)^2}, \quad (2)$$

for a beam which has a Gaussian distribution. Here, $w_0$ is the $1/e^2$-radius at the focal point $z = z_0$, and $z_{\text{R}} = \pi w_0^2/\lambda$ is the Rayleigh length, where $\lambda$ is the wavelength of the laser beam.

We call the ratio between the number of atoms trapped in the lattice against those originally trapped in the MOT prior to the loading as the "loading rate". Since Fr is not readily accessible, it is advantageous to find the optimal lattice parameters to yield the maximum loading rate without relying on experimental trial and error.

It is known that the loading rate follows the scaling rule $aP^{3/2}$ at low powers, and eventually shifting to $aP^{1.25}$, originally derived by mathematical analysis [5]. The coefficient $a$ depends on the characteristics of the trap, and is determined by fitting to the experimental result. A new approach to determine the loading rate without experimental results is to rigorously trace the motion of atoms under the influence of the lattice potential [6]. By solving classical equations of motion for each atom, it has been confirmed that the simulation follows the scaling law above, and also roughly resembles the experimental results of $^{87}$Sr, $^{88}$Sr, $^{174}$Yb, and $^{199}$Hg, with slight overestimates due to idealized trap structures.

The latter approach requires a significant amount of computational time compared to the former, but has the advantage that the spatiotemporal structure of the trap can be easily extended, for example to a "moving lattice" as mentioned later, or a slowly fluctuating lattice due to noise. We have thus developed a C++ code to estimate loading efficiencies of the 1D OL, following the work of Watson *et al.* [6,7]. Since we mainly focus on the simulations of alkali atoms such as Rb, Cs, and Fr, the original input parameter of atomic polarizability has been replaced by the semiclassical approximation [8]:

$$\alpha(\omega) = \pi\varepsilon_0 c^3\left\{\frac{2\Gamma_{\text{D2}}}{\omega_{\text{D2}}^3}\frac{1}{\omega - \omega_{\text{D2}}} + \frac{\Gamma_{\text{D1}}}{\omega_{\text{D1}}^3}\frac{1}{\omega - \omega_{\text{D1}}}\right\},$$

where $\Gamma_{\text{D1}}$ and $\omega_{\text{D1}}$ are the natural linewidth and resonance frequency for the D1 transition, and $\Gamma_{\text{D2}}$ and $\omega_{\text{D2}}$ are those of the D2 transition. We have also allowed the beam powers, widths, and frequencies of the forward and backward beams to vary independently, so that the simulation can be simply extended to a time-dependent and complicated experimental scheme.

Using the developed code, we have calculated the loading rate of $^{87}$Rb atoms from the MOT directly to the optical lattice. An additional term has been added to the potential to represent gravity in the $-y$ (transverse) direction, and the time step of 0.1 $\mu$s and displacement step of 10 pm for the potential gradient calculation are chosen, which do not produce significant numerical error for our use. 1000 $^{87}$Rb atoms are randomly generated following a 3D Gaussian distribution of $1/e$-radius [4] 100 $\mu$m, and their initial velocities

---

[3]Terminology of the OL meaning "to be reflected so that the reflected beam propagates on the same axis but in the opposite direction as the incoming beam".

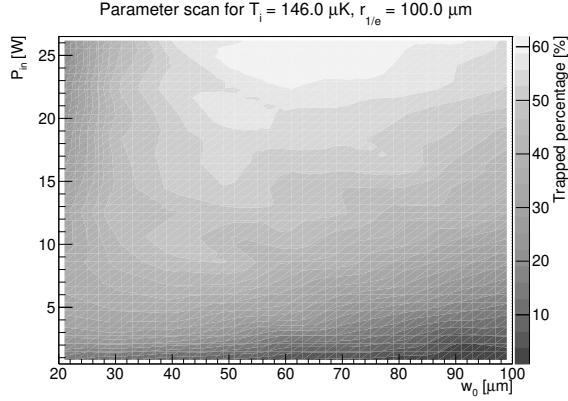[4]A typical measure to characterize the atomic cloud size; equivalent to

Figure 1. Calculation result of OL loading rate of $^{87}$Rb as a function of beam width $w_0$ and power $P$.

are given according to the 3D Maxwell-Boltzmann distribution of mean temperature equal to the Doppler temperature of 146 $\mu$K, which is the lowest temperature attainable by an MOT in principle. The simulation is stopped at time 100 ms, and the number of atoms remaining within 3 standard deviations of the potential width in the radial direction and 3 standard deviations of the initial atom cloud distribution in the axial direction are counted to yield the loading rate. The calculation result as a function of beam power $P$ and beam radius $w_0$ is shown in Fig. 1. The loading rate is expected to exceed 50% for $w_0 \sim 70$ $\mu$m and $P \sim 25$ W. In practice, a high power laser beam could induce photon scattering on the atoms and deteriorate the EDM measurement sensitivity, and could also destroy optical components that are vulnerable to heat, so a power in the range of a few watts is preferred. Also, the optimal beam width for a given power decreases for low power, since a smaller beam width will effectively a deeper potential, based on Eq. 1. When the beam width is too small, however, the overlap volume between the MOT and OL becomes so small that the loading rate does not increase with power. Note that this calculation has only been carried out once per each data point, so regions of low loading efficiencies are more susceptible to statistical error.

Based on this calculated result, we are preparing optical components to produce the 1D OL. As a first step, we aim to trap $^{87}$Rb atoms in a MOT vacuum chamber dedicated for offline experiments. The beam of wavelength 1064 nm is generated from a Nd:YAG laser source and amplified with a fiber amplifier. The beam is then sent to the vacuum chamber via a single-mode polarization-maintaining optical fiber.

The diverging beam emitted from the fiber is collimated to a beam diameter of 1.24 mm to 3.92 mm by a zoom fiber collimator, which is then focused by a lens to yield a minimum spot size of $w_0 = 21.61$ $\mu$m to $w_0 = 68.32$ $\mu$m at the center of the MOT region. A mirror is placed at the other side of the chamber, which reflects the beam back to the MOT region, forming a 1D OL.

By establishing the technique for an efficient loading into the 1D OL, we plan to utilize it for the Fr atomic EDM measurement. In order to minimize sources of resid-

ual magnetic fields or background gas, the EDM measurement region is preferably separated from the MOT region. One method to transport the atoms from the MOT region to the EDM measurement region is to introduce a slight frequency detuning between the two beams forming the OL [9], known as the "moving lattice". This is a technique often employed to transfer atoms without heating them [10, 11], and much precedent research has been conducted on the characterization of the physical background [12, 13], but there are not many cases where numerical estimates of the loss of atoms during the transportation has been thoroughly evaluated. Extending our calculations to the transportation of atoms and making quantitative comparisons to experimental data will enable us to evaluate the achievable EDM measurement precision in more detail.

## Acknowledgements

## References

[1] T.E. Chupp, P. Fierlinger, M.J. Ramsey-Musolf, and J.T. Singh, Rev. Mod. Phys. **91** (2019) 015001.

[2] N. Shitara, N. Yamanaka, B.K. Sahoo, T. Watanabe, and B.P. Das, J. High Energy Phys. **2021** (2021) 124.

[3] H. Nagahama, K. Nakamura, N. Ozawa, *et al.*, RIKEN Accel. Prog. Rep. **53** (2019) 57.

[4] G.D. Sprouse and L.A. Orozco, Annu. Rev. Nucl. Part. Sci. **47** (1997) 429.

[5] J. Wu, R. Newell, M. Hausmann, D.J. Vieira, and X. Zhao, J. Appl. Phys. **100** (2006) 054903.

[6] R.S. Watson and J.J. McFerran, J. Opt. Soc. Am. B **38** (2021) 36.

[7] J. McFerran "The Watson Optical Trap Simulator", Mathworks (2020), https://au.mathworks.com/matlabcentral/fileexchange/79568-the-watson-optical-trap-simulator.

[8] R. Grimm, M. Weidemüller, and Y.B. Ovchinnikov, Adv. At. Mol. Opt. Phys. **42** (2000) 95.

[9] M. Raizen, C. Salomon, and Q. Niu, Phys. Today **50** (1997) 30.

[10] I. Ushijima, M. Takamoto, M. Das, T. Ohkubo, and H. Katori, Nat. Photonics **9** (2015) 185.

[11] X. Zheng, J. Dolde, V. Lochab, B.N. Merriman, H. Li, and S. Kolkowitz, Nature **602** (2022) 425.

[12] M.B. Dahan, E. Peik, J. Reichel, Y. Castin, and C. Salomon, Phys. Rev. Lett. **76** (1996) 4508.

[13] S.R. Wilkinson, C.F. Bharucha, K.W. Madison, Q. Niu, and M.G. Raizen, Phys. Rev. Lett. **76** (1996) 4512.

---

$\sqrt{2}\sigma$ when $\sigma$ is the standard deviation.

# The study on beam viewer photography technique of the emittance monitor for the accelerated ion beams by AVF Cyclotron

Y. Kotaka, K. Kamakura, H. Yamaguchi, N. Imai, Y. Sakemi, J. Ohnishi[a], A. Goto[a], M. Kase[a], K. Hatanaka[b], S. Shimoura

*Center for Nuclear Study, Graduate School of Science, University of Tokyo*
*[a]RIKEN Nishina Center*
*[b]Research Center for Nuclear Physics, Osaka University*

## 1. Introduction

There are 3 experimental courses in the E7 room of RIKEN Nishina Center. On these courses, the experimental equipments of CNS are installed. When the beam intensity is less than 10 e$\mu$A, the overall average beam transport efficiency of those courses is 73 %. When the beam intensity is larger than 10 e$\mu$A, the overall average beam transport efficiency is 66 %. It is found that the stronger beam intensity tends to lower beam transport efficiency. For improving the beam transport efficiency, the optimization of the beam transport system is necessary. The cause for the decrease of beam transport efficiency is thought to be the increase of the beam emittance. However, high intensity beam emittances cannot be measured by the existing emittance monitor because of the insufficiency of cooling power [1,2].

We are developing the pepper-pot emittance monitor (PEM) [3,4] for the high intensity beam. In this fiscal year, the radiation protection for the digital camera of emittance monitor was studied. The ideas are to separate the camera from beamline and to cover the camera with shield material. Besides, the low performance and inexpensive camera is adopted in terms of frequent exchanges as the deterioration of camera cannot be helped.

## 2. Calibration of viewer coordinate

The remote calibration of the coordinate system on the fluorescent plate of PEM are developed because the rooms where PEM is to be installed are closed during the beam time and cannot be entered frequently. Formerly a graph paper was used for the calibration. This way needs to raise the inner pressure of beamline to atmospheric pressure, to remove PEM from beamline, and to exchange fluorescent plate to graph paper. To leave off these works, we decided to draw lines by scratching in a grid pattern at 5 mm interval on the copper plate shown in the left of Fig. 1. The fluorescent agent is poured on the copper plate to a thickness that allows the lines to be recognized shown in the right of Fig. 1. The cross-point positions were compared with graph paper to see working accuracy. Figure 2 shows the cross-point positions of the fluorescent plate (○) and of the graph paper (+) indicated by the bit-mapped coordinate system. The average and standard deviation of the differences at cross-point positions between the fluorescent plate and graph paper is 2.5±1.0 pixel, respectively. As 1 pixel correspond to 0.08 mm averagely, 2.5 pixel corresponds to 0.2 mm. The accuracy is the lower limit for handmade drawing.
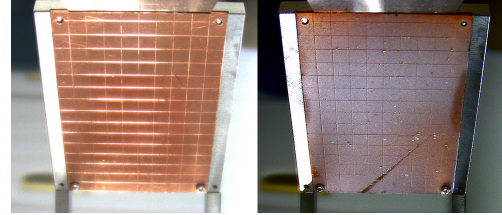


Figure 1. Left image is lines by scratching on the copper plate. Right image is the copper plate poured with potassium bromide (KBr).
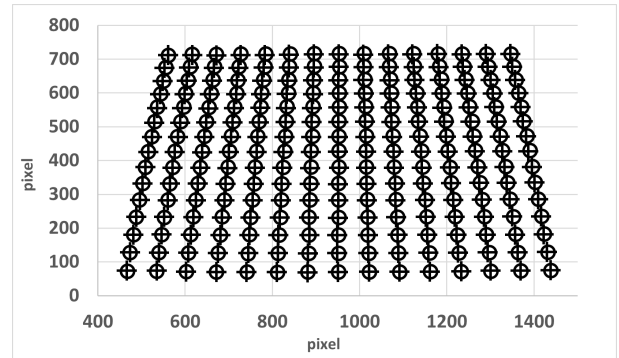


Figure 2. The comparison between the cross-point position of the copper plate (○) and of the graph paper (+).

## 3. Optical system of digital camera

The optical system with a tele lens was studied to keep away from the deterioration by radiation. For the low performance and inexpensive digital camera, we selected CMOS sensor because it would be more tolerant of radiation, and it is less expensive than CCD sensor. Although the number of pixels of CMOS sensor is 2.2 megapixel (MP), final resolution is degraded to 0.35 MP because the output signal of our selected digital camera is analog.

The required conditions for the optical system are to take an all-around image of fluorescent plate and to suppress the distortion of the image. The setup of this study is shown in Fig. 3. As the diameter of window is 40 mm, the entire region of the fluorescent plate cannot be seen at long distances from a camera only with tele lens. However, there are some solutions that the entire region of the fluorescent plate can be seen when a intermediate lens is added between the fluorescent plate and tele lens. The focal length of tele lens used for study is 100 mm. As shown in Fig. 4, the distance between the intermediate lens and window and the distance between the digital camera and window are defined as d (m) and L (m), respectively.

The achieved longest L is 1940 mm by now. At this time,

d is 480 mm. An achromatizing lens was adopted for the intermediate lens because it has an ability to suppress the distortion of image. The image of fluorescent plate under this condition is shown in the top of Fig. 4. Almost all regions can be seen besides the four corners. The distortion is indicated as the relationship between the fiducial (designed) positions and the difference from the positions on the image to fiducial (designed) positions shown in the bottom of Fig. 4. The differences are caused by not only distortion, but the error made from drawing lines on the copper plate. The standard deviations of the difference on the horizontal and vertical directions are 0.12 mm and 0.08 mm, respectively. The estimated beam angle error is 1 mrad as the length between the pepper-pot mask and the center of the fluorescent plate is 125 mm, which is adopted for the prototype.
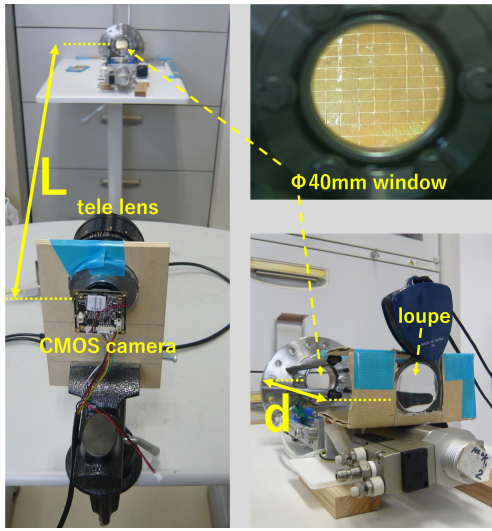


Figure 3. Setup of optical system with tele lens and intermediate lens. The distance between the intermediate lens and window is defined as d (m). The distance between the digital camera and window is also defined as L (m).
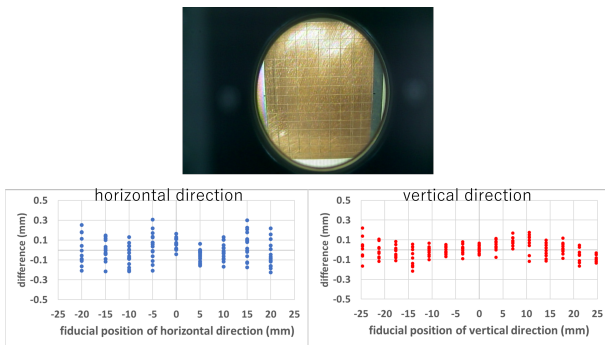


Figure 4. The top image is fluorescent plate on condition that L is 1940 mm and d is 480 mm. The bottom left and right are the correlation between fiducial positions and the difference from the positions on the image to fiducial positions in the horizontal and vertical directions, respectively.

## 4. The performance test with accelerated ion beam

The performance test of the prototype PEM was done with ion beam. However, we set the low performance cam-era at about L=500 mm interval from the window of the PEM because the optical system with tele lens was not ready in time for the beam time. As the condition that entire region of fluorescent plate fitted in a camera view was not found, we decided to take the beam image on a part of fluorescent plate.

The exposed ion beam was $^{24}Mg^{8+}$ 7.5 MeV/u and the beam power was 23 W which was correspond to 1020 enA. The vector of average beam angles through the holes of pepper-pot mask is shown in Fig. 5. Though the region where x is 20 mm or more and y is 6 mm or more and -17 mm or less is out of the camera view, the measurements of the beam positions and angles is useful for the performance evaluation. We compared the measurement of the PEM with the measurement of beam profile monitor set 4500 mm behind the PEM. As both measurements are not consistent currently, we are investing the cause.
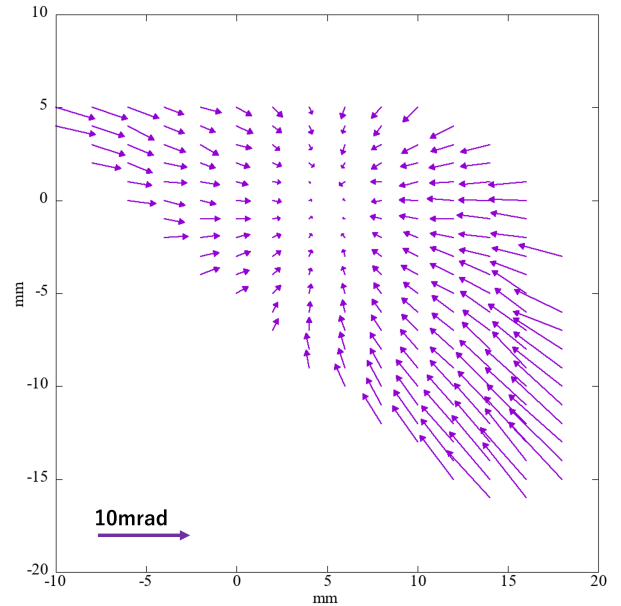


Figure 5. The angular vector at each position of beam through each hole of the pepper-pot mask.

## References

[1] Y. Kotaka *et al.*, CNS Ann. Rep. 2020 (2022), p.43-44.
[2] Y. Kotaka *et al.*, Proc. 18th Annual Meeting of PASJ, (2021), p.873-877.
[3] L. E. Collins and P. T. Stroud, Nucl. Instr. and Meth. **26** (1964), p.157-166.
[4] T. Hoffmann *et al.*, AIP Conf. Proc. **546**, 432 (2000).

# ECR Plasma Studies for Heavy Ion Production at HyperECR Ion Source

K. Kamakura, Y. Kotaka, T. Nakagawa[a], J. Ohnishi[a], K. Hatanaka[b], A. Goto[c], H. Yamaguchi,
N. Imai, S. Shimoura and Y. Sakemi

*Center for Nuclear Study, Graduate School of Science, the University of Tokyo*
[a]*Nishina Center for Accelerator-Based Science, RIKEN*
[b]*Research Center for Nuclear Physics, Osaka University*
[c]*Institute of Materials Structure Science, KEK*

## 1. Introduction

CNS 14 GHz HyperECR ion source provides various ion beams to the RIKEN AVF cyclotron. [1] We have been focusing on the increase of the intensity of multiply charged heavy ions by improving extraction electrodes, metal vapor generation methods, etc. [2] Recently, studies on ECR plasma have been performed for further improvements.

In principle, the state of ECR plasma is determined by physical quantities such as electron density, electron temperature, and ion confinement time. these quantities are controlled by various operation factors; flow rates of ionization and support gases, a set of mirror coil currents, microwave power, RF plunger position, etc. Some experiments using Krypton have been performed to study the effects of those parameters on highly charged ion productions. Transitional and hysteretic behaviors of ECR plasma were observed. The results of the experiments are discussed in this report.

## 2. HyperECR Ion Source

This ion source is a hybrid type ECRIS with an RF frequency of 14 GHz. Figure 1 shows a schematic diagram of the ion source.

It has a couple of normal conducting mirror coils; MC1 for upstream and MC2 for downstream. Sextupole magnet consists of permanent magnets. The plasma chamber is 50 mm in diameter, and 195 mm in length. It has a volume of about 380 $cm^2$. A movable stainless steel rod (RF plunger) can be inserted from upstream to adjust the boundary condition of the RF cavity. Ionization gas and support gas are injected from a gas chamber upstream. The gas pressure inside the plasma chamber is controlled by these needle valves.

14 GHz microwave is generated by a traveling-wave tube amplifier (TWTA) and guided to the plasma chamber through a waveguide. The plasma chamber is floating at an extraction voltage ($V_{ext}$) from the ground. In this experiment $V_{ext}$ is fixed to 15 kV. The extracted beam is focused by passing through an Einzel electrode to which $V_{ein}$ of positive voltage is applied.

There are a doublet of quadrupole magnets and a 90° analyzing magnet downstream of the extraction system.

A beam is tuned by handling six parameters of the ion source and three parameters of the beam transmission system. To optimize beam quantity and quality, operators have to solve this multivariable problem. The most difficult aspect of operating ECRIS is that operational parameters, physical quantities which determine a plasma state, and ob-
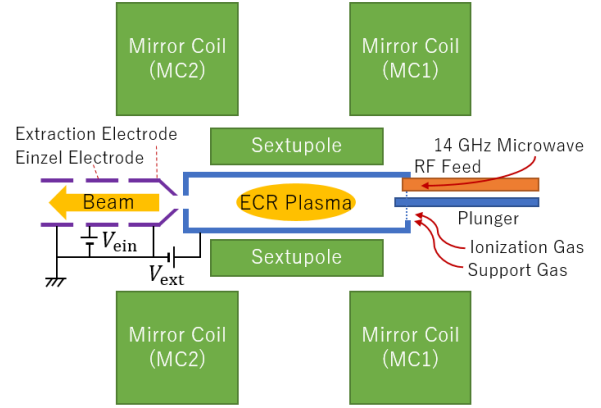


Figure 1. Scematic diagram of Hyper ECR ion source. Magnetic components are shown in green, the extraction system is in purple, geometrical elements affecting RF cavity condition are in blue and the RF feed is in orange.

servable values such as beam current have no one-to-one correspondence. For example, when ionization gas flow is increased, electron density increases and electron temperature decreases.

## 3. ECR Plasma Transitions

Recently, experiments have been performed to study those operating parameters' effects on highly charged heavy ions. Using Kr as an ionization gas and He, Ne, $N_2$ as support gasses, beam current is measured when operating parameters are changed independently. Consequently, transitions of plasma states with hysteresis are observed. Such transitions have occurred during past operations, and systematic data have been acquired by this experiment.

Using $N_2$ as a support gas, every operating parameter is tuned to maximize $^{84}Kr^{7+}$, then the parameters are swept individually while the beam current is measured. Figure 2 shows one example of such experiments. $^{84}Kr^{7+}$ beam current and reflected microwave (RF) power are measured when the RF power input from TWTA is swept back and forth between 100 W and 600 W.

In this case, there appeared to be at least two states of ECR plasma. Transitions occurred when the RF power reached 300 W while raising the power and 166.5 W while lowering it. Meanwhile, the reflected RF power stayed below 15 W.

The plasma state becomes more unstable as the input
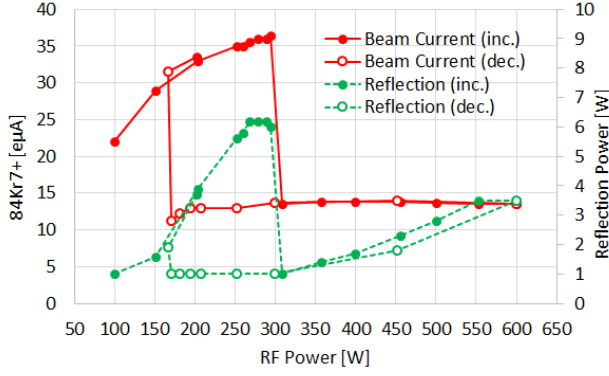
Figure 2. Beam current of $^{84}Kr^{7+}$ and reflected power vs. input RF power. The red solid line indicates the beam current and the green broken line indicates the reflected power. Closed circles are measured when input power is increased, and open circles when it is decreased. The graph shows that reflected microwave power less than 1 W cannot be detected by TWTA, hence is represented as 1 W.

power approaches the critical point, and it takes less time to transition. In this experiment, for example, it took around two minutes for the transition when the input power is set to 285 W and it was completely stable when it is set to 270 W. Operators should keep in mind that there sometimes is a trade-off between the beam intensity and the stability.

Figure 3 shows the charge state distributions (CSDs) measured while the downstream mirror coil (MC2) is swept. There was a plasma state transition at MC2: 542 A. The CSD measured at MC2: 588 A shows how the transition affects each charge state. The shape of the CSD at MC2: 588 A differs from the other two. Low charge states are significantly suppressed.

## 4. Bypassing Transitions

During the experiments regarding the upper mirror coil (MC1), the transition occurred at 555 A when the MC1 current was gradually raised. On the other hand, when it swept up in about 10 seconds from MC1: 530 A to 562 A, the transition was avoided and the plasma was stabilized even



Figure 3. Charge state distributions of Kr beams. Three trends are the results of their measurements when MC2 is set to 400 A (indicated as blue triangles), 500 A (as green circles), and 588 A (as red X-marks), while MC1 is fixed to 526 A.

at the maximum MC1 current of 588 A maximizing $^{84}Kr^{7+}$ beam current.

Another method is discovered during the MC2 experiment. This time plasma transition occurred at MC2: 480 A. $Kr^{7+}$ beam current was about 21 eµA at 500 A. The RF power is lowered from 274 W down to tens of watts, then it is brought back up again at the same power. The plasma state was changed and the beam current was enhanced to 36 eµA.

## 5. Summary

Before this experiment, the understanding of the plasma transition was vague. The experiment gave us more systematic insight into the phenomenon. It has multiple modes and hysteretic behaviors. Also, the time and order of tuning operation parameters may be relevant to maintaining the plasma state. The transition has an individual effect on each charge state. It seems that the externalization of plasma instabilities on certain conditions results in transitions, however, we need further experiments and analyses to discuss its physics.

More details about the plasma transition can be found in the proceedings of the 19th PASJ Meeting held in 2022. [3]

## References

[1] K. Ozeki *et al.*, Proceedings of the 19th PASJ Meeting, MTPF001 (2022).
[2] K. Kamakura *et al.*, CNS Annual Report 2020, 45-46 (2021).
[3] K. Kamakura *et al.*, Proceedings of the 19th PASJ Meeting, THPS035 (2022).

# Theoretical Nuclear Physics

# Eigenvector continuation in nuclear shell-model calculations

Noritaka Shimizu[a,b] and Sota Yoshida[c],

[a]Center for Nuclear Study, Graduate School of Science, The University of Tokyo
[b]Center for Computational Sciences, University of Tsukuba
[c]Liberal and General Education Center, Institute for Promotion of Higher Academic Education, Utsunomiya University

## 1. Introduction

The nuclear shell-model calculation is one of the most powerful tools to discuss various nuclear structures microscopically. In a traditional shell-model framework such as [1, 2], the parameters of the shell-model Hamiltonian are obtained employing the effective-interaction theory and these values are corrected phenomenologically so that the shell-model results well repro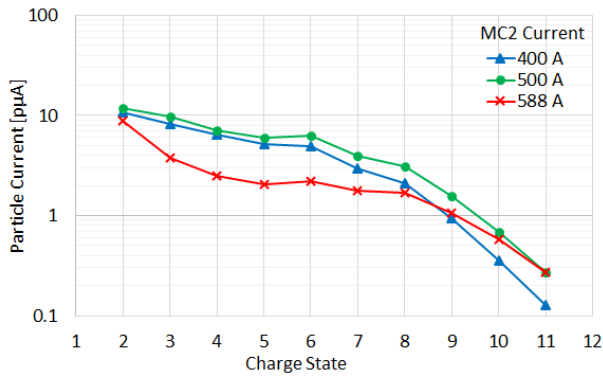duce the experimental binding and excitation energies. For the analysis of the uncertainty caused by this correction [3, 4], we have to perform many shell-model calculations repeatedly by changing these parameters slightly. In such a situation, the eigenvector-continuation (EC) technique [5] is expected to shorten the computation time of these calculations. In this report, we introduce the EC to nuclear shell-model calculations and discuss its performance. This report is condensed from Ref. [6].

## 2. Theoretical Framework

The nuclear shell-model Hamiltonian is defined as

$$H(c) = \sum_i e_i c_i^\dagger c_i + \sum_{i<j,k<l} v_{ijkl} c_i^\dagger c_j^\dagger c_l c_k \qquad (1)$$

where $c_i^\dagger$ is a creation operator of the single-particle state $i$ in the model space. The $e_i$ and $v_{ijkl}$ are parameters, which are determined so that the eigenvalue agrees with the experimental value keeping rotational and isospin symmetries. $c$ denotes a set of the parameters to define $e_i$ and $v_{ijkl}$. The eigenenergy $E(c)$ and the eigenvector $|\phi(c)\rangle$ are given by solving the eigenvalue problem

$$H(c)|\phi(c)\rangle = E(c)|\phi(c)\rangle, \qquad (2)$$

by means of the Lanczos method. However, the dimension of the Hamiltonian matrix is often huge [7], which would prevent us from solving the eigenvalue problem many times by changing the parameters.

Here, we introduce the EC technique to the shell-model calculations to estimate the eigenenergies and related physical observables without performing the diagonalization for each different interaction. In the preparation stage of the EC method, we prepare a set of sample interactions, $H(s)$, which are given randomly. We solve the eigenvalue problems of these sample interactions and obtain the sample eigenvectors $|\phi_s\rangle$ as

$$H(s)|\phi_s\rangle = E_s|\phi_s\rangle. \qquad (3)$$

By using these prepared eigenvectors, the eigenvalue of a target Hamiltonian $H(t)$ is estimated without solving its eigenvalue problem as follows. The eigenvector of $H(t)$ is approximated by solving the generalized eigenvalue problem in the subspace spanned by the sample vectors. It is obtained by

$$\sum_{s'=1}^{N_s} \tilde{H}_{ss'} \tilde{v}_{s'} = \tilde{E}_t \sum_{s'=1}^{N_s} \tilde{N}_{ss'} \tilde{v}_{s'}, \qquad (4)$$

with

$$\begin{aligned} \tilde{H}_{ss'} &= \langle \phi_s | H(\mathbf{t}) | \phi_{s'} \rangle \\ \tilde{N}_{ss'} &= \langle \phi_s | \phi_{s'} \rangle, \end{aligned} \qquad (5)$$

where $\tilde{E}_t$ is the estimated value of the exact eigenvalue of $H(\mathbf{t})$. The dimension of this generalized eigenvalue problem, namely the number of samples $N_s$, is far smaller than the original eigenvalue problem in Eq. (3). The eigenvector of $H(t)$ is also approximated by a linear combination of the sample eigenvectors with the coefficients $\tilde{v}_s$ as

$$|\phi_t\rangle \sim |\tilde{\phi}_t\rangle = \sum_s \tilde{v}_s |\phi_s\rangle, \qquad (6)$$

which is used to estimate other physical quantities.

To perform shell-model calculations and the EC estimation efficiently, one of the authors developed a new shell model code "ShellModel.jl", which is written in the Julia language and is publicly available [8].

## 3. Benchmark Results

Here we present a benchmark result of the EC estimation in shell-model calculations. We take two $sd$-shell nuclei, $^{28}$Si and $^{25}$Mg, with the $sd$-shell model space as examples. In this case, the number of parameters for the shell-model Hamiltonian is 66. The $M$-scheme dimension is 93,710 for $^{28}$Si and 44,133 for $^{25}$Mg.

As a first example, we take the yrast $0^+$, $1^+$, $2^+$, and $3^+$ energies of $^{28}$Si. We prepare 250 sample interactions generated by the sum of the USDB interaction [1] and random numbers with the 1-MeV standard deviation. For validation, we prepare 100 target interactions in the same way and estimate the energies by the EC method employing the sampling results. Figure 1 shows the EC estimated energies against the exact ones of the yrast $J = 0^+, 1^+, 2^+, 3^+$, and $4^+$ states of $^{28}$Si. They agree quite well and its typical error is less than 1%. Note again that the EC estimate requires little additional computations.

As an example of odd nuclei, the energies of $J = 1/2^+, 3/2^+, 5/2^+, 7/2^+$, and $9/2^+$ states of $^{25}$Mg are estimated by the EC method with the same 100 target interactions. Figure 2 shows the EC estimated energies agree quite well with the exact one similarly to Fig. 1.
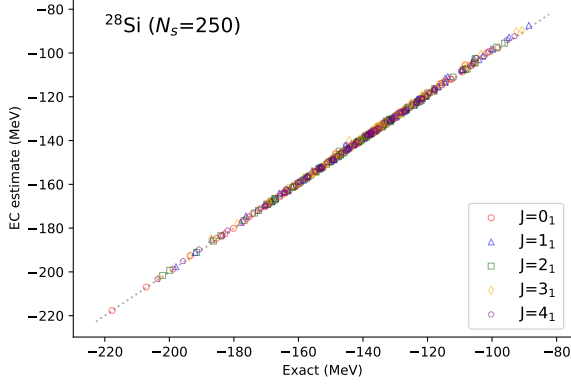
Figure 1. EC estimated energies of the $J = 0^+, 1^+, 2^+, 3^+$, and $4^+$ states of $^{28}$Si against the exact ones. The EC estimation is performed for the 100 different interactions with employing 250 samples. The dotted line shows the ideal agreement. Taken from Ref. [6].
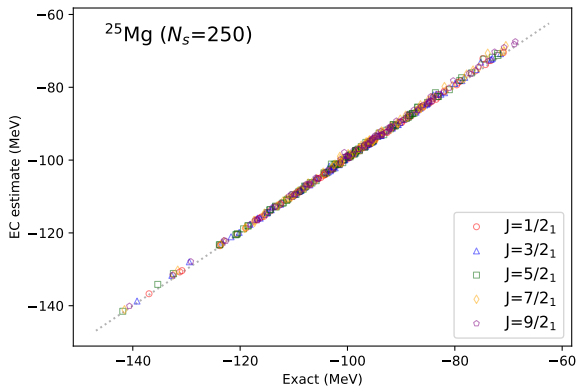


Figure 2. EC estimated energies of the $J = 1/2^+, 3/2^+, 5/2^+,$ $7/2^+$, and $9/2^+$ states of $^{25}$Mg against the exact ones. See the caption of Fig. 1 for details. Taken from Ref. [6].

## 4. Summary

We introduce the EC method to nuclear shell-model calculations and investigate its performance. We demonstrated that the EC estimated energies well reproduce the exact eigenenergies for $sd$-shell nuclei.

The accuracy of the EC estimation concerning quadrupole and magnetic moments and excitation energies is further discussed in Ref. [6]. Moreover, the approximated wave function given by the EC method can be used as an initial vector of the Lanczos iterations, which shortens the number of the iterations [6].

### References

[1] B. A. Brown and W. A. Richter, Phys. Rev. C **74**, 034315 (2006).

[2] M. Honma, T. Otsuka, B. A. Brown and T. Mizusaki, Euro. Phys. J. A **25**, 499 (2005).

[3] S. Yoshida, N. Shimizu, T. Togashi, and T. Otsuka, Phys. Rev. C **98**, 061301(R) (2018).

[4] J. M. R. Fox, C. W. Johnson, and R. N. Perez, Phys. Rev. C **101**, 054308 (2020).

[5] D. Frame, R. He, I. Ipsen, D. Lee, D. Lee, and E. Rrapaj, Phys. Rev. Lett. **121**, 032501 (2018).

[6] S. Yoshida and N. Shimizu, Prog. Theor. Exp. Phys. accepted. https://doi.org/10.1093/ptep/ptac057

[7] N. Shimizu, T. Mizusaki, Y. Utsuno, and Y. Tsunoda, Comp. Phys. Comm. **244**, 372 (2019).

[8] S. Yoshida, code ShellModel.jl (2021), https://github.com/SotaYoshida/ShellModel.jl

# Correlating the nuclear Schiff moment of $^{129}$Xe with the magnetic moment

K. Yanase[a], N. Shimizu[a,b], K. Higashiyama[c], and N. Yoshinaga[d]

[a]*Center for Nuclear Study, The University of Tokyo, Hongo Tokyo 113-0033, Japan*
[b]*Center for Computational Sciences, University of Tsukuba, Tsukuba 305-8577, Japan*
[c]*Department of Physics, Chiba Institute of Technology, Narashino, Chiba 275-0023, Japan*
[d]*Department of Physics, Saitama University, Saitama City 338-8570, Japan*

The charge-parity (*CP*) violation in the fundamental physics is one of the necessary conditions for the matter-antimatter asymmetry in the current universe. The permanent electric dipole moments (EDMs) of elementary and composite particles are promising probes of the *CP* violation beyond the standard model. In particular the EDMs of diamagnetic atoms including $^{129}$Xe are sensitive to the $P$, $T$-odd coupling constants of the hadronic sector through the nuclear Schiff moment (NSM).

As discussed in Ref. [2], the NSM is factorized into the $P$, $T$-odd coupling constants at the nuclear energy scale and their coefficients, $s_N$, $a_T$, and $a_N$, obtained by nuclear many-body calculations as

$$S = S_2 + S_3 \tag{1}$$

$$S_2 = \sum_{N=p,n} s_N d_N, \tag{2}$$

$$S_3 = \sum_{T=0}^{2} a_T g_{\pi NN}^{(T)} + \sum_{N=p,n} a_N d_N, \tag{3}$$

where $d_p$ and $d_n$ are the proton EDM and the neutron EDM, respectively, and $g_{\pi NN}^{(T)}$ denotes the $P$, $T$-odd $\pi NN$ coupling constants with the isospin components $T = 0, 1, 2$. The second-order and third-order contributions are denoted by $S_2$ and $S_3$, respectively. The NSM coefficient $a_T$ induced from the $P$, $T$-odd one-pion-exchange nucleon-nucleon ($\pi NN$) interaction have been computed based on the large-scale shell model [3]. In this report, we evaluate the nucleon EDM contributions $s_N$ and $a_N$ of $^{129}$Xe by using beyond the mean-field approaches.

The second-order NSM operator is defined by

$$S_{2,k} = \frac{1}{6} \sum_{a=1}^{A} d_{a,k} \left( r_a^2 - \langle r^2 \rangle_{\text{ch}} \right)$$
$$+ \frac{2}{15} \sum_{a=1}^{A} \sum_{j} d_{a,j} \left( Q_{a,jk} - \langle Q_{jk} \rangle_{\text{ch}} \right), \tag{4}$$

where $d_{a,k} = d_p \sigma_k$ for proton, $d_{a,k} = d_n \sigma_k$ for neutron, $\sigma_k$ is the spin Pauli matrix, and $Q_{a,jk}$ is the nuclear quadrupole moment. The cartesian components are denoted by $j$ and $k$. The second-order contribution is computed by

$$S_2 = \left\langle \psi_{\text{g.s.}}^{(N)} \middle| S_{2z} \middle| \psi_{\text{g.s.}}^{(N)} \right\rangle. \tag{5}$$

Here, $\left| \psi_{\text{g.s.}}^{(N)} \right\rangle$ represents the nuclear ground state where the $P$, $T$ symmetries are not violated. In contrast, the third-order processes involve the $P$, $T$ violations inside the nu-cleus. The third-order NSM is given by the $P$, $T$-odd operator

$$\boldsymbol{S}_3 = \frac{e}{10} \sum_{a=1}^{Z} \left[ r_a^2 \boldsymbol{r}_a - \frac{5}{3} \boldsymbol{r}_a \langle r^2 \rangle_{\text{ch}} - \frac{4}{3} \boldsymbol{r}_a \langle Q_{jk} \rangle_{\text{ch}} \right], \tag{6}$$

and the expectation value is calculated perturbatively as

$$S_3 = \sum_n \frac{1}{E_{\text{g.s.}}^{(N)} - E_n^{(N)}}$$
$$\times \left\langle \psi_{\text{g.s.}}^{(N)} \middle| S_{3z} \middle| \psi_n^{(N)} \right\rangle \left\langle \psi_n^{(N)} \middle| \widetilde{V} \middle| \psi_{\text{g.s.}}^{(N)} \right\rangle$$
$$+ c.c. \tag{7}$$

where $\widetilde{V}$ denotes the $P$, $T$-odd $NN$ interactions including the $P$, $T$-odd $\pi NN$ interactions and the nucleon EDM interactions with protons.

We apply large-scale shell-model (LSSM) calculations performed in Ref. [3] to compute $s_N$ and $a_N$. We utilize the KSHELL code [4] and the effective interactions SNV and SN100PN for the LSSM calculations. Recent studies of nuclear spectroscopy using the LSSM calculations with those realistic interactions have shown the good agreements of low-energy spectra with experiment in a specific area of the nuclear chart.

The LSSM calculations also reproduce experimental data of the magnetic moment by adopting the quenching factor 0.7 for the spin $g$-factor. This effective operator is attributed to the two-body current correction and the core polarization. The LSSM calculations of $^{129}$Xe employs the standard model space between the magic numbers 50 and 82, and lack the particle-hole configurations such as $(0g_{9/2}^{-1}, 0g_{7/2})$ and $(0h_{11/2}^{-1}, 0h_{9/2})$, which play a crucial role for this quenching [5]. The spin dependence of the second-order NSM operator in Eq. (4) indicates that its one-body matrix elements between the spin-orbit partners are significant similarly to the magnetic moment. We then perform the quasi-particle vacua shell model (QVSM) calculations for the extended model space to include the $0g_{9/2}$ and the $0h_{9/2}$ orbitals. The framework of the QVSM calculation is detailed in Ref. [6].

For the QVSM calculations, we adopt phenomenological extensions of the SNV effective interaction to the full *sdgh* shell. The SNV effective interaction is employed for the standard model space and the extended part is given by the VMU interaction. This interaction is referred to as SNV-*sdgh*. Another set consists of the SNV, JUN45, and Kuo-Herling interactions, and the remaining proton-neutron part is given by the VMU interaction. To com-

pensate the enhancement of the pairing correlation by extending the model space, we reduce the pairing interaction strengths between like nucleons. The reduction factors are determined by low-energy spectra of $^{134}$Sn and $^{134}$Te as 0.72 for proton and 0.76 for neutron in the SNV-*sdgh* interaction and 0.74 for proton and 0.76 for neutron in the SNJKV interaction.

The second-order NSM coefficients $s_N$ of $^{129}$Xe have been investigated by using the pair-truncated shell model (PTSM), where many-body configurations are made of building blocks composed of nucleon pairs with specific angular momenta. It reduces the dimension of the many-body Hamiltonian matrix to be diagonalized by orders of magnitude. The PTSM calculation of $s_N$ was originally performed in Ref. [7]. They employed the phenomenological monopole and quadrupole pairing plus quadrupole-quadrupole interaction as the effective interaction. The interaction strengths are optimized for low-energy spectra of Xe, Ba, Ce, and Nd isotopes close to the neutron magic number. This effective interaction is referred to as HY04 in this letter. Another parameter set of the effective interactions (HY11) was also applied to compute the NSM coefficients [8, 9]. This revision was for the better reproduction of odd-mass nuclei.

We revisit the PTSM calculations with some corrections for comparison. In this report, we adopt the standard formula $\hbar\omega = 41A^{-1/3}$ (MeV) for the harmonic oscillator frequency to evaluate the one-body matrix elements as well as in the LSSM and the QVSM calculations. This choice corresponds to the root-mean-square charge radius 4.6 fm of $^{129}$Xe, which is consistent with the experimental value 4.8 fm [10]. On the other hand, an incorrect value of $\hbar\omega = 41$ MeV was adopted and the charge radius was severely underestimated in Ref. [8]. Another modification is concerned with the model space. The original study adopted an extended model space for proton [9], but the influence is negligible. We employ the standard model space for the consistency with the LSSM calculations.

Figure 1 shows the possible relation between $s_n$ and the magnetic moment of $^{129}$Xe. This correlation is understood by considering the fictitious state

$$\bigl|\psi\bigr\rangle = \alpha\bigl|\psi_{\text{g.s.}}\bigr\rangle + \sqrt{1-\alpha^2}\bigl|\psi_{\text{exc.}}\bigr\rangle, \tag{8}$$

where $\bigl|\psi_{\text{g.s.}}\bigr\rangle$ and $\bigl|\psi_{\text{exc.}}\bigr\rangle$ denote the ideal ground state and the second lowest $\frac{1}{2}^+$ state. If a nuclear model calculation represents well the ground state as $\alpha \simeq 1$, the result should be plotted on the upper-left in Fig. 1 corresponding to the experimental value of the magnetic moment. However, the result approaches the predicted values of the second lowest $\frac{1}{2}^+$ state as $\alpha$ becomes close to zero. This picture can explain the significant quenching in the PTSM calculations.

Using the correlation described in Fig. 1, the theoretical uncertainty of the NSM coefficient $s_n$ can be suppressed. Even though the PTSM is counted with the equal weight, we obtain $s_n = 0.29 \pm 0.10\,\text{fm}^2$, which support the LSSM and the QVSM calculations. We note that the third-order contribution $a_n$ does not disturb this correlation. Our LSSM calculation with the SNV effective interaction gives $a_n = 0.053\,\text{fm}^2$ and $a_p = -0.001\,\text{fm}^2$ for $^{129}$Xe.

In summary, we have computed the nucleon EDM induced NSM coefficients of $^{129}$Xe in the nuclear shell model. We found the clear correlation between $s_n$ and the magnetic moment, which allows us to significantly reduce the uncertainty of $s_n$. In fact the experimental value of the magnetic moment is well reproduced in the LSSM calculations. We have also performed the QVSM calculations to evaluate the influence of the $0g_{9/2}$ and $0h_{9/2}$ orbitals strongly connected with the standard model space by the second-order NSM operator. The corrections from this extension of the model space and the third-order contribution $a_n$ do not disturb the useful correlation.

## References

[1] L. I. Schiff, Phys. Rev. **132** (1963) 2194.

[2] K. Yanase, Phys. Rev. C **103** (2021) 035501.

[3] K. Yanase and N. Shimizu, Phys. Rev. C **102** (2020) 065502.

[4] N. Shimizu, T. Mizusaki, Y. Utsuno, and Y. Tsunoda, Comput. Phys. Commun. **244** (2019) 372.

[5] B. A. Brown, N. J. Stone, J. R. Stone, I. S. Towner, and M. Hjorth-Jensen, Phys. Rev. C **71** (2005) 044317.

[6] N. Shimizu, Y. Tsunoda, Y. Utsuno, T. Otsuka, Phys. Rev. C **103** (2021) 014312.

[7] N. Yoshinaga, K. Higashiyama, and R. Arai, Prog. Theor. Phys. **124** (2010) 1115.

[8] K. Higashiyama and N. Yoshinaga, Phys. Rev. C **83** (2011) 034321.

[9] N. Yoshinaga and K. Higashiyama and R. Arai and E. Teruya, Phys. Rev. C **87** (2013) 044332.

[10] I. Angeli and K. P. Marinova, Atomic Data and Nuclear Data Tables **99** (2013) 69.
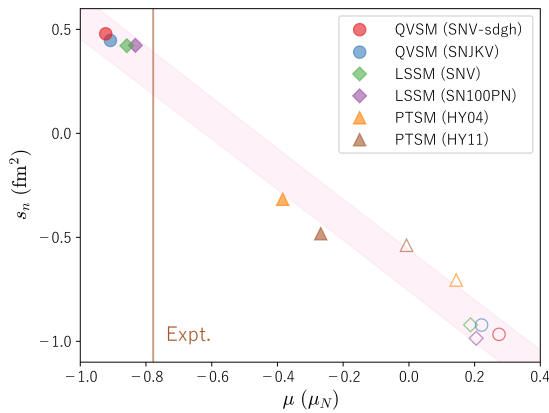
Figure 1. The magnetic moment and the second-order NSM of $^{129}$Xe. The filled symbols and the open symbols represent the ground state and the $\frac{1}{2}^+_2$ state, respectively.

# Other Activities

# The 20th CNS International Summer School CNSSS21

N. Aoi[a], T. Gunji, N. Imai, H. Liang[b,c], S. Michimasa, H. Nagahama, S. Ota, T. Otsuka[b],
H. Sakai[b], Y. Sakemi, H. Sakurai[b,c], N. Shimizu, S. Shimoura, H. Ueno[b], T. Uesaka[b], Y. Utsuno[d],
T. Wakasa[e], K. Yako, H. Yamaguchi, K. Yoneda

*Center for Nuclear Study, Graduate School of Science, University of Tokyo*
*[a]RCNP, Osaka University*
*[b]RIKEN Nishina Center*
*[c]Department of Physics, Univ. of Tokyo*
*[d]Advanced Science Research Center, Japan Atomic Energy Agency*
*[e]Super Heavy Element Center, Kyushu University*

The 20th CNS International Summer School (CNSSS21) was hosted by Center for Nuclear Study (CNS) from 16th to 20th in August, 2021. The school was co-organized by JSPS A3-Foresight program and Super Heavy Element Center, Kyushu University. The school was also supported by RIKEN Nishina Center and Asian Nuclear Physics Association (ANPhA).

Because of the COVID-19 pandemic, the school was held only on-line like the A3F-CNSSS20. The summer school was the twentieth one in the series which aimed at fostering graduate students and postdocs by providing basic knowledge and perspectives of nuclear physics. It consisted of lectures by leading scientists in the fields of both experimental and theoretical nuclear physics. Each lecture started with an introductory talk from the fundamental point of view and ended with up-to-date topics in the relevant field.

The list of the lecturers and the title of lectures are following:

- Dr. Stefan Typel (GSI, Germany), "From nuclei to starts with a relativistic density functional"
- Prof. Hidetoshi Yamaguchi (CNS, U. of Tokyo, Japan), "How to study nuclear clusters experimenally"
- Prof. Peter Mueller (ANL, USA), "Atom Traps of Rare Isotopes at the Precision and Sensitivity Frontier in Nuclear Physics"
- Prof. Akira Ejiri (U. of Tokyo, Japan), " R&D for nuclear fusion reactors, High temperature plasma as a complex system"
- Dr. Zaihong Yang (RCNP, Osaka University, Japan) "Probing nuclear clustering with knockout reactions"
- Dr. Sarah Naimi (RIKEN Nishina Center, Japan) "Overview of RIBF"
- Prof. Susumu Shimoura (CNS, U. of Tokyo, Japan) "Direct reactions as quantum probes of sub-atomic system"

One of the motivations of the summer school is to enhance the mutual understanding among the participants in different counties. Because the school was held on-line, there are less chance to comunicate. We organized the after-school session for the first time where the participants introduced their own laboratories.
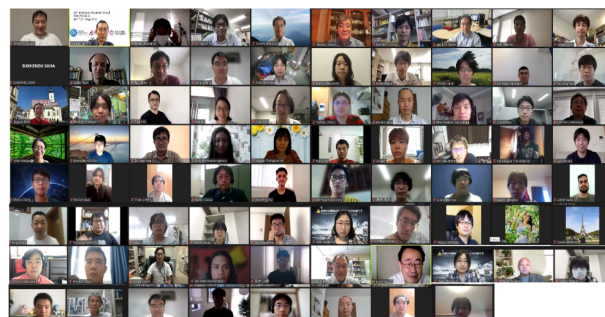


Figure 1. A group photos of the participants of CNSSS21 with the lecturers.

Seven lecturers and 173 participants registered at the school. Because the school was held on-line, participants joined not only from Japan, Korea, China and Vietnam but also from India, Malaysia and Norway. The time of each class was 50 minutes. There was 10 minutes break between the classes. The actual average number of participants is around 130. Figure 1 is a group photo of all the participants with the lecturers.

As traditional, there were four "Young Scientist Sessions", where oral and poster presentations were given by graduate students and postdocs. There were twenty-one oral presentations and nine poster presentations. Since 2017, we have the CNSSS young scientist awards (CNSSSYS awards) for the good presentations. A few winners were selected from each young scientist session by the members of organizing committee and the lecturers. The winners of the third CNSSSYS award were;

- Mr. Naoto Hasegawa (Tohoku University) "Time-Dependent Generator Coordinate Method for many-particle tunneling"
- Mr. Tin Gao (The University of HongKong) " In-beam $\hat{I}^3$-ray Spectroscopy of $^{97}$Cd"
- Ms. Moemi Matsumoto (Tohoku University) "Visualization of nuclear cluster correlation with microscopic wave function

The certificate of the awards were presented to them from the school master, Prof. Shimoura.

The best presenter among them, Mr. Moemi Matsumoto, was also awarded the APPS-DNP/ANPhA prize for young physicist, which was sponsered by AAPPS-DNP/ANPhA.

He received the certificate as well as the prize money as prestend from Prof. W. Liu, the chair of ANPhA.

# Laboratory Exercise for Undergraduate Students

H. Nagahama, K. Yako, M. Niikura[a], M. Fukase, K. Okawa, M. Michimasa, N. Imai, H. Yamaguchi,
H. Sakurai[a,b] and S. Shimoura

*Center for Nuclear Study, Graduate School of Science, University of Tokyo*
[a]*Department of Physics, University of Tokyo*
[b] *RIKEN Nishina Center*

Nuclear scattering experiments were performed as a laboratory exercise for undergraduate students of the University of Tokyo. This program was aiming at providing undergraduate students with an opportunity to learn how to study subatomic physics by using an ion beam from an accelerator. In 2021, 32 students attended this program.

Four beam times were scheduled in the second semester for third-year students, and 8 students participated in each beam time. The experiments were performed at the RIBF using a 26-MeV alpha beam accelerated by the AVF cyclotron. The alpha beam extracted from the AVF cyclotron was transported to the E7B beam line in the E7 experimental hall. The scattering chamber has two separate target ports which enable us to perform two independent experiments without opening the chamber during the beam time. In each beam time, the students were divided into two groups and took one of the following two subjects:

1. Measurement of elastic scattering of incident alpha particle with $^{197}$Au, to learn how to determine nuclear size.

2. Measurement of gamma rays emitted from the cascade decay of highly excited $^{154}$Gd and $^{184}$Os, to learn the nuclear deformation.

Before the experiment, the students took a course on the basic handling of the semiconductor detectors and electronic circuits at the Hongo campus, and attended a radiation safety lecture at RIKEN. CNS conducted tours to the RI beam factory for the students.

In the $\alpha + ^{197}$Au measurement, $\alpha$ particles scattered with the Au target with a thickness of 1 $\mu$m were detected using a silicon PIN-diode located 15-cm away from the target. A collimator with a diameter of 6 mm was attached on the silicon detector. The energy spectrum of the scattered $\alpha$ particles was recorded by a multi-channel analyzer (MCA) system. The beam was stopped by a Faraday cup located downstream of the scattering chamber. The cross section for the alpha elastic scattering was measured in the angular range of $\theta_{\text{lab}} = 20 - 150°$.

The measured cross section was compared with the calculated cross section of the Rutherford scattering. The cross section was also analyzed by the potential model calculation, and the radius of the $^{197}$Au nucleus was discussed. Some students obtained the radius of $\sim 10$ fm by using a classical model where the trajectory of the $\alpha$ particle in the nuclear potential is obtained using the Runge-Kutta method. Others tried to understand the scattering process by calculating the angular distribution using the distorted wave Born approximation method with a Coulomb wave function and a realistic nuclear potential.

In the measurement of gamma rays, excited states in $^{154}$Gd and $^{184}$Os nuclei were populated by the $^{152}$Sm($\alpha$,2n) and $^{182}$W($\alpha$,2n) reactions, respectively. The gamma rays emitted from the cascade decay of the rotational bands were measured by a high-purity germanium detector located 30-cm away from the target. The energy of the gamma ray were recorded by the MCA system. The gain and the efficiency of the detector system had been calibrated using standard gamma-ray sources of $^{60}$Co, $^{133}$Ba, and $^{137}$Cs. The gamma rays from the $10^+$ and $8^+$ states in $^{154}$Gd and $^{184}$Os, respectively, were successfully identified. Based on the energies of the gamma rays, the moment of inertia and the deformation parameters of the excited states were discussed by using a classical rigid rotor model and a irrotational fluid model. The students found that the reality lies between the two extreme models. The initial population among the levels in the rotational band was also discussed by taking the effect of the internal conversion into account.

It was the first time for most of the students to use large experimental equipments. They learned basic things about the experimental nuclear physics and how to extract physics from the data. We believe this program was very impressive for the students. The authors would like to thank Dr. K. Tanaka, the CNS accelerator group, and the RIBF cyclotron crew for their helpful effort in the present program.

# Appendices

**Symposium, Workshop, Seminar, and PAC**
**CNS Reports**
**Publication List**
**Talks and Presentations**
**Awards, Press Releases, and Others**
**Personnel**

# Symposium, Workshop, Seminar, and PAC

**A. Symposium and Workshop**

None

**B. CNS Seminar**

1.  CNS + RIBF NP Seminar #295 (Prof. Otsuka)
    Date: November 5, 2021

**C. Program Advisory Committee for Nuclear-Physics Experiments at RI Beam Factory**

1.  The 22nd NP-PAC meeting
    Date: December 1-3, 2021
    Online meeting via zoom

# CNS Reports

**#100** "CNS Annual Report 2020"
Edited by H. Nagahama
March, 2022

# Publication List

## A. Original Papers

1. S. Go, E. Ideguchi, R. Yokoyama, N. Aoi, F. Azaiez, K. Furutaka, Y. Hatsukawa, A. Kimura, K. Kisamori, M. Kobayashi, F. Kitatani, M. Koizumi, H. Harada, I. Matea, S. Michimasa, H. Miya, S. Nakamura, M. Niikura, H. Nishibata, N. Shimizu, S. Shimoura, T. Shizuma, M. Sugawara, D. Suzuki, M. Takaki, Y. Toh, Y. Utsuno, D. Verney, A. Yagi, "High-spin states in $^{35}$S", Phys. Rev. C **103**, 034327 (2021)

2. H. Baba, T. Ichihara, T. Isobe, T. Ohnishi, K. Yoshida, Y. Watanabe, S. Ota, H. Shimizu, S. Shimoura, S. Takeuchi, D. Nishimura, J. Zenihiro, A.O. Tokiyasu, R. Yokoyama, "MPV-Parallel Readout Architecture for the VME Data Acquisition System", IEEE Trans. Nucl. Sci. **68**, 1841–1848 (2021)

3. R. Nakamoto, M. Ito, A. Saito, S. Shimoura, "Extended Migdal-Watson formula to evaluate background strength in binary breakup reactions", Phys. Rev. C **104**, 034602 (2021)

4. N. Kitamura, N. Imai, H. Haba, S. Michimasa, S. Shimoura, Y. Yamaguchi, "Production of $^{178}$Hf$^{m2}$ and a simple chemical separation method for Hf recovery", J. Rad. Nucl. Chem. **330**, 721–725 (2021)

5. S.W. Huang, Z.H. Yang, F.M. Marqués, N.L. Achouri, D.S. Ahn, T. Aumann, H. Baba, D. Beaumel, M. Böhmer, K. Boretzky, M. Caamaño, S. Chen, N. Chiga, M.L. Cortés, D. Cortina, P. Doornenbal, CA. Douma, F. Dufter, J. Feng, B. Fernandez-dominguez, Z. Elekes, U. Forsberg, T. Fujino, N. Fukuda, I. Gašparić, Z. Ge, R. Gernhäuser, J.M. Gheller, J. Gibelin, A. Gillibert, Z. Halász, T. Harada, M.N. Harakeh, A. Hirayama, N. Inabe, T. Isobe, J. Kahlbow, N. Kalantar-Nayestanaki, D. Kim, S. Kim, S. Kiyotake, T. Kobayashi, Y. Kondo, P. Koseoglou, Y. Kubota, I. Kuti, C. Lehr, C. Lenain, P.J. Li, Y. Liu, Y. Maeda, S. Masuoka, M. Matsumoto, A. Matta, J. Mayer, H. Miki, M. Miwa, B. Monteagudo, I. Murray, T. Nakamura, A. Obertelli, N.A. Orr, H. Otsu, V. Panin, S. Park, M. Parlog, S. Paschalis, M. Potlog, S. Reichert, A. Revel, D. Rossi, A. Saito, M. Sasano, H. Sato, H. Scheit, F. Schindler, T. Shimada, Y. Shimizu, S. Shimoura, H. Simon, I. Stefan, S. Storck, L. Stuhl, H. Suzuki, D. Symochko, H. Takeda, S. Takeuchi, J. Tanaka, Y. Togano, T. Tomai, H.T. Törnqvist, E. Tronchin, J. Tscheuschner, T. Uesaka, V. Wagner, K. Wimmer, H. Yamada, B. Yang, L. Yang, Y. Yasuda, K. Yoneda, L. Zanetti, J. Zenihiro, "Experimental Study of $^{4}n$ by Directly Detecting the Decay Neutrons", Few-Body Systems **62**, 102 (2021)

6. R. Nakamoto, M. Ito, A. Saito, S. Shimoura, "Continuum Strength of Direct Breakup Induced by External Isoscalar Field", Few-Body Systems **62**, 107 (2021)

7. W. Horiuchi, T. Inakura, S. Michimasa, "Large enhancement of total reaction cross sections at the edge of the island of inversion in Ti, Cr, and Fe isotopes" Phys. Rev. C **105**, 014316 (2022)

8. R. Yokoyama, E. Ideguchi, G.S. Simpson, Mn. Tanaka, Y. Sun, Cui-Juan Lv, Yan-Xin Liu, Long-Jun Wang, S. Nishimura, P. Doornenbal, G. Lorusso, P.A. Soderstrom, T. Sumikama, J. Wu, Z.Y. Xu, N. Aoi, H. Baba, F.L.B. Garrote, G. Benzoni, F. Browne, R. Daido, Y. Fang, N. Fukuda, A. Gottardo, G. Gey, S. Go, S. Inabe, T. Isobe, D. Kameda, K. Kobayashi, M. Kobayashi, I. Kojouharov, T. Komatsubara, T. Kubo, N. Kurz, I. Kuti, Z. Li, M. Matsushita, S. Michimasa, C.B. Moon, H. Nishibata, I. Nishizuka, A. Odahara, Z. Patel, S. Rice, E. Sahin, H. Sakurai, H. Schaffner, L. Sinclair, H. Suzuki, H. Takeda, J. Taprogge, Z. Vajta, H. Watanabe, A. Yagi, "Three-quasiparticle isomers in odd-even (159)'Pm-161: Calling for modified spin-orbit interaction for the neutron-rich region" Phys. Rev. C **104**, L021303 (2021)

9. R.D. Harding, A.N. Andreyev, A.E. Barzakh, J. G. Cubiss1, P. Van Duppen, M. Al Monthery, N.A. Althubiti, B. Andel, S. Antalic, T.E. Cocolios, T. Day Goodacre, K. Dockx, G. J. Farooq-Smith, D.V. Fedorov, V. N. Fedosseev, D. A. Fink, L. P. Gaffney, L. Ghys, J. D. Johnson, D. T. Joss, M. Huyse, N. Imai, K. M. Lynch, B. A. Marsh, Y. Martinez Palenzuel, P. L. Molkanov, G. G. O'Neill, R. D. Page, R. E. Rossel, S. Rothe, M. D. Seliverstov, S. Sels, C. Van Beveren, and E. Verstraelen, "Laser-assisted nuclear decay spectroscopy of $^{176,177,179}$Au, Phys. Rev. C **104**, 024326 (2022),

10. N. Kitamura, K. Wimmer, T. Miyagi, A. Poves, N. Shimizu, J. A. Tostevin, V. M. Bader, C. Bancroft, D. Barofsky, T. Baugher, D. Bazin, J. S. Berryman, V. Bildstein, A. Gade, N. Imai, T. Kröll, C. Langer, J. Lloyd, E. Lunderberg, F. Nowacki, G. Perdikakis, F. Recchia, T. Redpath, S. Saenz, D. Smalley, S.R. Stroberg, Y. Utsuno, D. Weisshaar, A. Westerberg, "In-beam $\gamma$-ray spectroscopy of $^{32}$Mg via direct reactions", Phys. Rev. C **105** 034318 (2022).

11. A. Fernández, A. Jungclaus, P. Doornenbal, M.A. Bentley, S.M. Lenzi, D. Rudolph, F. Browne, M.L. Cortés, T. Koi-wai, R. Taniuchi, V. Vaquero, K. Wimmer, T. Arici, N. Imai, N. Kitamura, B. Longfellow, R. Lozeva, B. Mauss, D.R. Napoli, M. Niikura, X. Pereira-Lopez, S Pigliapoco, A. Poves, F. Recchia, P. Ruotsalainen, H. Sakurai, S. Uthayakumaar, R. Wadsworth, R. Yajzey, "Mirror energy differences above the 0f(7/2) shell: First gamma-ray spectroscopy of the T-z =-2 nucleus Zn-56", Physics Letters **823** 136784 (2021).

12. S. Hayakawa, M. La Cognata, L. Lamia, H. Yamaguchi, D. Kahl, K. Abe, H. Shimizu, L. Yang, O. Beliuskina, S. M. Cha, K. Y. Chae, S. Cherubini, P. Figuera, Z. Ge, M. Gulino, J. Hu, A. Inoue, N. Iwasa, A. Kim, D. Kim, G. Kiss, S. Kubono, M. La Commara, M. Lattuada, E. J. Lee, J. Y. Moon, S. Palmerini, C. Parascandolo, S. Y. Park, V. H. Phong, D. Pierroutsakou, R. G. Pizzone, G. G. Rapisarda, S. Romano, C. Spitaleri, X. D. Tang, O. Trippella, A. Tumino, and N. T. Zhang, "Constraining the Primordial Lithium Abundance: New Cross Section Measurement of the $^7$Be$+n$ Reactions Updates the Total $^7$Be Destruction Rate", Astrophys. J. Lett. **915**, L13 (2021).

13. S. Palmerini, M. La Cognata, F. Hammache, L. Acosta, R. Alba, V. Burjan, E. Chávez, S. Cherubini, A. Cvetinovic, G. D'Agata, N. de Séréville, A. Di Pietro, P. Figuera, Z. Fülöp, K. Gaitán De Los Rios, G. L. Guardo, M. Gulino, S. Hayakawa, G. G. Kiss, M. La Commara, L. Lamia, C. Maiolino, G. Manicó, C. Matei, M. Mazzocco, J. Mrazek, T. Parascandolo, T. Petruse, D. Pierroutsakou, R. G. Pizzone, G. G. Rapisarda, S. Romano, D. Santonocito, M. L. Sergi, R. Sparta, A. Tumino, H. Yamaguchi, "The $^{27}$Al$(p,\alpha)^{24}$Mg reaction at astrophysical energies studied by means of the trojan horse method applied to the $^2$H($^{27}$Al, $\alpha$ $^{24}$Mg)$n$ reaction", The European Physical Journal Plus **136**, 898 (2021).

14. J. Hu, H. Yamaguchi, Y. H. Lam, A. Heger, D. Kahl, A. M. Jacobs, Z. Johnston, S. W. Xu, N. T. Zhang, S. B. Ma, L. H. Ru, E. Q. Liu, T. Liu, S. Hayakawa, L. Yang, H. Shimizu, C. B. Hamill, A. St J. Murphy, J. Su, X. Fang, K. Y. Chae, M. S. Kwag, S. M. Cha, N. N. Duy, N. K. Uyen, D. H. Kim, R. G. Pizzone, M. La Cognata, S. Cherubini, S. Romano, A. Tumino, J. Liang, A. Psaltis, M. Sferrazza, D. Kim, Y. Y. Li, and S. Kubono, "Advancement of photospheric radius expansion and clocked type-I x-ray burst models with the new $^{22}$Mg($\alpha$, $p$)$^{25}$Al reaction rate determined at the Gamow energy", Phys Rev. Lett. **127**, 172701 (2021).

15. G. G. Kiss, M. La Cognata, R. Yarmukhamedov, K. I. Tursunmakhatov, I. Wiedenhöver, L. T. Baby, S. Cherubini, A. Cvetinović, G. D'Agata, P. Figuera, G. L. Guardo, M. Gulino, S. Hayakawa, I. In- delicato, L. Lamia, M. Lattuada, F. Mudò, S. Palmerini, R. G. Pizzone, G. G. Rapisarda, S. Ro- mano, M. L. Sergi, R. Spartà, C. Spitaleri, O. Trippella, A. Tumino, M. Anastasiou, S. A. Kuvin, N. Rijal, B. Schmidt, S. B. Igamov, S. B. Sakuta, Zs. Fülöp, Gs. Gyürky, T. Szücs, Z. Halász, E. Somorjai, Z. Hons, J. Mrázek, R. E. Tribble, and A. M. Mukhamedzhanov, "Indirect determination of the astrophysical S factor for the $^6$Li(p,$\gamma$)$^7$Be reaction using the asymptotic normalization coefficient method ", Phys. Rev. C, **104**, 015807, (2021).

16. U. A. Acharya *et al.* [PHENIX], "Transverse-single-spin asymmetries of charged pions at midrapidity in trans-versely polarized $p+p$ collisions at $\sqrt{s} = 200$ GeV," Phys. Rev. D **105**, no.3, 032003 (2022).

17. S. Acharya *et al.* [ALICE], "Production of light (anti)nuclei in pp collisions at $\sqrt{s} = 5.02$ TeV," Eur. Phys. J. C **82**, no.4, 289 (2022).

18. S. Acharya *et al.* [ALICE], "Observation of a multiplicity dependence in the pT-differential charm baryon-to-meson ratios in proton–proton collisions at s=13 TeV," Phys. Lett. B **829**, 137065 (2022).

19. S. Acharya *et al.* [ALICE], "Investigating charm production and fragmentation via azimuthal correlations of prompt D mesons with charged particles in pp collisions at $\sqrt{s} = 13$ TeV," Eur. Phys. J. C **82**, no.4, 335 (2022).

20. S. Acharya *et al.* [ALICE], "Measurement of prompt $D_s^+$-meson production and azimuthal anisotropy in Pb–Pb collisions at $\sqrt{s_{NN}}$=5.02TeV," Phys. Lett. B **827**, 136986 (2022).

21. S. Acharya *et al.* [ALICE], "Prompt D$^0$, D$^+$, and D$^{*+}$ production in Pb–Pb collisions at $\sqrt{s_{NN}} = 5.02$ TeV," JHEP **01**, 174 (2022).

22. U. A. Acharya *et al.* [PHENIX], "Transverse single spin asymmetries of forward neutrons in $p + p$, $p$+Al and $p$+Au collisions at $\sqrt{s_{NN}} = 200$ GeV as a function of transverse and longitudinal momenta," Phys. Rev. D **105**, no.3, 032004 (2022).

23. S. Acharya *et al.* [ALICE], "Measurement of inclusive charged-particle b-jet production in pp and p-Pb collisions at $\sqrt{s_{NN}} = 5.02$ TeV," JHEP **01**, 178 (2022).

24. S. Acharya *et al.* [ALICE], "Production of light (anti)nuclei in pp collisions at $\sqrt{s} = 13$ TeV," JHEP **01**, 106 (2022).

25. S. Acharya *et al.* [ALICE], "Prompt and non-prompt J/$\psi$ production cross sections at midrapidity in proton-proton collisions at $\sqrt{s}$ = 5.02 and 13 TeV," JHEP **03**, 190 (2022).

26. S. Acharya *et al.* [ALICE], "Inclusive J/$\psi$ production at midrapidity in pp collisions at $\sqrt{s}$ = 13 TeV," Eur. Phys. J. C **81**, no.12, 1121 (2021).

27. S. Acharya *et al.* [A Large Ion Collider Experiment and ALICE], "Measurement of the groomed jet radius and momentum splitting fraction in pp and Pb−Pb collisions at $\sqrt{s_{NN}}$ = 5.02 TeV," Phys. Rev. Lett. **128**, no.10, 102001 (2022).

28. S. Acharya *et al.* [ALICE], "Measurements of the groomed and ungroomed jet angularities in pp collisions at $\sqrt{s}$ = 5.02 TeV," JHEP **05**, 061 (2022).

29. S. Acharya *et al.* [ALICE], "Polarization of $\Lambda$ and $\bar{\Lambda}$ Hyperons along the Beam Direction in Pb-Pb Collisions at $\sqrt{s_{NN}}$=5.02 TeV," Phys. Rev. Lett. **128**, no.17, 172005 (2022).

30. S. Acharya *et al.* [ALICE], "K$_S^0$- and (anti-)$\Lambda$-hadron correlations in pp collisions at $\sqrt{s}$ = 13 TeV," Eur. Phys. J. C **81**, no.10, 945 (2021).

31. S. Acharya *et al.* [ALICE], "Anisotropic flow of identified hadrons in Xe-Xe collisions at $\sqrt{s_{NN}}$ = 5.44 TeV," JHEP **10**, 152 (2021).

32. U. A. Acharya *et al.* [PHENIX], "Kinematic dependence of azimuthal anisotropies in $p+Au$, $d+Au$, and $^3He+Au$ at $\sqrt{s_{NN}}$ = 200 GeV," Phys. Rev. C **105**, no.2, 024901 (2022).

33. S. Acharya *et al.* [ALICE], "Direct observation of the dead-cone effect in quantum chromodynamics," Nature **605**, no.7910, 440-446 (2022).

34. S. Acharya *et al.* [ALICE], "Measurement of Prompt D$^0$, $\Lambda_c^+$, and $\Sigma_c^{0,++}$(2455) Production in Proton–Proton Collisions at $\sqrt{s}$ = 13 TeV," Phys. Rev. Lett. **128**, no.1, 012001 (2022).

35. S. Acharya *et al.* [ALICE], "Charm-quark fragmentation fractions and production cross section at midrapidity in pp collisions at the LHC," Phys. Rev. D **105**, no.1, L011103 (2022).

36. S. Acharya *et al.* [ALICE], "Measurement of the production cross section of prompt $\Xi_c^0$ baryons at midrapidity in pp collisions at $\sqrt{s}$ = 5.02 TeV," JHEP **10**, 159 (2021).

37. S. Acharya *et al.* [ALICE], "Experimental Evidence for an Attractive p-$\phi$ Interaction," Phys. Rev. Lett. **127**, no.17, 172301 (2021).

38. S. Acharya *et al.* [ALICE], "Kaon–proton strong interaction at low relative momentum via femtoscopy in Pb–Pb collisions at the LHC," Phys. Lett. B **822**, 136708 (2021).

39. S. Acharya *et al.* [ALICE], "Charged-particle multiplicity fluctuations in Pb–Pb collisions at $\sqrt{s_{NN}}$ = 2.76 TeV," Eur. Phys. J. C **81**, no.11, 1012 (2021).

40. S. Acharya *et al.* [ALICE], "Measurement of K$^*$(892)$^\pm$ production in inelastic pp collisions at the LHC," Phys. Lett. B **828**, 137013 (2022).

41. S. Acharya *et al.* [ALICE], "First measurements of N-subjettiness in central Pb-Pb collisions at $\sqrt{s_{NN}}$ = 2.76 TeV," JHEP **10**, 003 (2021).

42. S. Acharya *et al.* [ALICE], "Measurement of the Cross Sections of $\Xi_c^0$ and $\Xi_c^+$ Baryons and of the Branching-Fraction Ratio BR($\Xi_c^0 \rightarrow \Xi^- e^+ \nu_e$)/BR($\Xi_c^0 \rightarrow \Xi^- \pi^+$) in pp collisions at 13 TeV," Phys. Rev. Lett. **127**, no.27, 272001 (2021).

43. S. Acharya *et al.* [ALICE], "Investigating the role of strangeness in baryon–antibaryon annihilation at the LHC," Phys. Lett. B **829**, 137060 (2022).

44. S. Acharya *et al.* [ALICE], "Production of $\Lambda$ and $K_s^0$ in jets in p–Pb collisions at $\sqrt{s_{NN}}$=5.02 TeV and pp collisions at $\sqrt{s}$=7 TeV," Phys. Lett. B **827**, 136984 (2022).

45. S. Acharya *et al.* [ALICE], "Energy dependence of $\phi$ meson production at forward rapidity in pp collisions at the LHC," Eur. Phys. J. C **81**, no.8, 772 (2021).

46. S. Acharya *et al.* [ALICE], "Nuclear modification factor of light neutral-meson spectra up to high transverse momentum in p–Pb collisions at sNN=8.16 TeV," Phys. Lett. B **827**, 136943 (2022).

47. U. A. Acharya *et al.* [PHENIX], "Probing Gluon Spin-Momentum Correlations in Transversely Polarized Protons through Midrapidity Isolated Direct Photons in $p^\uparrow + p$ Collisions at $\sqrt{s}$=200 GeV," Phys. Rev. Lett. **127**, no.16, 162001 (2021).

48. S. Acharya *et al.* [ALICE], "Measurement of beauty and charm production in pp collisions at $\sqrt{s}$ = 5.02 TeV via non-prompt and prompt D mesons," JHEP **05**, 220 (2021).

49. S. Acharya *et al.* [ALICE], "Measurements of mixed harmonic cumulants in Pb–Pb collisions at $\sqrt{s_{NN}}$ = 5.02 TeV," Phys. Lett. B **818**, 136354 (2021).

50. S. Acharya *et al.* [ALICE], "First measurement of the |*t*|-dependence of coherent $J/\psi$ photonuclear production," Phys. Lett. B **817**, 136280 (2021).

51. S. Acharya *et al.* [ALICE], "Coherent J/■ and ■′ photoproduction at midrapidity in ultra-peripheral Pb-Pb collisions at $\sqrt{s_{\mathrm{NN}}}$ = 5.02 TeV," Eur. Phys. J. C **81**, no.8, 712 (2021).

52. S. Acharya *et al.* [ALICE], "Long- and short-range correlations and their event-scale dependence in high-multiplicity pp collisions at $\sqrt{s}$ = 13 TeV," JHEP **05**, 290 (2021).

53. S. Acharya *et al.* [ALICE], "Production of pions, kaons, (anti-)protons and $\phi$ mesons in Xe–Xe collisions at $\sqrt{s_{\mathrm{NN}}}$ = 5.44 TeV," Eur. Phys. J. C **81**, no.7, 584 (2021).

54. S. Acharya *et al.* [ALICE], "First measurement of coherent $\rho$0 photoproduction in ultra-peripheral Xe–Xe collisions at sNN=5.44 TeV," Phys. Lett. B **820**, 136481 (2021).

55. S. Acharya *et al.* [ALICE], "Multiharmonic Correlations of Different Flow Amplitudes in Pb-Pb Collisions at $\sqrt{s_{NN}}$ = 2.76 TeV," Phys. Rev. Lett. **127**, no.9, 092302 (2021).

56. K.S. Tanaka, K. Harada, T. Hayamizu, R. Kita, R. Kono, K. Maruta, H. Nagahama, N. Ozawa, Y. Sakemi, R. Sugimori, "The accelerator experiment for junior and senior high school students to improve students' involvement in fundamental physics," Physics Education **57**, 045013 (2022).

57. R. Mitraa, V. S. Prasannaa, R. F. Garcia Ruiz, T. K. Sato, M. Abe, Y. Sakemi, B. P. Das and B. K. Sahoo, "Towards CP Violation Studies on Superheavy Molecules: Theoretical and Experimental Perspectives," Phys. Rev. A **104**, 062801 (2021).

58. T. Aoki, R. Sreekantham, B. K. Sahoo, Bindiya Arora, A. Kastberg, T. Sato, H. Ikeda, N. Okamoto, Y. Torii, T. Hayamizu, K. Nakamura, S. Nagase, M. Ohtsuka, H. Nagahama, N. Ozawa, M. Sato, T. Nakashita, K. Yamane, K. S. Tanaka, K. Harada, H. Kawamura, T. Inoue, A. Uchiyama, A. Hatakeyama, A. Takamine, H. Ueno, Y. Ichikawa, Y. Matsuda, H. Haba and Y. Sakemi, "Quantum sensing of the electron electric dipole moment using ultracold entangled Fr atoms," Quantum Science and Technology, **6**, 044008 (2021).

59. K.S. Tanaka, U. Dammalapati, K. Harada, T. Hayamizu, M. Itoh, H. Kawamura, H. Nagahama, K. Nakamura, N. Ozawa, Y. Sakemi, "Two-dimensional beam profile monitor for the detection of alpha-emitting radioactive isotope beam," Nucl. Instrum. Methods in Phys. Res. A **1017**, 165803 (2021).

60. E. Ideguchi, T. Kibedi, J. Dowie, H. T. Hoang, Kumar Raju M., G. Lane, L. Bignell, T.K. Eriksen, A. J. Mitchell, A. Akber, B. Combes, B. McCormik, T. Gray, A. Stuchbery, N. Shimizu, and Y. Utsuno, "Electric monopole transition from the superdeformed band in $^{40}$Ca", Phys. Rev. Lett. in press. https://arxiv.org/abs/2205.06516

61. S. Yoshida and N. Shimizu, "A new workflow of shell-model calculations with the emulator and preprocessing using eigenvector continuation", Prog. Theor. Exp. Phys. in press. https://doi.org/10.1093/ptep/ptac057

62. T. Otsuka, T. Abe, T. Yoshida, Y. Tsunoda, N. Shimizu, N. Itagaki, Y. Utsuno, J. Vary, P. Maris and H. Ueno, "$\alpha$-clustering in atomic nuclei from First Principles with Statistical Learning and the Hoyle State character", Nat. Comm. **13**, 2234 (2022).

63. N. Kitamura, K. Wimmer, T. Miyagi, A. Poves, N. Shimizu, J. A. Tostevin, V. M. Bader, C. Bancroft, D. Barofsky, T. Baugher, D. Bazin, J. S. Berryman, V. Bildstein, A. Gade, N. Imai, T. Kröll, C. Langer, J. Lloyd, E. Lunderberg, F. Nowacki, G. Perdikakis, F. Recchia, T. Redpath, S. Saenz, D. Smalley, S. R. Stroberg, Y. Utsuno, D. Weisshaar, A. Westerberg, "In-beam $\gamma$-ray spectroscopy of $^{32}$Mg via direct reactions", Phys. Rev. C **105**, 034318 (2022).

64. T. Koiwai, K. Wimmer, P. Doornenbal, A. Obertellid, T. Miyagi, J. D. Holt, N. Shimizu, V. Soma, Y. Utsuno, K. Ogata, K. Yoshida, N. Achouri, H. Baba, F. Browne, D. Calvet, F. Chateaue, S. Chen, N. Chiga, A. Corsi, M. L. Cortes, A. Delbart, J-M. Gheller, A. Giganon, A. Gillibert, C. Hilaire, T. Isobe, T. Kobayashi, Y. Kubota, V. Lapoux, H. N. Liue, T. Motobayashi, I. Murray, H. Otsu, V. Panin, N. Paul, W. Rodriguez, H. Sakurai, M. Sasano, D. Steppenbeck, L. Stuhl, Y. L. Sun, Y. Togano, T. Uesaka,K. Yoneda, O. Aktas, T. Aumann, L. X. Chung, F. Flavigny, S. Franchoo, I. Gasparic, R.-B. Gerst, J. Gibelin, K. I. Hahn, D. Kim, Y. Kondo, P. Koseoglou, J. Lee, C. Lehr, B. D. Linh, T. Lokotko, M. MacCormick, K. Moschner, T. Nakamura, S. Y. Park, D. Rossi, E. Sahina, P-A. Soderstrom, D. Sohlera, S. Takeuchi, H. Toernqvist, V. Vaquero, V. Wagner, S. Wanga, V. Werner, X. Xu, H. Yamada, D. Yana, Z. Yang, M. Yasuda, L. Zanetti, "A First glimpse at the shell structure beyond $^{54}$Ca: spectroscopy of $^{55}$K, $^{55}$Ca and $^{57}$Ca", Phys. Lett. B **827**, 136953 (2022).

65. T. Otsuka, N. Shimizu, and Y. Tsunoda, "Moments and radii of exotic Na and Mg isotopes", Phys. Rev. C **105**, 014319 (2022).

66. B. D. Linh, A. Corsi, A. Gillibert, A. Obertelli, P. Doornenbal, C. Barbieri, S. Chen, L.X. Chung, T. Duguet, M. Gomez-Ramos, J.D. Holt, A. Moro, P. Navratil, K. Ogata, N. T. T. Phuc, N. Shimizu, V. Soma, Y. Utsuno, N. Achouri, H. Baba, F. Browne, D. Calvet, F. Chateau, N. Chiga, M. L. Cortes, A. Delbart, J.-M. Gheller, A. Giganon, C. Hilaire, T. Isobe, T. Kobayashi, Y. Kubota, V. Lapoux, H. N. Liu, T. Motobayashi, I. Murray, H. Otsu, V. Panin, N. Paul, W. Rodriguez, H. Sakurai, M. Sasano, D. Steppenbeck, L. Stuhl, Y. L. Sun, Y. Togano, T. Uesaka, K. Wimmer, K. Yoneda, O. Aktas, T. Aumann, F. Flavigny, S. Franchoo, I. Gasparic, R.B. Gerst, J. Gibelin, K.I. Hahn, N.T. Khai, D. Kim, T. Koiwai, Y. Kondo, P. Koseoglou, J. Lee, C. Lehr, T. Lokotko, M. Maccormick, K. Moschner, T. Nakamura, S. Y. Park, D. Rossi, E. Sahin, D. Sohler, P.-A. Soderstrom, S. Takeuchi, H. Tornqvist, V. Vaquero, V. Wagner, H. Wang, V. Werner, X. Xu, N.D. Ton, Y. Yamada, D. Yan, Z. Yang, M. Yasuda, and L. Zanetti, "Investigation of the ground-state spin inversion in the neutron-rich $^{47,49}$Cl isotopes", Phys. Rev. C **104**, 044331 (2021).

67. N. Kitamura, K. Wimmer, A. Poves, N. Shimizu, J. Tostevin, V. M. Bader, C. Bancroft, D. Barofsky, T. Baugher, D. Bazin, J. S. Berryman, V. Bildstein, A. Gade, N. Imai, T. Kroll, C. Langer, J. Lloyd, E. Lunderberg, G. Perdikakis, F. Recchia, T. Redpath, S. Saenz, D. Smalley, S. R. Stroberg, Y. Utsuno, D. Weisshaar, and A. Westerberg, "Coexisting normal and intruder configurations in $^{32}$Mg", Phys. Lett. B **822**, 136682 (2021).

68. T. Abe, P. Maris, T. Otsuka, N. Shimizu, Y. Utsuno, and J. P. Vary, "Ground-state properties of light 4$n$ self-conjugate nuclei in no-core Monte Carlo shell model with nonlogcal $NN$ interactions", Phys. Rev. C **104**, 054315 (2021).

69. R. Nakamoto, E. Ueda, M. Ito, and N. Shimizu, "Formulation of shell-cluster overlap integral with Gaussian expansion method", Prog. Theor. Exp. Phys. **2021**, 113D01 (2021).

70. H. Kleis, M. Seidlitz, A. Blazhev, L. Kaya, P. Reiter, K. Arnswald, A. Dewald, M. Droste, C. Fransen, O. Möller, N. Shimizu, Y. Utsuno, P. von Brentano, and K. O. Zell, "Lifetime measurements of excited states in $^{55}$Cr", Phys. Rev. C **104**, 034310 (2021).

71. N. Shimizu, T. Mizusaki, K. Kaneko, and Y. Tsunoda, "Generator-coordinate methods with symmetry-restored Hartree-Fock-Bogoliubov wave functions for large-scale shell-model calculations", Phys. Rev. C **103**, 064302 (2021).

72. K. Kaneko, N. Shimizu, T. Mizusaki, and Y. Sun, "Triple enhancement of quasi-SU(3) quadrupole collectivity in Strontium-Zirconium $N \approx Z$ isotopes", Phys. Lett. B **817**, 136286 (2021).

## B. Proceedings

1. S. Michimasa, "Development of energy-degraded RI beam and expansion of nuclear reaction studies – Recent results obtained by the OEDO-SHARAQ system – Proceedings of the 2020 Symposium on Nuclear Data" Nov. 26-27, RIKEN Nishina Center, RIKEN Wako Campus, Wako, Saitama,Japan. JAEA-Conf2021-001 pp.59–64 (2021)

2. S. Gorbunov, E. Hellbar, G. M. Innocenti, M. Ivanov, M. Kabus, M. Kleiner, H. Riaz, D. Rohr, R. Sadikin and K. Schweda, et al. "Deep neural network techniques in the calibration of space-charge distortion fluctuations for the ALICE TPC," EPJ Web Conf. **251**, 03020 (2021).

3. D. Sekihata for the ALICE Collaboration, "Low-mass dielectron measurements in pp, p-Pb and Pb-Pb collisions with ALICE at the LHC", PoS HardProbes2020 (2021) 047, 10th International Conference on Hard and Electromagnetic Probes of High-Energy Nuclear Collisions, Onlnie, 31 May - 5 June 2020.

4. T. Hayamizu, H. Haba, K. Nakamura, T. Aoki, H. Nagahama, K. Tanaka, N. Ozawa, M. Ohtsuka, Y. Sakemi, "Development of Ultracold Francium Atomic Sources Towards the Permanent EDM Search," Few-Body Systems, FBSY-D-21-00090R1 (2021).

5. N. Shimizu, Y. Utsuno and T. Togashi, "$\beta$-decay half-lives of neutron-rich N=82,81 isotones by shell-model calculations", EPJ Web of Conferences **260**, 11049 (2022).

## C. Theses

1. S. Nagase: "Development for the cold Francium source with laser cooling technique for the atomic electric dipole moment search": Master thesis, the University of Tokyo. March 2021.

# Talks and Presentations

## A. International Conference

1. H. Yamaguchi (oral), "Nuclear astrophysics at the low-energy RI beam separator CRIB", RIBF Users Meeting 2021, web meeting hosted by RIKEN, Wako, Saitama, Japan, Sep. 7–9, 2021.

2. H. Yamaguchi (oral), "Experimental studies on astrophysical reactions at the low-energy RI beam separator CRIB", The 16th International Symposium on Nuclei in the Cosmos (NIC-XVI), web symposium hosted by JUNA, China, Sep. 21-25, 2021.

3. H. Yamaguchi (oral), "Cluster states and astrophysical $(\alpha, p)$ reactionss", RCNP Workshop, "Cluster phenomena in knockout and astrophysical reactions", web workshop hosted by RCNP, Osaka University, Oct. 14–15, 2021.

4. T. Gunji (invited) for the ALICE collaboration, "Future measurements from ALICE Run3 and Run4", The 8th Asian Triangle Heavy-Ion Conference (ATHIC2021), hybrid, 5–9 Nov 2021, Inha Univ. Incheon, South Korea.

5. D. Sekihata for the ALICE Collaboration, "Low-mass dielectron measurement in ALICE at the LHC", The 8th Asian Triangle Heavy-Ion Conference, hybrid, 5–9 Nov 2021, Inha Univ. Incheon, South Korea.

6. Y. Utsuno (Oral), "Present status of large-scale shell-model calculations for photonuclear reactions", Second PANDORA Workshop, September 10, 2021.

7. N. Shimizu (Oral), "Microscopic description of the collective motions of medium-heavy nuclei based on shell-model calculations", 13th symposium on Discovery, Fusion, Creation of New Knowledge by Multidisciplinary Computational Sciences, online, October 8, 2021.

8. Y. Tsunoda (Oral), "Nuclear shapes and collective motions in the region of Sm", 13th symposium on Discovery, Fusion, Creation of New Knowledge by Multidisciplinary Computational Sciences, online, October 8, 2021.

9. N. Shimizu (Poster), "Gamow-Teller transition of neutron-rich N=82,81 nuclei by shell-model calculations", 16th International Symposium on Nuclei in the Cosmos (NIC-XVI), Zoom online meeting, September 25, 2021.

## B. Domestic Conference

1. S. Shimoura (Invited): "High-resolution spectroscopy with SHARAQ and advice on HIHR", the 2nd J-PARC HEF-ex workshop, on-line, February 16 -18, 2022

2. T. Chillery (Oral): "Measurement of Deuteron-Induced Pre-equilibrium Reactions on 93Zr at 30 MeV/u for the Treatment of Radioactive Waste", 77th JPS meeting 2022 Spring, online.

3. R. Tsunoda (Oral): "Observation of the isobaric analog resonances coupled to the excited state in Zr isotope", 77th JPS meeting 2022 Spring, online.

4. J.T. Li (Oral): "New project to explore neutron-deficient actinide nuclei", 77th JPS meeting 2022 Spring, online.

5. S. Hanai (Oral): "A fast-response tracking detector for high-intensity heavy ion beams", Workshop for radiation detector and their uses, KEK 2022, Jan. 24-26.

6. N. Imai (Invited): "Nuclear Structure study with decelerated RI beams" RCNP future workshop, 27–29th/Oct. 2021.

7. 川田敬太 (口頭発表),「核破砕反応における角運動量移行」, 日本物理学会 2021 年秋季大会, オンライン講演, 2021 年 9 月 14–17 日.

8. 早川勢也（口頭発表）:" 7Be+n ビッグバン元素合成反応の測定と原始 7Li 生成量の検証 "、日本物理学会 秋季大会、14pU2- 2、オンライン開催、2021 年 9 月 14–17 日.

9. 郡司卓 (invited), "Status of ALICE Upgrade and Commissioning for Run3", 第 7 回クラスター階層領域研究会, 2021 年 12 月 27-28 日, 東北大学.

10. 郡司卓 (invited)、"高密度クォーク物質探索の展望", シンポジウム「宇宙観測、加速器実験と理論の協奏で探る高密度核物質」、日本物理学会、3/15-3/19, オンライン.

11. 関畑大貴 (invited),"光子・レプトン対・ハード測定", 重イオン衝突の時空発展の理解に向けた理論・実験合同研究会, オンライン, 2021 年 9 月 24 日.

12. D. Sekihata for the ALICE Collaboration,"√ sNN = 5.02 TeV 鉛+鉛原子核衝突における ALICE 実験の電子対測定", 日本物理学会 2021 年秋季大会, オンライン, 2021 年 9 月 14-17 日.

13. 関畑大貴,"ALICE 実験での電子対の結果と展望", Heavy Ion Pub 研究会, オンライン, 2021 年 5 月 28 日.

14. 関口 裕子 for the ALICE Collaboration,"LHC-ALICE 実験を用いた長距離 2 粒子相関のシステムサイズ依存性測定", 日本物理学会第 77 回年次大会, オンライン, 2022 年 3 月 15-19 日.

15. 関口 裕子 for the ALICE Collaboration, "LHC-ALICE 実験を用いた小さな衝突系における 2 粒子相関測定", 日本物理学会 2021 年秋季大会, オンライン, 2021 年 9 月 14-17 日.

16. 鎌倉恵太 (ポスター発表), 「東京大学 CNS 14 GHz Hyper ECR イオン源の現状」, 第 18 回日本加速器学会年会, オンライン講演, 2021 年 8 月 9-12 日

17. 小高康照 (ポスター発表), 「東京大学 CNS 14 GHz Hyper ECR イオン源の現状」, 第 18 回日本加速器学会年会, オンライン講演, 2021 年 8 月 9-12 日

18. 清水則孝（口頭発表), 「CI 計算とその発展的手法による大規模原子核構造計算」, 2021 年度第 2 回 HPCIC 計算科学フォーラム (オンライン開催), 2022 年 3 月 28 日.

19. 清水則孝, 吉田聡太、角田直文、角田佑介、大塚孝治（口頭発表）, 「殻模型計算による中性子過剰 pf 殻核の構造」, 日本物理学会第７６回年次大会 (オンライン開催) 2022 年 3 月 17 日

20. 清水則孝（口頭発表), 「CI 計算とその発展的手法による大規模原子核構造計算」, 「富岳」成果創出加速プログラム シンポジウム・研究交流会「富岳百景」2021 年度第 2 回 HPCIC 計算科学フォーラム　(オンライン開催) 2022 年 3 月 14 日

21. 清水則孝（口頭発表), 「大規模殻模型計算による中重核構造研究の進展」「富岳で加速する素粒子・原子核・宇宙・惑星」シンポジウム (オンライン開催), 2022 年 1 月 17 日

22. 清水則孝, 宇都野穣, 富樫智章（口頭発表）, 「殻模型計算による N=82,81 中性子過剰核のガモフテラー遷移」日本物理学会 2021 年秋の分科会　(オンライン開催), 2021 年 9 月 14 日

23. 角田佑介、清水則孝、大塚孝治（口頭発表）, 「準粒子真空殻模型計算による中重核の構造の研究」, 日本物理学会 2021 年秋季大会 (オンライン開催), 2021 年 9 月 15 日

24. 角田佑介、清水則孝、大塚孝治（口頭発表）, 「準粒子真空殻模型計算による Sm 領域の構造の研究」, 日本物理学会第 77 回年次大会 (オンライン開催), 2022 年 3 月 17 日

25. 柳瀬宏太、清水則孝、東山幸司、吉永尚孝（口頭発表）, 「キセノン原子核のシッフモーメントと中性子 EDM 探索」, 日本物理学会第 77 回年次大会, 2022 年 3 月 17 日

26. 宇都野穣、角田佑介、清水則孝（口頭発表）, 「大規模殻模型計算による M1 バンドの解析」, 日本物理学会 2021 年秋季大会, 2021 年 9 月 15 日

27. 宇都野穣（口頭発表), 「非イラスト領域における原子核の秩序の探求」, RCNP での次期計画検討会, 2021 年 9 月 27 日

28. 宇都野穣（口頭発表), "Cluster formation in nuclei from first-principles Monte Carlo shell model", 第 7 回クラスター階層領域研究会, 2021 年 12 月 27 日

# C. Lectures

1. Y. Sakemi, H. Yamaguchi: "Nuclear Physics III", Summer, 2021.

2. T. Gunji (with K. Fukushima): "High-Energy hadron physics", Autumn, 2021.

3. K. Yako (with M. Yokoyama): "Experimental Techniques in Particle and Nuclear Physics", Summer, 2021.

4. N. Imai: "Nuclear Physics I/II", Autumn, 2021.

5. K. Yako: "Classical mechanics A for undergraduate students", Summer, 2021.

6. K. Yako, H. Nagahama: "Physics Experiment II", Autumn, 2021.

# Press Releases

1. 山口英斉, 早川勢也,Hu Jun,「X 線バースト天体における不安定マグネシウム燃焼の解明」, 2021 年 10 月 20 日.

2. 早川勢也, 山口英斉,「ビッグバンで生成されるリチウム量の矛盾、解決へ一歩前進」, 2021 年 7 月 1 日.

# Personnel

**Director**

SHIMOURA, Susumu
*Professor, Graduate School of Science*
*Center for Nuclear Study*

**Scientific Staff**

| | |
|---|---|
| SAKEMI, Yasuhiro | *Professor* |
| YAKO, Kentaro | *Associate Professor* |
| IMAI, Nobuaki | *Associate Professor* |
| GUNJI, Taku | *Associate Professor* |
| SHIMIZU, Noritaka | *Project Associate Professor* |
| YAMAGUCHI, Hidetoshi | *Lecturer* |
| MICHIMASA, Shin'ichiro | *Assistant Professor* |
| OTA, Shinsuke | *Assistant Professor* |
| NAGAHAMA, Hiroki | *Assistant Professor* |

**Guest Scientists**

| | |
|---|---|
| UTSUNO, Yutaka | *JAEA* |
| NISHIMURA, Daiki | *Tokyo City University* |
| KAJINO, Toshitaka | *NAOJ* |
| HAMAMOTO, Ikuko | *Lund University* |
| HWANG, Jongwon | *IBS* |

**Technical Staff**

KOTAKA, Yasuteru

**Technical Assistant**

YAGYU, Masayoshi

**Project Research Associates**

DOZONO, Masanori　　　　　　　　HAYAKAWA, Seiya

SEKIHATA, Daiki　　　　　　　　　YOKOYAMA, Rin

**Post Doctoral Associates**

MA, Nanru　　　　　　　　　　　　TSUNODA, Yusuke

NAKAMURA, Keisuke　　　　　　　YANASE, Kota

KAMAKURA, Keita　　　　　　　　CHILLERY, Thomas William

**Academic Specialist**

KOJIMA, Reiko

**Assistant Teaching Staff**

SEKIGUCHI, Yuko　　　　　　　　SAKAUE, Akane

KAWATA, Keita　　　　　　　　　MASUOKA, Shoichiro

**Graduate Students**

SHIMIZU, Hideki　　　　　　　　　TSUNODA, Rieko

OZAWA, Naoya　　　　　　　　　　HANAI, Shutaro

NAGASE, Shintaro　　　　　　　　KOHARA, Ryotaro

LI, Jiatai　　　　　　　　　　　　UEHARA, Daisuke

OKAWA, Kodai　　　　　　　　　　BABA, Hitoshi

FUKASE, Mirai

**Administration Staff**

SHIMANE, Noriko

YAMAMOTO, Ikuko　　　　　　　KISHI, Yukino

KOTAKA, Aki

**Committees**

**Steering Committee**

| | |
|---|---|
| OHKOSHI, Shinichi | *Department of Chemistry, Graduate School of Science, UT* |
| HOSHINO, Masahiro | *Department of Earth and Planetary Physics, Graduate School of Science, UT* |
| TSUNEYUKI, Shinji | *Department of Physics, Graduate School of Science, UT* |
| SAKURAI, Hiroyoshi | *Department of Physics, Graduate School of Science, UT* |
| MORI, Toshinori | *International Center for Elementary Particle Physics, UT* |
| TAKAHASHI, Hiroyuki | *Department of Nuclear Engineering and Management, Graduate School of Engineering, UT* |
| SHIMOURA, Susumu | *Center for Nuclear Study, Graduate School of Science, UT* |
| SAKEMI, Yasuhiro | *Center for Nuclear Study, Graduate School of Science, UT* |
| YAKO, Kentaro | *Center for Nuclear Study, Graduate School of Science, UT* |
| TAMURA, Hirokazu | *Department of Physics, Graduate School of Science, Tohoku University* |